Petrogenesis of the LG-6 chromitite at Ruighoek mine, western limb of the Bushveld Complex, South Africa

University of the Witwatersrand, Johannesburg

School of Geosciences

By: Ryan McIntosh

Student Number: 0713618G

2017

A Dissertation submitted to the Faculty of Science, University of Witwatersrand in the fulfilment of the requirements for the degree of Master of Science (Geology)

Declaration

I declare that this thesis is my own, unaided work. It is being submitted for the Degree of Master of Science at the University of the Witwatersrand, Johannesburg. It has not been submitted before for any degree or examination at any other University.

_____

Ryan McIntosh

_____ Day of _____201_ in _____.

Abstract

The LG-6 chromitite layer is the thickest (0.90 to 1.20 m thick) chromitite layer in the Lower Group chromitites of the Bushveld Complex and is of economic significance owing to the relatively high Cr-content. It can be traced across the entirety of the western limb and is mined in both the western limb and the eastern limb.

This study evaluates previously published models of chromitite formation using data from the LG-6 chromitite at Ruighoek Mine, western Bushveld Complex. Data includes petrographic studies of the reef and host rocks, whole rock analysis of the silicate host rocks and reef, and mineral chemistry for orthopyroxene, olivine and Cr-spinel using electron probe microanalysis (EPMA).

In the Ruighoek region the LG-6 chromitite comprises up to 95 vol. % chromite and is typically hosted by orthopyroxenite. Borehole data indicated an area (about 250 m^2 in size) where the LG-6 is entirely hosted by harzburgite (42% orthopyroxene, 11% Cr-spinel, 14% olivine, 32% serpentine and 1% other) rather than orthopyroxenite. The whole rock and mineral chemistry revealed that the LG-6 chromitite in this area has an exceptionally high Cr/Fe ratio, up to 2.1. The whole rock data also indicated several compositional reversals in terms of MgO, Al_2O_3, Cr_2O_3, FeO, and Mg# (Mg/ [Mg+Fe^{2+}]) for the unenriched borehole 13R-3, and compositional reversals in Cr/Fe and Cr# (Cr/ [Cr+Al]) for the enriched borehole 13R-9 upwards through the chromitite layer. The hanging wall harzburgites are characterized by an increase in Mg# for the mineral chemistry of the Cr-spinel, orthopyroxene and olivine compared to those in the footwall harzburgite. Importantly, spatial 3D modelling of borehole data at Ruighoek mine (19 drill-cores) indicates that the elevated Cr/Fe ratio in LG-6 chromitite is coincident with a depression in the topography of the chamber floor at the time of formation of the LG-6 chromitite.

These data are difficult to reconcile with existing models for chromitite formation in layered intrusions, such as the models for gravity settling, addition of a Cr-spinel crystal-laden magma, or a pressure increase. Thus, this work has developed a new model for formation of the LG-6 chromitite at Ruighoek Mine. The exceptionally high Cr/Fe ratio of LG-6 chromitite and its close association with harzburgite is attributed to multiple replenishments of the chamber by relatively primitive magmas. These are inferred to either be saturated in olivine and chromite, or chromite alone. The occurrence of relatively primitive rocks within the depression is suggested to be related to a local feeder situated within the depression. Injection of new, relatively dense magma pulses from the feeder are inferred to spread out across the chamber floor as basal flows owing to compositional stratification of the resident magma at the time of development of the LG-6 chromitite. The replenishing magmas contributed to the existing compositional stratification in the chamber, resulting in the most primitive composition within the depression of the chamber floor. Subsequent crystallisation of the most primitive magmas within the depression resulted in local development of LG-6 chromitite with exceptionally high Cr/Fe ratios together with the enclosing harzburgitic rocks. The thickness of the LG-6 chromitite is attributed to continuous replenishment by large volumes of new, chromite-saturated, magmas via the feeder channel located in the depression. This study suggests that magma stratification and the replenishment of the chamber by chromite-saturated magmas played an important role in the development of the chromitite layers of the Bushveld Complex.

Dedicated to

My Ouma

11 October 1921 – 20 October 2015

Acknowledgements

First and foremost, I would like to express gratitude to Prof. Rais Latypov for supervising this research project and both Prof. Rais Latypov and Dr. Sofya Chistyakova for setting up an interesting and challenging project. A special thanks to Dr. Emma Hunt for her guidance, constructive criticism, patience and willingness to lend an ear.

The project could not have happened without Ruighoek mine and Andru Scoggings for supplying the samples necessary for the project. Thank you to the National Research Foundation (NRF) for the funding they provided.

I would also like to thank Miek Meyering for assistance with sampling at Ruighoek, Christelle Van Der Merwe at Assore for additional samples and data from Groenfontein farm, and site visits.

I would like to thank Dr. Péter Horváth for assistance with the EPMA and related corrections of the data, as well as Dr. Hannah Hughes for assistance with processing of the whole rock data.

I am grateful to the Dr. Grant Bybee, Dr. Zubair Jinnah, Adam Engela, Mike Donze and Katie Hill for all the support and advice over the course of this project particularly regarding coffee.

Finally I would like to thank Sally-Anne Lee for her enduring support.

Table of Contents

List of figures

List of tables

1. Geological Background

1.1 Introduction

The LG-6 chromitite occurs within the lower Critical Zone of the Rustenburg Layered Suite, Bushveld Complex (BC). Due to its lateral continuity and thickness (0.90-1.20 m) it is the only economic horizon within the lower group chromitite layers. The thickness and continuity make it ideal for understanding the processes through which Cr-spinel is concentrated (Cawthorn et al., 2006). This chapter will provide an overview of the regional geology and processes inferred to account for the development of chromitite layers.

1.2 Regional setting

The Kaapvaal craton, Southern Africa stabilised between 3.0 and 2.7 Ga, and since then has been undergone various transgressive and regressive events associated with sea level changes. During submersion, rocks in the volcano-sedimentary basins of the Witwatersrand (2.9 to 2.7 Ga), Ventersdorp, Transvaal (2.6 to 2.2 Ga), Waterberg and Karoo Supergroups accumulated (Cawthorn, 2015). The BC intruded the Transvaal Supergroup, which is a succession of meta-sedimentary quartzites followed by a dolomitic and banded ironstone sequence, with an alternating package of quartzite and shale, capped by an upper basaltic and acid volcanic phase (Eriksson et al, 2006; Eales and Cawthorn, 1996;) that were deposited onto the Kaapvaal craton (Kinnaird, 2005). The BC is a layered intrusion located in the north eastern part of South Africa (inset Figure 1.15) which lies slightly discordantly to the Pretoria Group of the Transvaal Supergroup (Cawthorn et al, 2006; Eales and Cawthorn, 1996).

1.3 The Bushveld Complex

The BC has been studied extensively in the last 100 years because of its richness of ore deposits, such as platinum, palladium, rhodium, chromium, vanadium. The BC is a Paleoproterozoic intrusion with

an approximate age of ca. 2054 Ma (Eales and Cawthorn, 1996; Kinnaird et al 2005, Scoates and Friedman, 2008) and is approximately 8-9 km in vertical thickness. The intrusive bodies of the BC are subdivided into: the Lebowa granite suite, the Rashoop granophyre suite and the Rustenburg Layered Suite (RLS) (Cawthorn et al., 2006; South African Committee for Stratigraphy, 1980). The RLS forms five limbs: the western limb, far-western limb, eastern limb, south-eastern (Bethal) limb and the northern (Potgietersrus) limb (Figure 1.14) (Cawthorn et al., 2006). The limbs of the BC dip towards the geographical centre of the complex at approximately 15° (Du Toit, 1926).The extent of the south-eastern limb was identified using gravity data (Figure 1.1) (Cawthorn & Webb 2001) as it does not outcrop and was corroborated with borehole core. Cawthorn and Webb (2001) suggest that based on gravity modelling the upper portions of the BC are laterally continuous across the entire complex. The intrusive rocks of the BC are overlain by the extrusive Rooiberg Group of felsic volcanics (Cawthorn et al., 2006; South African Committee for Stratigraphy, 1980). Figure 1.2 portrays a general geological cross section through the BC indicating the different outcropping lithologies from west to east (Cawthorn et al., 2006).

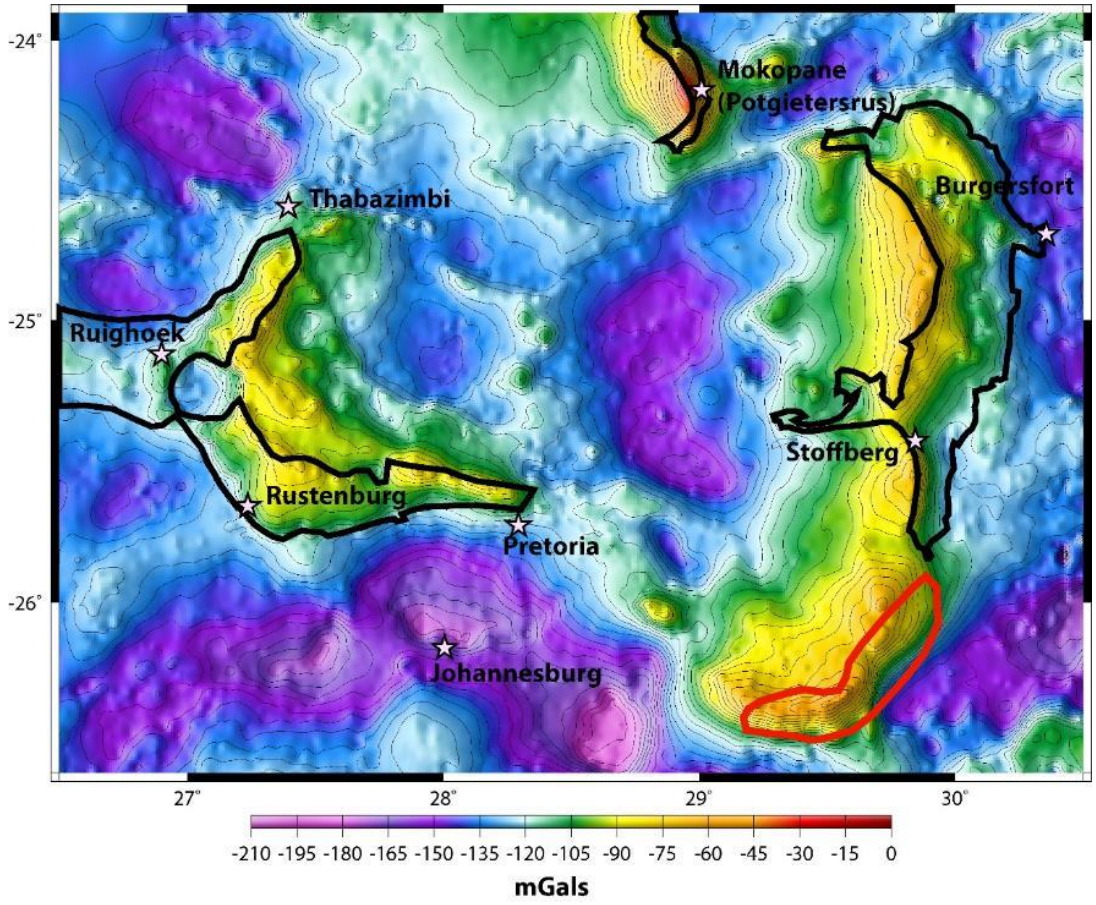

Figure 1.1: Gravity map of the Bushveld Complex, the black outline representing the approximate outcrop of the mafic rocks of the Bushveld Complex and the red outline indicating the approximate area of the covered south-eastern limb (adapted from Cawthorn and Webb, 2001)

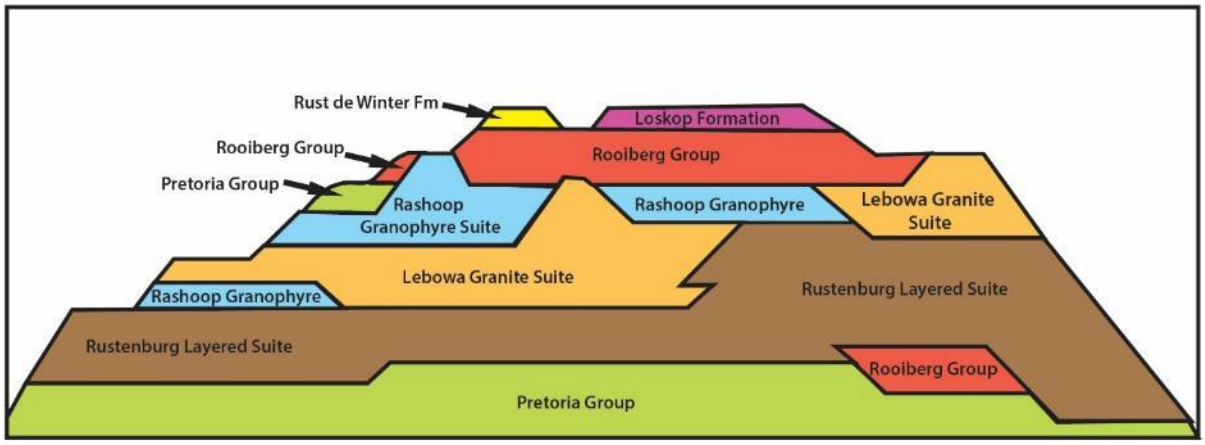

Figure 1.2: A schematic cross-section through the BC showing the different lithologies from West to East across South Africa as well as their relative association with each other stratigraphically (Cawthorn et al., 2006).

1.3.1 The Rooiberg Group

The Rooiberg Group volcanics (Figure 1.2) are ~3.5 km thick and cover a surface area >50 000 km^2 (Cawthorn et al., 2006). They consist of a volcanic sequence with interbedded sediments and have been dated via a Pb-Pb zircon age at 2061±2 Ma (Walraven, 1997). The group is comprised of 4 units: the basal Dullstroom Formation, the Damwal Formation, the Kwaggasnek Formation and the upper Schrikkloof Formation (Cawthorn et al., 2006; South African Committee for Stratigraphy, 1980). There is a compositional variation from basalts and dacites at the base of the sequence to rhyolites at the top (Bailie and Robb, 2004).

1.3.2 The Rashoop Granophyre Suite

The Rashoop Granophyre suite has an age of 2053±12 Ma (Coertze et al., 1978) and occurs below the Lebowa Granite suite and overlies the Pretoria Group, Transvaal Supergroup or locally the Rooiberg Group (Figure 1.2). It is comprised of 3 granophyre units, each of which can be classified as either metamorphic or magmatic based on their origin (Cawthorn et al., 2006; South African Committee for Stratigraphy, 1980). The Stavoren Granophyre is of a magmatic type (Cawthorn et al., 2006) and is characterised by well-developed intergrowths of quartz and alkali feldspar. It displays very little

differentiation, especially in comparison to the Lebowa Granite Suite granites (Cawthorn et al., 2006). The Zwartbank Pseudogranophyre is a metamorphic type, and is located in the western limb of the BC. It consists of irregular quartz and alkali feldspar intergrowths (Cawthorn et al., 2006). The Diepkloof Granophyre is also a metamorphic type, but is located in the eastern limb of the BC (Cawthorn et al., 2006). It is texturally similar to the Stavoren Granophyre, however it has a characteristically different trace element geochemistry (Cawthorn et al., 2006).

1.3.3 The Lebowa Granite Suite

The Lebowa Granite Suite (LGS) consists of a series of sheeted intrusions between 1.5 to 3.5 km thick (Figure 1.2) that dip <10° towards the centre of the complex (Kleeman and Twist, 1989). The LGS is comprised of seven granite facies: the Nebo Granite, Lease Granite, Bobbejaankop Granite, Balmoral Granite, Makhutso Granite, Klipkloof Granite and the Verena Granite (Bailie and Robb, 2004; South African Committee for Stratigraphy, 1980). It should be noted that these granite facies are described by various authors and named according to spatial distributions, but may have compositional similarities. Additionally, there may be a coarse-grained granite facies that is compositionally different to a fine-grained facies, however these are commonly grouped as it is hard to distinguish whether the fine-grained facies is part of a chill margin or a separate intrusion. The Nebo Granite is the most voluminous and has an age of 2054 ±1.8 Ma (Walraven and Hattingh, 1993).

1.3.4 The Rustenburg Layered Suite

The Rustenburg Layered Suite (RLS) is a mafic to ultramafic series of rocks up to 8 km in thickness (Cawthorn et al., 2006). It was emplaced below the Rooiberg volcanics, the Rashoop Granophyres and the Lebowa Granite Suite as well as within the Transvaal Supergroup (Figure 1.2). The RLS has been divided into 5 zones (Figure 1.3A): the Marginal Zone, Lower Zone, Critical Zone, Main Zone and Upper Zone. The exact boundaries of these zones are still debated, with different criteria applied by different authors. For example the South African Committee for Stratigraphy (1980) differentiates the different zones based on the appearance and disappearance of cumulus phases of minerals whereasKruger (1994) differentiates the zones based on Sr isotope ratios.

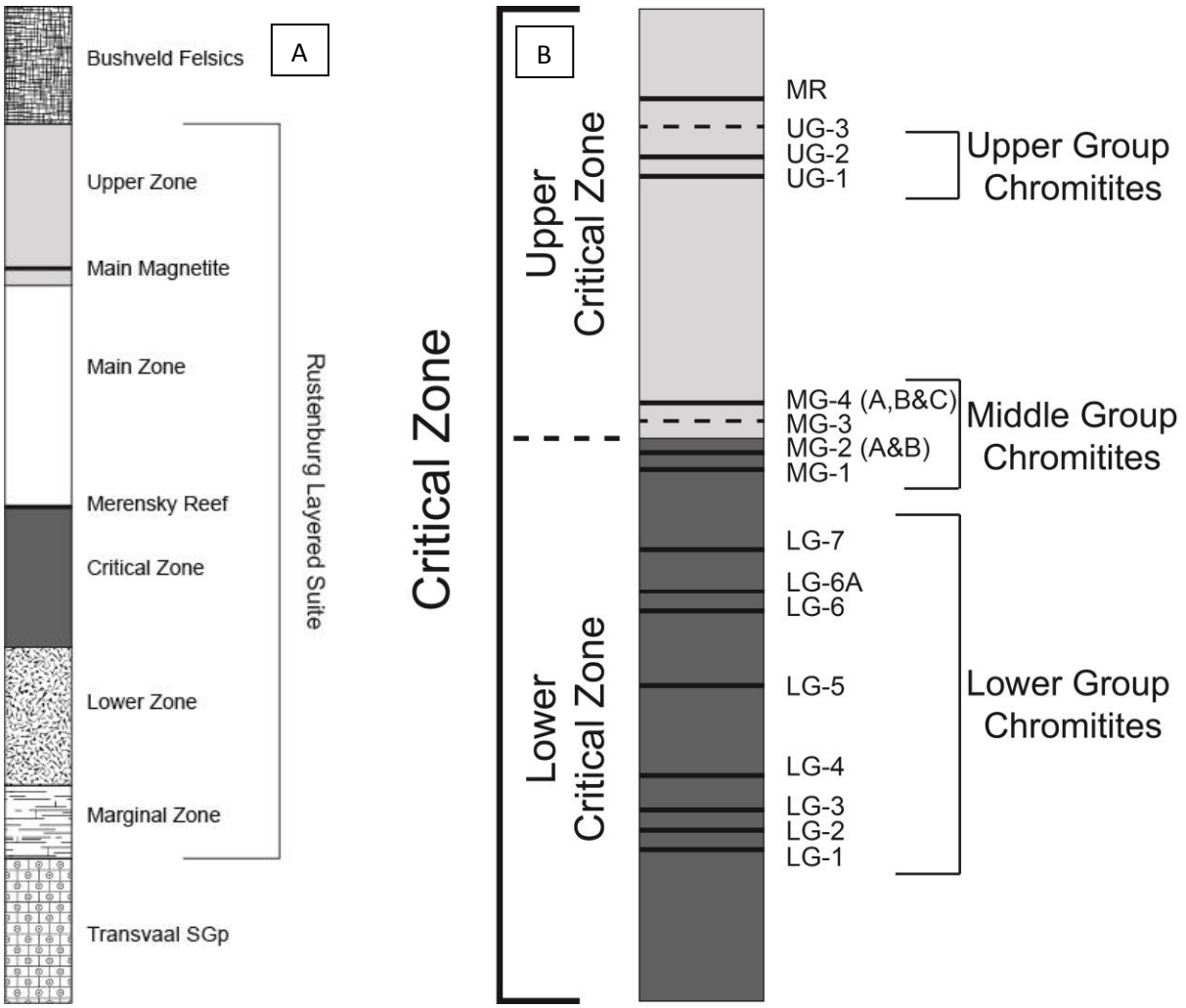

Figure 1.3: A- Generalised stratigraphic column of the Rustenburg Layered Suite showing the different zones (Eales and Cawthorn, 1996). B- Stratigraphy of the Critical Zone and its sub-division into the Lower and Upper Critical Zone and the locality of the chromititelayers. The MG-3 and UG-3 chromitite layers are not present everywhere in the BC (Andrew Scogings, Pers Comm).

The Marginal Zone is principally comprised of noritic rocks and is <800 m in thickness. The Lower Zone is comprised of ultramafic rocks including orthopyroxenite, dunite, harzburgite and is ~1700 m thick (Eales and Cawthorn, 1996). The Critical Zone is divided into the Lower and Upper Critical Zone (Figure 1.3B). The Lower Critical Zone is predominantly composed of pyroxenites and is 500-800 m in thickness whereas the Upper Critical Zone is composed of noritic to anorthositic rocks with fewer pyroxenitic and is 500-1000 m thick (Eales and Cawthorn, 1996). The boundary between the sub-zones is commonly accepted to be defined by the appearance of cumulus plagioclase in the Upper Critical Zone, between the MG-2 and MG-3 chromitite layers, when MG-3 is present, otherwise between MG-2 and MG-4 (Ashwal et al., 2005). The Critical Zone hosts the bulk of the economic resources (Cr and PGE) in the BC within chromitite layers and the Merensky reef (Figure 1.3B).

The Main Zone is principally composed of gabbronorite with lesser norite, gabbro and anorthosite and is the thickest zone in the RLS at 2200 – 3100 m in thickness (Nex et al., 1998). The Main Zone displays the least well developed igneous layering. Nex et al (1998) have divided it into five sub-zones based on pyroxene assemblages. The Upper Zone is defined by the appearance of cumulus magnetite and is divided into three sub-zones based on the appearance of different minerals (Eales and Cawthorn, 1996). Subzone A is comprised of gabbronorite and anorthosite, with 11 magnetite layers including the Main magnetite layer which is ~2 m thick (Eales and Cawthorn, 1996). Subzone B is distinguished by the appearance of olivine crystals with gabbronorite, anorthosite and multiple magnetite layers (Eales and Cawthorn, 1996). Subzone C is marked by the appearance of euhedral cumulus apatite crystals with olivine diorite, anorthosite and several magnetite layers (Eales and Cawthorn, 1996).

1.4 Chromitite layers

The Bushveld chromitite layers are situated in the Lower and Upper Critical Zone (Figure 1.3B). 14 chromitite layers have been distinguished within the Critical Zone (Cousins and Feringa, 1964; Eales and Cawthorn, 1996) and are divided, based on work by Cousins and Feringa (1964), into three groups: the Lower Group (LG), the Middle Group (MG) and the Upper Group (UG) with the numbering of each unit increasing from the bottom up (Figure 1.3B). The LG is in the Lower Critical Zone and the UG is in the Upper Critical Zone. The MG straddles the boundary between the Lower and Upper Critical Zone. The MG-3 and the UG-3 chromitite layers are not as laterally continuous as the other seams and are only found in some areas, for instance the UG-3 seam only outcrops on the eastern limb in the vicinity of the Driekop pipe.

Of all the chromitite layers the UG-1 and UG-2 chromitite layers are economically important because of their high PGE contents, UG-2 is mined extensively on both the Eastern and western limbs of the BC for PGE's. The other economically significant chromitite layer is the LG-6, but this is mined for chromium (Cr).

1.5 LG-6 Chromitite

The focus of this study, the LG-6 chromitite layer, is one of the chromitite layers of the LG chromitites, situated in the Lower Critical Zone (Figure 1.3B and Figure 1.4). It is laterally continuous across both

the western and eastern limbs. The LG-6 chromitite has previously been referred to in the literature as the “Steelpoort Chromitite layer”-Eastern BC, “M seam” – western BC, “Main seam” - western BC (Kroondal Chrome mine) and “Magazine seam” - western BC (Zwartkop Chrome mine) (Cameron, 1977; McDonald, 1967). It has a typical thickness of 0.90-1.20 m and is associated with orthopyroxenite host silicates and a thinner (~20 cm) overlying chromitite called the LG-6A leader reef (Teigler, 1999). LG-6 has a typical Cr/Fe ratio of ~1.55 (Cameron, 1977; Teigler 1990 & 1999; Scoon and Teigler, 1994), which means it is economically viable to mine for chromium oxide in both the western and eastern limbs of the BC.

Work by McDonald (1967) on four boreholes in the Ruighoek area observed that the LG-6 chromitite had a normal Cr/Fe ratio of 1.55 for two of them whereas the other two had elevated Cr/Fe ratios up to 1.95. There is no olivine in the two with normal Cr/Fe ratios, in contrast to the two with elevated Cr/Fe ratios which had olivine.

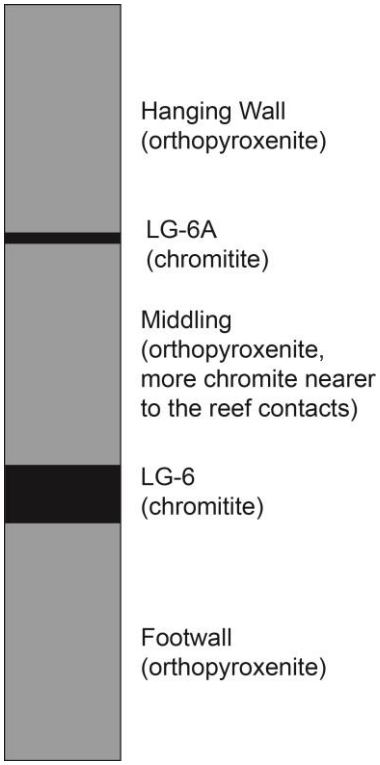

Figure 1.4: Generalised sketch of the LG-6 and LG-6A including hanging wall, middling and footwall.

1.6 Models of chromitite layer formation

The generation of chromitites within layered intrusions is widely debated and several models have been proposed to explain their formation and the most frequently cited are briefly described below, as well as a few newer models. However, investigating the development of the Bushveld Complex chromitites requires several geological features to be considered and addressed within any successful model for their formation.

- Chromitite layers are laterally extensive and can be traced for 300 - 400 km along strike (Figure 1.14).
- The total amount of chromium within the Lower and Critical Zones is greater than the amount that can be accounted for by the magma that generated the Lower, Critical, Main and Upper Zones (Eales, 2000), i.e. there is a mass balance problem. Thus either there is a large volume of residual magma missing, or additional chromium was introduced through later magma injections.
- Rocks comprised of a single cumulus phase (e.g. chromitite) are hosted between rocks comprised of multiple phases (e.g. norite, gabbronorite and pyroxenite). Processes of fractional crystallisation typically result in multiple phases crystallising at the same time and it is difficult to explain the occurrence of a single mineral phase hosted in rocks comprised of multiple phases. Therefore a mechanism to explain how Cr-spinel is concentrated as a single cumulus phase is required.
- Much of the Critical Zone is comprised of rhythmic or multi-cyclic (Maier and Bowen, 1996) units e.g. LG1-7, MG1-4 and UG1-2. Thus any model that attempts to explain the formation of Cr-spinel seams will need to be repeatable to generate the cyclicity. Although it is important to note here that the dominant processes forming each unit do not have to be identical to previous units and multiple mechanisms may occur within a single unit.
- The layering is not consistently sub-horizontal and erosional features such as potholes (Figure 1.5) are observed in the UG1, UG2 and Merensky reefs. In these features mineralisation can develop on overturned sidewalls (Figure 1.5) (Latypov *et al.* 2017).

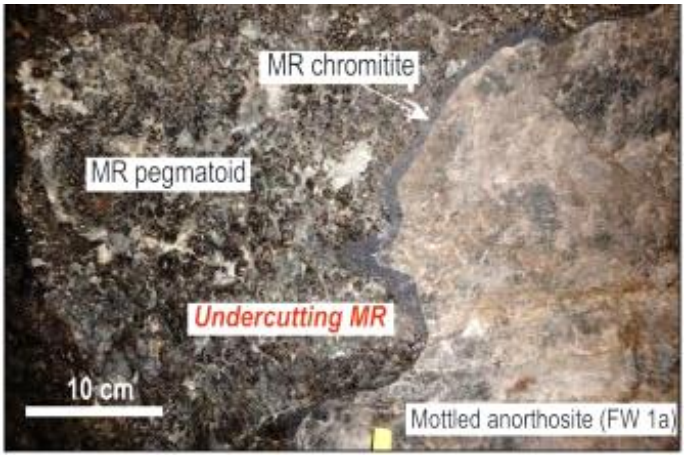

Figure 1.5: Chromitite mineralisation along the overturned sidewall of a pothole from the Merensky reef (Latypov *et al*, 2017).

1.6.1 Gravitational settling

Cr-spinel has a relatively high density (~4.5 g/cm^3), thus the gravitational settling model is appealing for the formation of the monomineralic chromitite layers. However, when discussing gravitational settling as a mechanism, additional factors such as crystal sizes must be taken into account. This is highlighted by Stokes equation for the velocity of settling:

$$V = 2gr^2 * (\rho_c - \rho_l)/9\eta$$

Where V is settling velocity, g – acceleration due to gravity, r – radius of spherical particle, ρ_c – density of particle, ρ_l – density of liquid and η – coefficient of viscosity. Importantly the radius and density of the olivine, orthopyroxene and Cr-spinel crystals are the two competing characteristics. Although Cr-spinel has a higher density (ρ_{chr}~4.5 g/cm^3) than the olivine (ρ_{ol}~ 3.3 g/cm^3) and the orthopyroxene (ρ_{opx}~ 3.2 - 3.55 g/cm^3), Cr-spinel typically has a much smaller radius. Thus from Stokes equation the radius of the settling particle is more significant than the density when comparing the settling behaviour of two or more particles with dissimilar radii. Therefore the larger olivine crystals would settle fastest and thus in this model should accumulate at the base of the layer, rather than the Cr-spinel. The extent of convection within the magma chamber should also be considered as this may hinder the settling of any and all particles. (Eales and Cawthorn, 1996; Manoochehri and Schmidt, 2014).

A further problem not accounted is the occurrence of chromitites on overturned sidewalls (Figure 1.5) as this cannot form through settling of crystals. Nex (2004) suggested an analogy with soft sediment deformation, however Glazner (2014) contradicts this, saying that the processes of soft sediment deformation in water-rich materials cannot be used as an analogy for the interaction between magmas and particles (crystals) due to the differences in viscosity and crystals will react with the magma, they are not inert like sand in water.

1.6.2 Magma Mixing or Contamination

This model was first proposed by Irvine (1975) suggesting that contamination of a mafic magma (Figure 1.6, M1) by siliceous magma (Figure 1.6, M2) from the digestion of granitic roof rock would form a hybrid magma (Figure 1.6, M3) that would be Cr-spinel saturated.

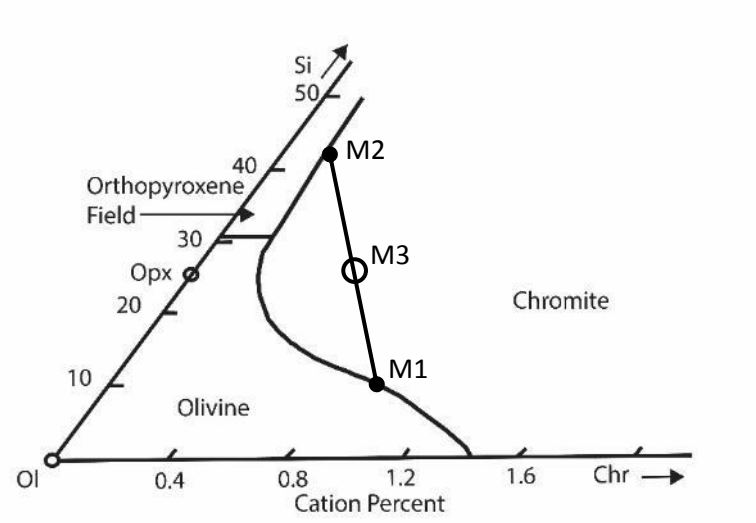

Figure 1.6: Phase diagram showing the cotectic curve and the hypothetical mixed magma composition (M3, M3 = M1 + M2) (Irvine, 1977)

There is chemical evidence for crustal contamination of the Bushveld Complex, as the cumulates have a strong crustal signature in the trace element characteristics e.g. elevated Ce/Sm, Th/Hf, $^{87}Sr/^{86}Sr_i$, high $^{187}Os/^{188}Os_i$, low ε_{Nd} and enrichment in large ion lithophile elements (LILE) and other incompatible trace elements (Maier et al., 2013). Units in the eastern and western limb of the BC that occur at equivalent stratigraphic heights have essentially identical $^{87}Sr/^{86}Sr_i$ isotopic ratios particularly in the Upper Critical Zone, Main Zone and Upper Zone (Kruger, 1994), indicating that contamination

occurred before the final emplacement. Latypov et al. (2015) suggested that assimilation played a role in maintaining magma superheating which they suggest is crucial to explain the presence of potholes and erosional features of the reef rocks with their respective footwall. The assimilation is also a possible mechanism for precipitation of Cr-spinel as the first liquidus mineral phase.

Irvine, 1977 revised his early work proposing that the contamination of the mafic magma by silica would enrich the magma in alkalis to such an extent that it would push the orthopyroxene-chromite cotectic in the MgO-Cr_2O_3-SiO_2 ternary diagram to the SiO_2 end (Figure 1.6 andFigure 1.7). Thus an abnormally high degree of contamination would be required for Cr-spinel crystallisation. Spandler et al. (2005) who studied inclusions within Cr-spinel from the Stillwater Complex (Montana, USA). The mineral compositions found in the inclusions are different from what would be expected to have formed from the proposed parental magma. As such the authors interpreted the presence of exotic minerals of albite, enstatite, diopside, Na-phlogopite and Na-Ca amphibole to represent variable amounts of mixing between a high Mg basaltic magma and a trondhjemitic magma, however, failed to address the problem of the cotectic shifting when contaminated by a felsic magma. However, the contamination proposed by Spandler et al. (2005) should have crystallised more forsteritic olivines than those observed in the Stillwater Complex, according to modelling by Mondal and Mathez (2007). Naldrett et al. (2009) suggested that contamination could result in Cr-spinel crystallisation however modelling indicated (Naldrett et al., 2012) that contamination of Critical Zone magma with a felsic melt would induce sulphide immiscibility rather than Cr-spinel crystallisation.

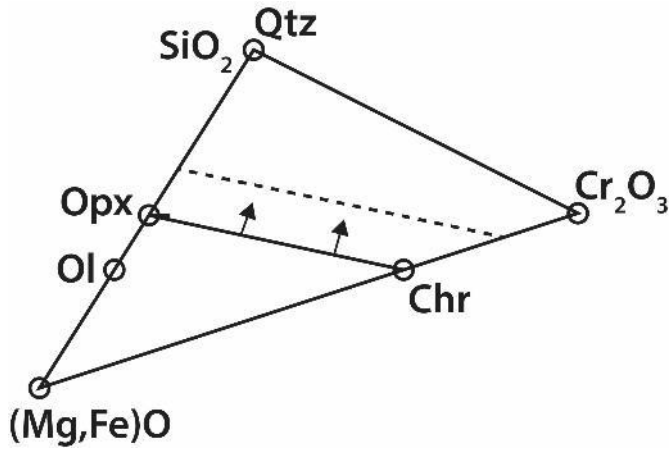

Figure 1.7: MgO-Cr2O3-SiO2 ternary diagram showing the position of Cr-spinel, orthopyroxene and quartz. The solid line representing the orthopyroxene-chromite cotectic, whereas the dotted line and arrows represents the direction of migration of the cotectic, suggested by Irvine due to contamination of a mafic magma by silica (Irvine, 1977).

Kinnaird et al. (2002) studied the bulk rock initial Sr-isotope composition of the silicate host rocks and plagioclase separates from chromitites. They found a sharp discontinuity in the Sr isotope ratios of plagioclase crystals between the chromitites and underlying silicates for UG-1 and UG-2. The Sr isotope ratios gradually evolve through the chromitite reefs with the top of the reefs having similar Sr isotope ratios to the overlying silicate rocks. The sharp discontinuity in the Sr isotope ratios is attributed to contamination by siliceous roof rocks. Kinnaird et al. (2002) proposed that the contamination occurred when a new magma influxed turbulently through the residual liquid as a fountain and interacted with the overlying felsic roof rocks, along with simultaneous mixing with the resident magma (Figure 1.8). Kinnaird et al. (2002) suggested this resulted in crystallisation of Cr-spinel alone, which settled to the floor, together with a small amount of trapped magma that formed the interstitial silicates with enriched Sr isotopic ratios. The less enriched Sr isotope composition of the hanging wall rocks indicates that they formed from an uncontaminated magma with a differing composition to the magma that formed the chromitites. O'Driscoll *et al*. (2010) supports the contamination model, proposing that assimilation of a plagioclase-rich floor rock by an intruding magma may trigger Cr-Al spinel saturation. They proposed this developed the thin chromitite stringers in the Rum Eastern Layered Intrusion (Scotland).

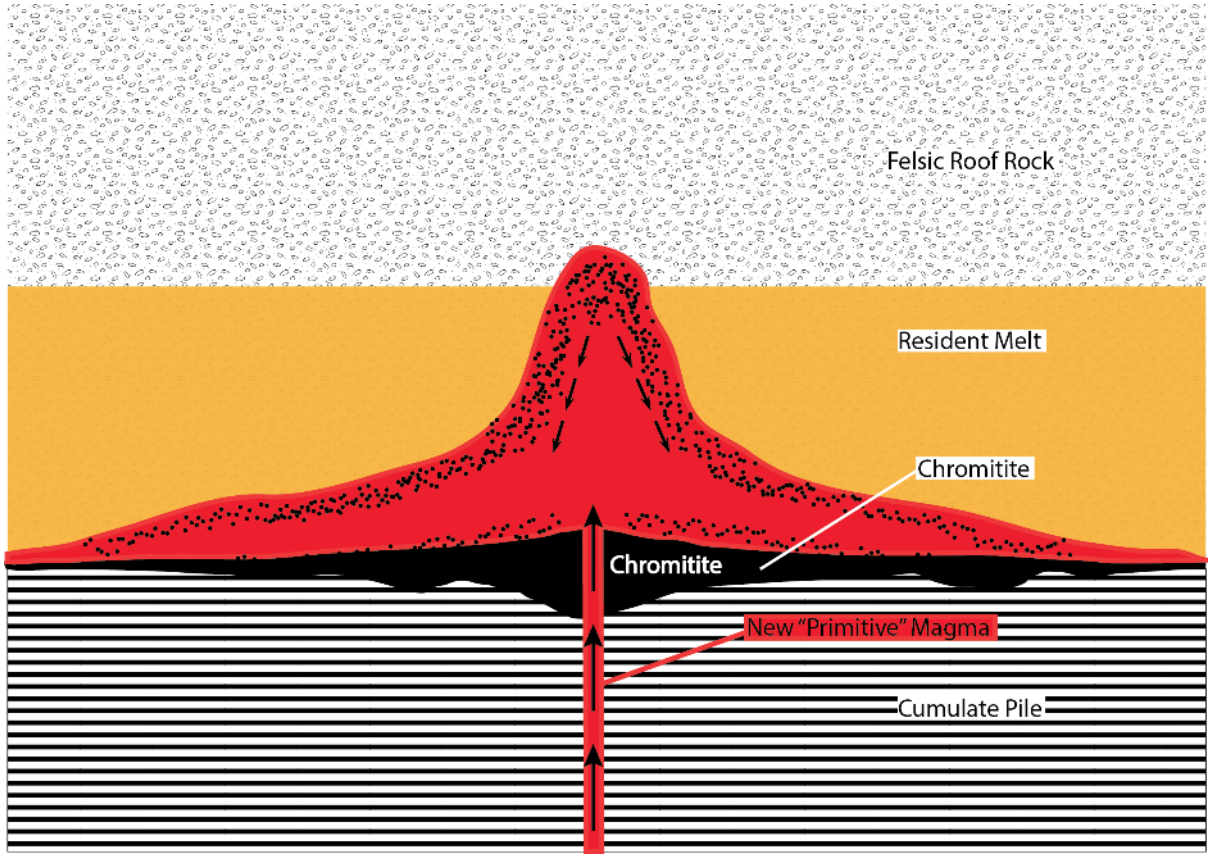

Figure 1.8: Diagram of magma mixing model with felsic roof rock contamination causing Cr-spinel crystallisation within the hybrid magma (adapted from Kinnaird et al. (2002b)).

1.6.3 Ephemeral pressure increase

This model was originally proposed by Cameron (1977) proposing crystallisation began due to an increase in pressure within the magma chamber (Figure 1.9). Further work by Lipin (1992) provided evidence for pressure changes of 5 - 10 %, based on analogies with the summit chambers of Kilauea and Krafla volcanoes. The pressure changes are attributed to the nucleation of CO_2 bubbles in the magma, which increase in volume by a factor of 4-6 as they rise up through the chamber (Figure 1.10) (Lipin, 1992). This method has the advantage of affecting the entire magma chamber simultaneously (Mondal and Mathez, 2007) thus can account for the lateral extent of the BC chromitites. However, neither the phase boundaries nor Cr solubility appear to be affected by changes in total pressure (Mondal and Mathez, 2007). Experimental work by Roeder and Reynolds (1991) indicates the Cr solubility may actually increase with pressure and not decrease (Mondal and Mathez, 2007).

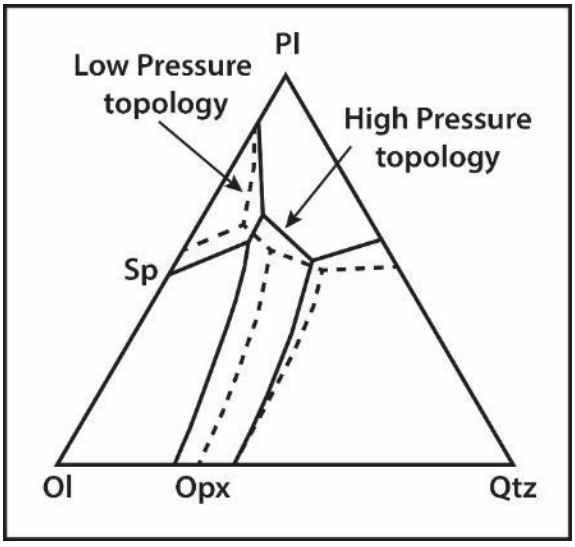

Figure 1.9: Ternary phase diagram showing the phase boundaries at high (solid) and low pressure (dashed). Note how a magma crystallising spinel, olivine and plagioclase at low pressure would crystallise only spinel at higher pressure from adapted from Lipin (1992)

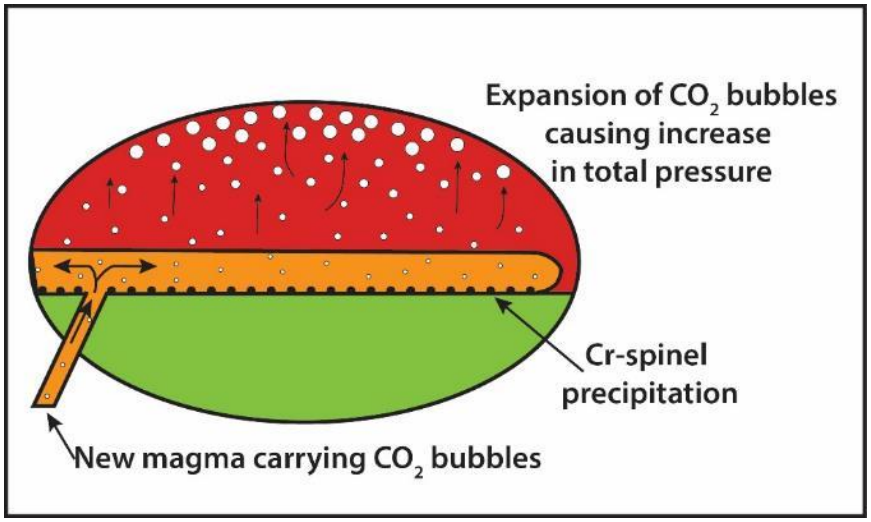

Figure 1.10: Model showing injection of a CO_2-rich magma into the chamber. The entire magma chamber experiences a pressure increase due to the concurrent rise and expansion of CO_2 bubbles. This results in crystallisation of Cr-spinel (adapted from Latypov et al, 2015)

1.6.4 Addition of H_2O

Nicholson and Mathez (1991) proposed that the chromitite layers of the Merensky reef were formed by a hydrous interstitial melt occurring between the partially molten pyroxenite hanging wall and the partially molten norite footwall (Figure 1.11). Succeeded by vapour migrating upwards through cracks in the partially molten norite, however the fractures are unable to propagate through the melt rich horizon between the partially molten norite and pyroxenite. This caused the vapour to accumulate between them in the melt rich horizon. The volatiles in combination with the melt postulated to cause the crystallisation of chromitite at the contacts with the partially molten norite and pyroxenite.

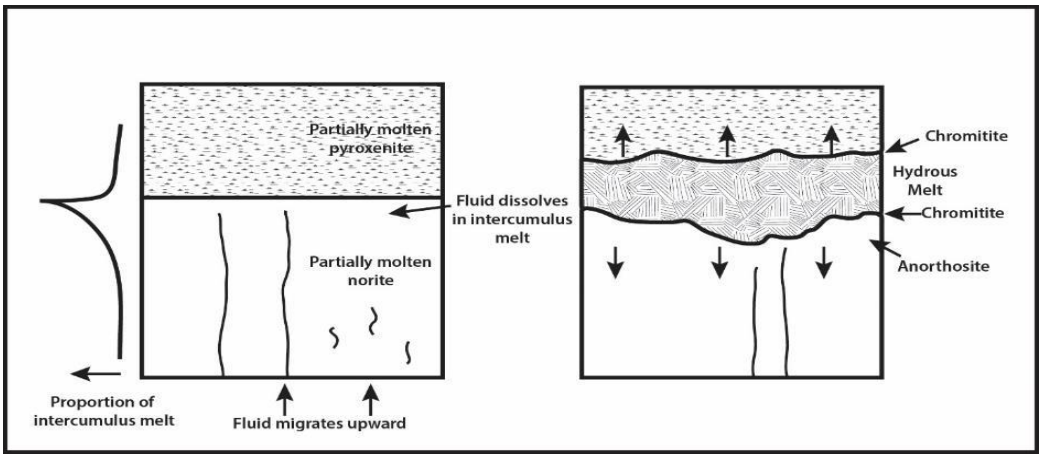

Figure 1.11: Migration of vapour to produce hydrous melt (Nicholson & Mathez, 1991)

This was based on experiments by Ford et al (1972) which have since been verified by experiments by Gaetani et al (1994). Who showed that adding water to a silicate melt would subdue the crystallisation temperature of the silicates more so than that of Cr-spinel.

The problem with this model is that it would require the dissolution of large amounts of the host rock (~50 times the volume of the Cr if dissolving Clinopyroxene and ~100 times if dissolving orthopyroxene) (Mondal & Mathez, 2007). In the case of the thicker chromitite layers such as the UG-1 it would need to not only dissolve ~100m of partially molten rock, but also extract and concentrate the Cr-spinel. This alone seems geologically unreasonable, but then it also requires the addition of a large mass of water to a partially molten rock pile (Mondal & Mathez, 2007).

1.6.5 Addition of magma with suspended Cr-spinel crystals

Mondal and Mathez (2007) proposed that the chromitites developed from accumulation of suspended Cr-spinel crystals sourced from newly emplaced magma. This mechanism can develop chromitites with nearly identical hanging wall and footwall compositions, which is what Mondal and Mathez (2007) found when studying mineral chemistry of the UG-2 and the host rock. Minor differences in chemistry and petrography are attributed to an impermeable chromitite layer trapping interstitial or percolating fluids beneath it (Mondal and Mathez, 2007). The model indicates the reef should have a totally different geochemical signature to the hanging wall and footwall, unless the accumulated Cr-spinel crystals are derived from the same parental magma as the host rocks. This model deals with the mass balance problem, but does not explain what happens to the residual magma after the chromitite layer has formed. It also requires crystallisation of Cr-spinel in a deeper staging chamber below the main Bushveld chamber (Figure 1.12). Mondal and Mathez (2007) suggests that there is “ample geochemical evidence” for a deeper chamber based on phenocrysts including Cr-spinel phenocrysts seen in lavas and hypabyssal bodies such as the Ferrar dolerite sills of Antarctica (Marsh, 2004), however they do not provide further specifics. Even if there is a deeper staging chamber, a mechanism is still required to explain either the sole crystallisation of Cr-spinel or a method of separating the Cr-spinel from other crystallising phases in the staging chamber.

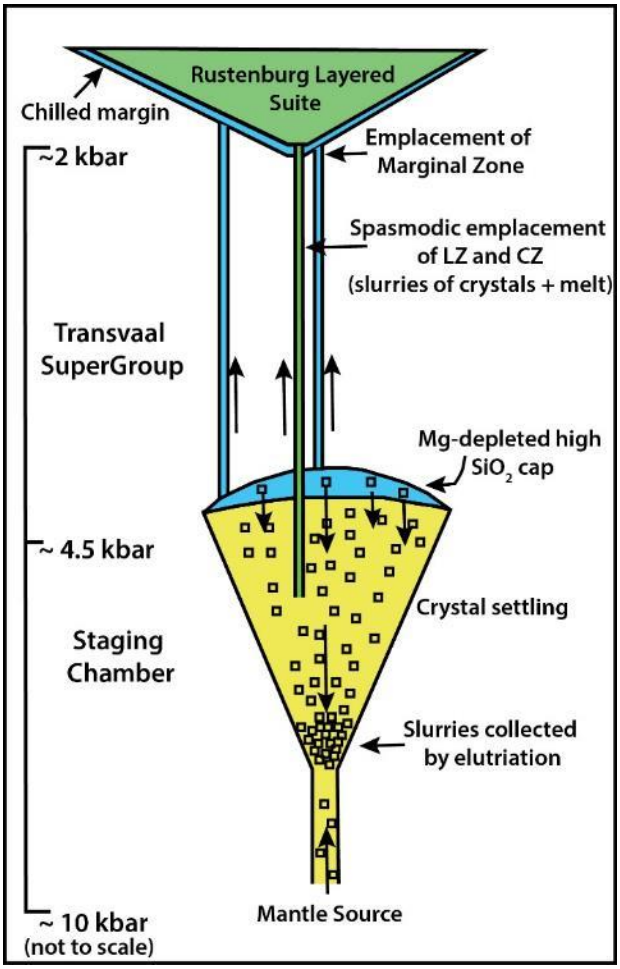

Figure 1.12: Diagram of a model proposed by Eales and Costin (2012), showing a staging chamber that allowed for the formation of a SiO_2-rich cap as well as crystallisation of Cr-spinel. The SiO_2-rich cap is emplaced as the Marginal Zone with the slurry + residual magma representing the chromitite layers and the Lower and Critical Zone (adapted from Eales and Costin, 2012).

1.6.6 Addition of crystal-poor, Cr saturated magma

Naldrett et al. (2012) postulated that there was an addition of a new magma into the resident magma chamber which had chromite as the sole liquidus phase. More recently Latypov et al (2017) (in press) also invokes the addition of chromite-saturated magma. The amount of chromitite present in the reefs could be explained by the addition of a Cr saturated magma during a recharge event occurring as a basal flow, as this would help solve the mass balance problem when crystallising the chromitite. This model would account for why the chromitites have a different geochemical signature to the underlying and overlying silicates, as they would crystallise in situ from the new magma (Latypov et

al, 2017, in press). They therefore would not follow a fractional crystallisation trend going from the footwall into the reef and then the hanging wall.

1.6.7 Lateral variations across the western limb

Previous work by Eales et al (1988, 1993) postulated a proximal and distal facies for the western limb of the BC with the northern portion (Union) being proximal and the south eastern portion of the limb (towards Brits) being distal. This is based on borehole core observations and chemical variations within horizons of the Critical Zone, including thinning of individual chromitite and olivine-rich layers within the Lower Critical Zone and decreasing whole rock MgO contents in a southerly direction. There is also a progressive decrease in the Mg# (Mg^{2+}/ (Mg^{2+}+Fe^{2+})) of orthopyroxene and olivine within cumulates from Union section south towards Rustenburg.

The proximal-distal idea proposes that there is a feeder zone/pipe situated near the proximal Union section. This theory was considered because it uses the concept of crystallisation occurring at the front of an incoming magma pulse concurrently the crystallisation is considered to be fractional and this is used to explain the lateral variation going from the proximal Union section towards the distal Brits (Eales et al, 1988). However the proximal to distal concept is flawed because the rate of magma flow is much greater than the rate of crystallisation. Magma influx flow rates are in the order of $m.day^{-1}$ to $km.day^{-1}$ compared to crystallisation rates of $mm.year^{-1}$ to $cm.year^{-1}$ (Latypov et al., 2017). Thus the entire magma chamber floor would be covered before any significant crystallisation occurs.

1.6.8 Magma stratification

Magma stratification has not been used before as a mechanism for the formation of chromitite layers, however it is necessary to have a basic understanding of how it works for future discussion. Magma stratification can develop when a new more primitive magma is introduced into the magma chamber. The two magmas have different chemistries and temperatures, leading to the formation of individual convection cells due to the unstable thermal profile (Figure 1.13) (Campbell and Turner, 1986). Crystallisation occurs at thermal boundaries, thus Cr-spinel can crystallise at the base of the cell adjacent to the cumulate pile. As Cr-spinel crystallises, the composition and temperature of the cell become similar to that of the cell above, this causes the two cells to mix (Campbell and Turner, 1986).

The mixing of the two cells keeps Cr-spinel crystallising as the composition of the “new” bottom cell becomes similar to the cell above it the process is repeated.

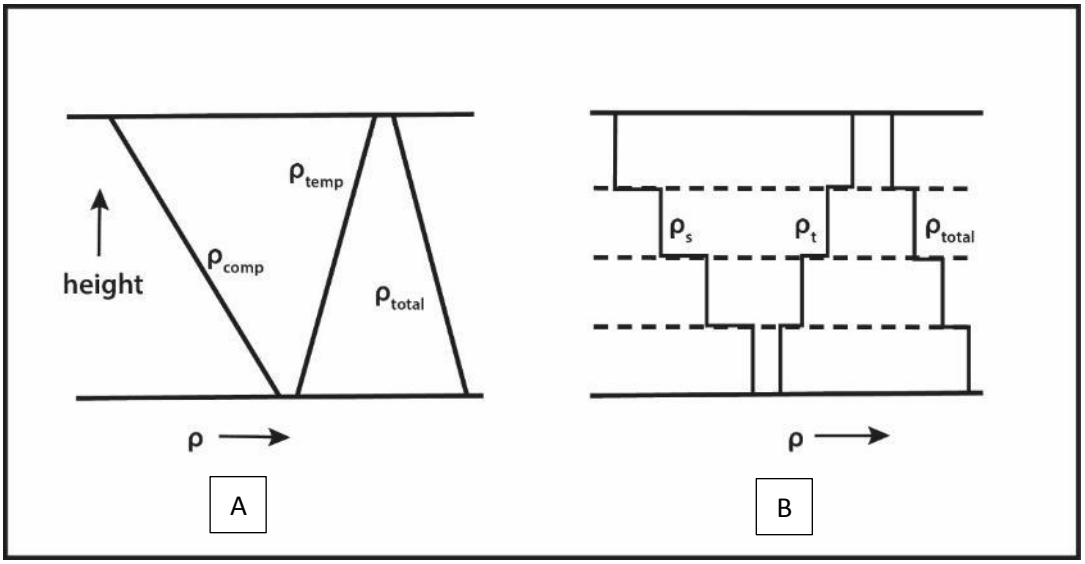

Figure 1.13: A) Distribution of density due to composition and temperature in a fluid layer before it breaks up into double diffusive convection cells. The density distribution of heat which is the faster diffusing component is destabilising, however the overall density gradient is stable (Campbell and Turner, 1986). B) The system in 2.12A breaks up into a series of double diffusive convecting layers, which are driven by the release of potential energy from the unstable distribution of the faster diffusing property (heat). Individual convecting cells are well mixed and are separated by thin diffusive interfaces (indicated by dashed lines), across which heat and composition are transferred by diffusion (heat more rapidly than composition (after Campbell and Turner, 1986).

1.7 Introduction to the field area

Ruighoek mine is located directly to the northwest of the Pilanesberg Intrusion, approximately 125 km northwest of Rustenburg (Figure 1.14). Previous drilling in the area identified the elevated Cr/Fe ratio, Figure 1.15 displays the locations of boreholes drilled and the inferred extent of the elevated Cr/Fe ratios in LG-6 chromitite.

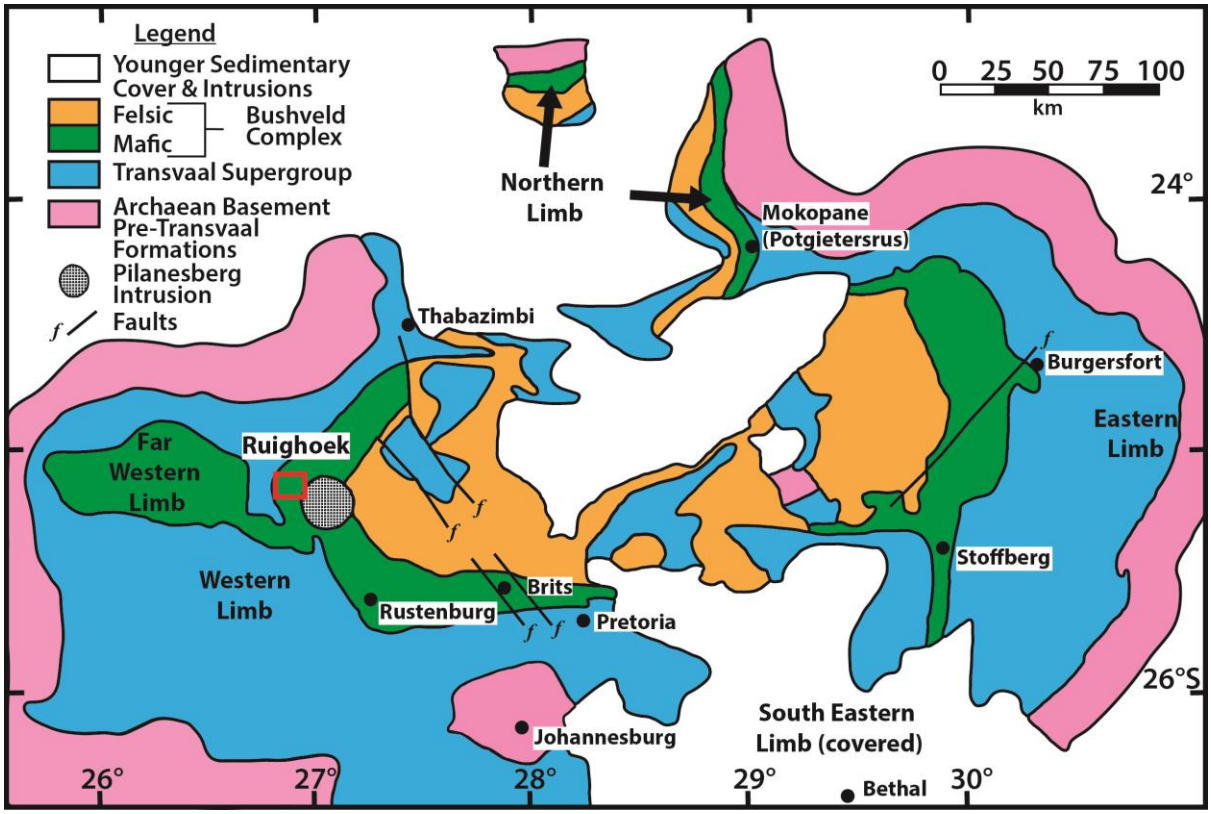

Figure 1.14: Geological map of the Bushveld Complex. Red box marking the location of Ruighoek mine. (Barnes and Maier, 2002).

The unique geochemistry of the LG-6 chromitite in its range of $Cr/Fe_{(Tot)}$ ratios and the occurrence of harzburgite rocks associated with elevated Cr/Fe ratios in the Ruighoek area provide new insight into the processes of chromitite formation through magmatic replenishment events. The elevated Cr/Fe ratio is economically significant because it means that there is more chromium per ton mined.

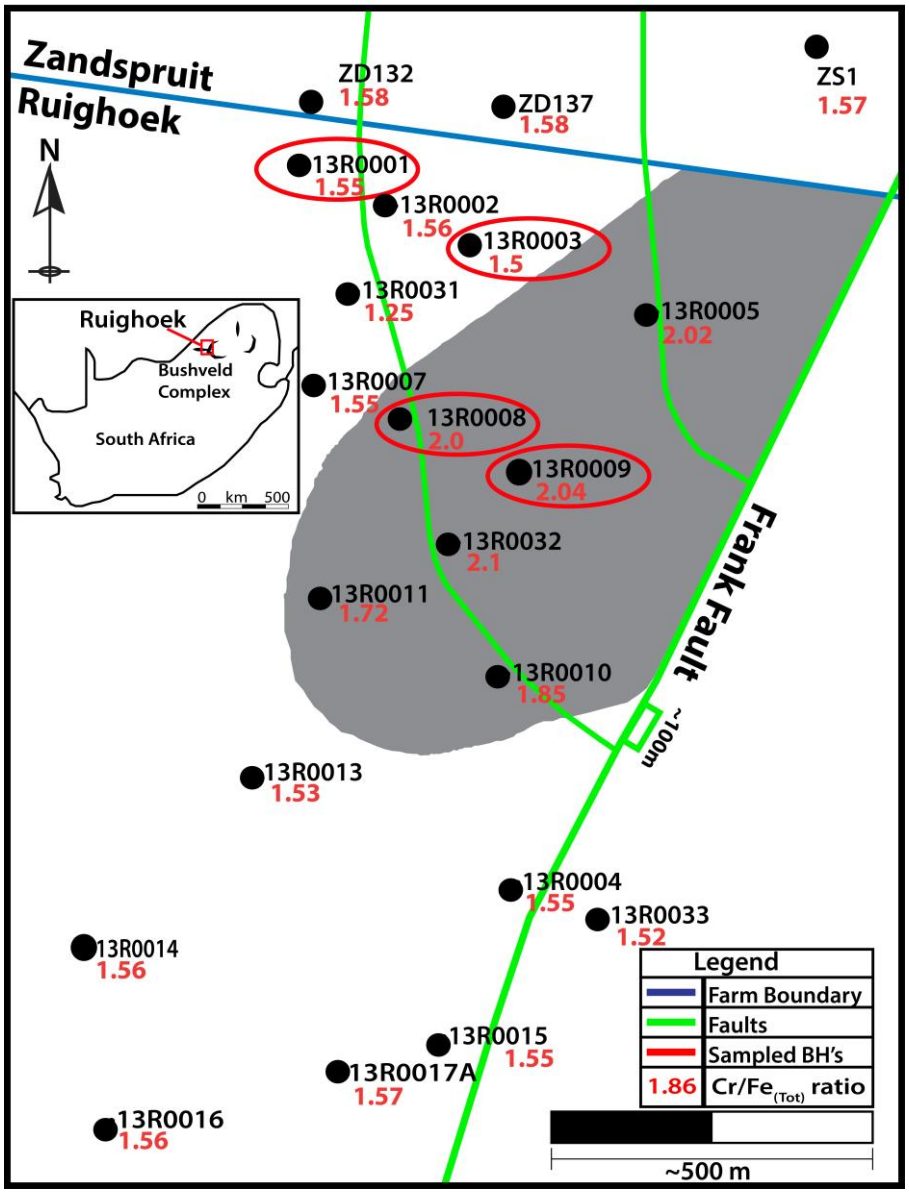

Figure 1.15: Borehole locations at Ruighoek Mine. The shaded area represents the inferred extent of the elevated Cr/Fe ratios of the LG-6 chromitite.

1.8 Aim

The generation of mineralised chromitite layers in the Bushveld Complex is currently poorly understood, with many competing models suggested in the literature [e.g. Mungall, 2002; Irvine, 1977; Nex, 2004; Mondal and Mathez, 2007; Spandler et al, 2005; Naldrett et al, 2009 & 2012; O'Driscoll et al, 2010; Latypov, 2015; McDonald, 1965; Lipin, 1992; Campbell & Turner, 1986]. This project will contribute to the understanding of chromitite formation through a detailed petrological and geochemical study of the LG-6 chromitite layer at Ruighoek mine, in the western limb of the Bushveld complex (Figure 1.14).

1.9 Structure of the thesis

This study has three principal objectives within the evaluation of the processes involved in the formation of the LG-6 chromitite in the Ruighoek area. Any lateral variation in composition of the LG-6 reef will be determined through detailed petrographic analyses combined with whole rock and mineral chemical analyses. Compositional variations will be spatially plotted across the Ruighoek area to identify any trends. These data will be used to evaluate previously published models for chromitite formation.

Chapter 2 covers sampling techniques, the different methods used and how they work and illustrates the spatial variations in the topography of the LG-6 chromitite reef and associated geochemical variations. Chapter 3 contains all the petrographic observations and a description of the lithologies that occur in the two boreholes (13R-3 and 13R-9). Chapter 4 describes the different geochemical datasets, including the whole rock geochemistry which included analysis of chromitite samples for 6 PGEs (platinum group elements) and mineral chemistry through EPMA (Electron Probe Micro Analysis). Chapter 5 will interpret the data from the previous chapters and finally Chapter 6 concludes and provides suggestions for future work.

Nomenclature: To avoid confusion with the geological and mining terminology that are variably interchanged, this thesis applies the following terms. The term “reef” refers to horizons of economic value and in this thesis typically refers to the LG-6 chromitite. The main reef is the LG-6 reef and the overlying, thinner leader reef is referred to as LG-6A. Due to the presence of two reef bodies, the term “middling” is used to refer to the silicates sandwiched between the reefs. “Hanging wall” refers to the host rocks directly above the LG-6A reef. “Footwall” applies to the rocks directly below the LG-6 reef. Cr/Fe means $Cr/Fe_{(Tot)}$ for both whole rock and mineral geochemistry throughout this thesis unless stated otherwise.

2. Methods and Modelling

In the study area of Ruighoek, LG-6 and LG-6A are ~75 cm and ~25 cm thick respectively and the two chromitite layers are separated by 15 metres of orthopyroxenite. Samples were collected from Ruighoek Mine, using borehole cores from both 'normal' (not elevated) LG-6 as well as from the area of LG-6 that displayed elevated Cr/Fe ratios (Figure 1.15).The horizontal distance between the two boreholes is approximately 500 metres.

2.1 Sampling technique

Bulk samples were collected from a number of cores through the footwall silicates, LG-6 chromitite, middling, LG-6A chromitite reef and the hanging wall silicates.

Half cores (47.6 mm diameter) from boreholes 13R0001, 13R0003, 13R0008 and 13R0009 (Figure 1.15) were sampled continuously through the reef and at a 1 – 2 metre spacing in the host silicate rocks. Boreholes 13R0001 and 13R0003 were chosen to represent normal LG-6, with Cr/Fe ratios of 1.55 and 1.50, respectively. Boreholes 13R0008 and 13R0009 were chosen to represent the enriched LG-6, with Cr/Fe ratios of 2.00 and 2.04, respectively.

LG-6 chromitite in cores 13R0003 and 13R0009 was sampled every 2.5 to 4.0 cm, with the use of a thin blade to reduce loss of core. 1/3 of each sample was retained for sectioning, the remaining 2/3 (> 50 grams) were used for whole rock analysis including PGE abundances. 13R0003 was subdivided into 45 samples and 13R0009 into 52 samples.

A second sampling excursion was done with a more general focus of the area in mind. The point was to collect reef samples from several boreholes in the area, namely the LG-6A, LG-7, MG-1. MG-2 (A & B) and MG-4 (A, B & C). See Appendix J for details regarding samples collected. The idea was to determine if there is a spatial relationship between the geochemistry of each reef and its respective topography.

2.2 Petrographic Analysis

Petrographic analyses were performed under transmitted and reflected light to identify mineral phases, modal proportions and identify textural relationships.

2.3 Whole rock methodology

Major and trace elements were analysed by the Genalysis Intertek laboratory in Australia. The whole rock major element analyses were performed through X-ray fluorescence (XRF) of compressed powder disks. Loss on ignition (LOI) was obtained through thermogravimetry and calibrations were performed with the use of international standards SARM, SY and AMIS (Table 2.1). Trace element compositions were determined using inductively-coupled plasma optical emission spectrometry (ICP-OES) and inductively-coupled plasma mass spectrometry (ICP-MS) with four acid digests at 3000 times dilution. High concentrations of Cr-spinel in the reef samples resulted in small residues of undisolved Cr-spinel, thus these samples underwent a further 10 times dilution to obtain consistent reliable trace element data using ICP-MS. No futher dilution was necessary for analysis through ICP-OES which has a greater tolerance for total dissolved solids. Calibrations were performed with the use of international standards AMIS for ICP-MS and OREAS for ICP-OES (Table 2.1). Due to the additional dilution for ICP-MS the following elements are either below, or close to, the detection limit: Ag, As, Be, Bi, Cd, Cs, Eu, Hf, Ho, In, Lu, Mo, Nb, Pb, Re, Sb, Se, Sn, Ta, Te, Th, Tl, Tm, U and W.

Nickel sulphide collection fire assays were used for determining PGE abundances with international rock standards AMIS run as unknowns for assessment of analytical recovery (Table 2.1 & Appendix D).

Table 2.1: International standards used for calibration of analyses.

Standard	Instrument
SARM 1, 2, 8 & 9	XRF
SY 4	XRF
OREAS 45d, 45e, 13b & 73b	ICP-OES & ICP-MS
AMIS 0170 & 0171	ICP-OES & ICP-MS
AMIS 0323	XRF
AMIS 0132	XRF, ICP-OES & ICP-MS
AMIS 0278 & 0010	PGE's

Two sigma (2σ) and analytical recovery (AR) calculations can be found in Appendix D.

2.4 Scanning Electron Microscope (SEM)

The FEI Quanta 200 ESEM was used at the University of the Witwatersrand to identify whether compositional zoning was present in olivine, orthopyroxene and Cr-spinel, as preliminary work for the EPMA. This was completed using back-scattered electron (BSE) images combined with semi quantitative energy-dispersive x-ray spectroscopy (EDS). Operating conditions used an acceleration voltage of 30.00 kV, a working distance of 10.3 mm and each EDS point was analysed for 30.0 seconds.

2.5 Electron Probe Microanalysis (EPMA)

Electron probe microanalysis was performed using the Cameca SXFive-FE electron microprobe equipped with 5 WDS spectrometers at the University of the Witwatersrand. Targeted olivine, orthopyroxene and Cr-spinel crystals were analysed using an acceleration voltage of 15 kV and a focussed beam with a current of 20 nA. Counts times were 20 seconds on peak and background measurements were half of the peak times. A mix of natural and synthetic standards were used for calibration. Formulae of olivine were recalculated based on 3 cations and 4 oxygens; orthopyroxene

using 4 cations and 6 oxygens; and Cr-spinel using 24 cations and 32 oxygens. $Fe_{(T)}$ was corrected to Fe^{2+} and Fe^{3+} through the Droop (1987) method.

2.6 Surfer Modelling

Surfer 8 published by Golden software was used to visualise the spatial relationship between the reef topography and the noted chemical variations. To model the data, the kriging gridding method was applied, each of the layers had a different line spacing and a varying number of lines dependant on the number of data points. Kriging was used as it produces the best representation when dealing with a small data set.

2.6.1 Spatial variation in chemistry of the LG-6

3D modelling was used to help visualise the spatial relationship of the boreholes and their different chemistries, the borehole co-ordinates used in the model can be found in Appendix H.

The topography of the LG-6 has a regional dip of east, with a depression near the centre of the model (Figure 2.1). The depression coincides with an elevated Cr/Fe ratio for the LG-6 which is represented by the blue to red (low to high) coloured contour map (Figure 2.2) which overlies the topography wireframe model.

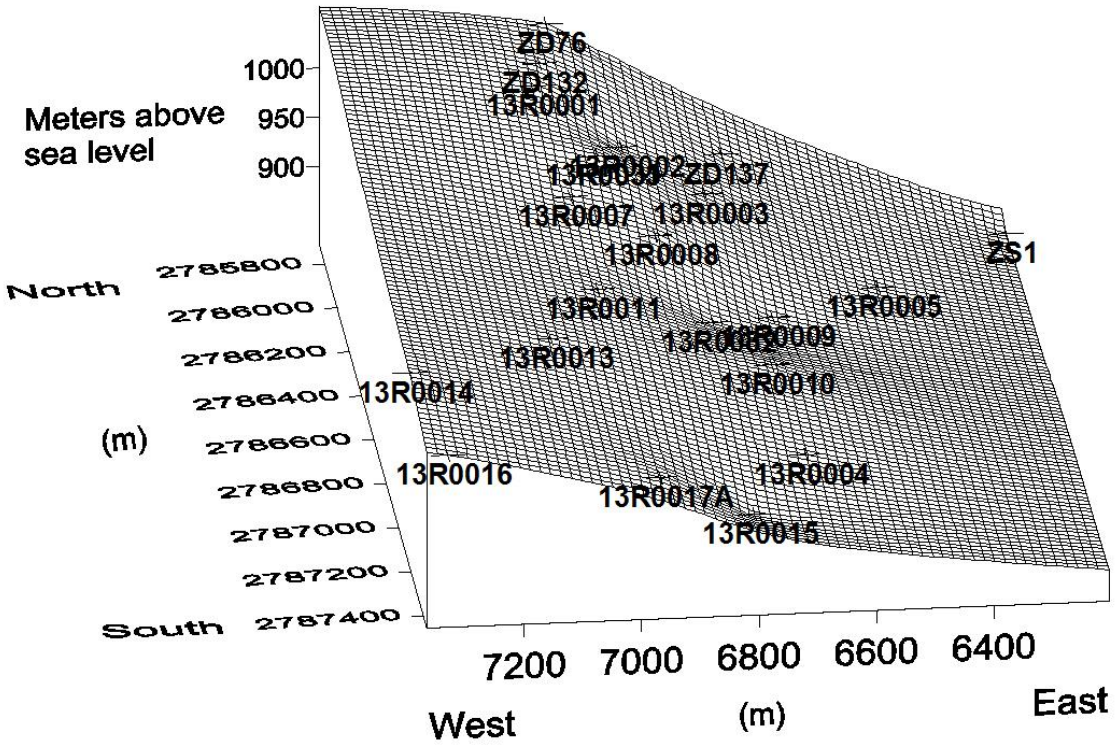

Figure 2.1: Wireframe model of the LG-6 topography

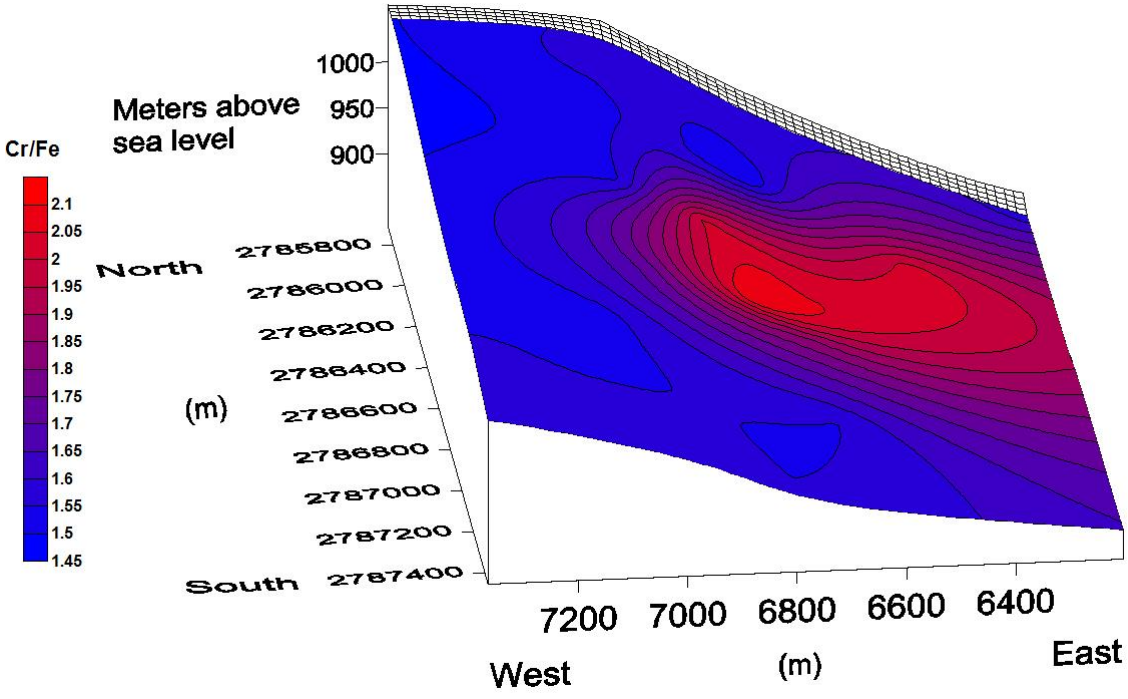

Figure 2.2: Wireframe model of the LG-6 chromitite with the Cr/Fe ratio overlain

The depression circular in shape and approximately 250 m in diameter with a depth of 30 m (below that of the expected elevation).

3. Petrography

3.1 Introduction

Nomenclature: The terms 13R-3 and 13R-9 refers to two separate boreholes 13R0003 and 13R0009 respectively (Figure 1.15).

The footwall, middling and hanging wall lithologies of the chromitite reefs are typically composed of orthopyroxenite as typified by borehole 13R-3. Borehole 13R-9 which is in the NE of the Ruighoek area has local occurrence of harzburgites in the hanging wall, middling and footwall of the LG-6. The LG-6 chromitite is typically massive and comprised of >90% Cr-spinel. Table 3.1 and Table 3.2 at the end of each of their respective sub chapters summarise the lithologies in each of the boreholes.

3.2 Borehole 13R-3

3.2.1 Hanging wall

Predominantly composed of orthopyroxene with disseminated Cr-spinel and interstitial plagioclase and clinopyroxene (Table 3.1). Orthopyroxene crystals are euhedral to subhedral and range in size from 0.5 mm to 3 mm and frequently display exsolution lamellae of clinopyroxene. The disseminated Cr-spinel crystals increase in abundance downwards towards the LG-6A chromitite reef. Cr-spinel crystals predominantly occur along orthopyroxene crystal boundaries (Figure 3.1), however occasionally occur as inclusions within orthopyroxene and to a lesser extent plagioclase (Figure 3.2). Cr-spinel crystal sizes range from 0.1 mm to 0.6 mm. Plagioclase commonly displays characteristic multiple twinning.

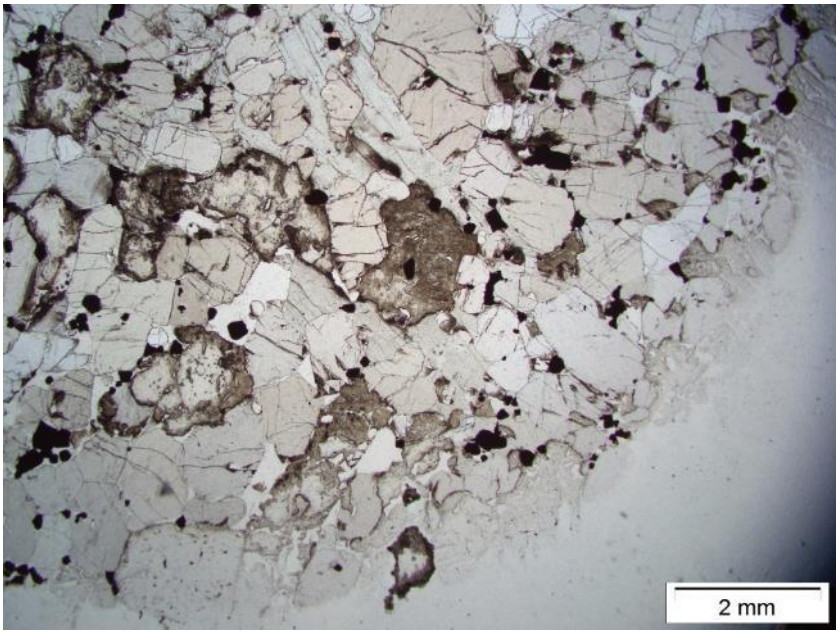

Figure 3.1: Typical orthopyroxenite with the Cr-spinel crystals (black) predominantly disseminated along crystal boundaries. Plane polarised transmitted light (sample: 13R-3/150.88 – 151 m).

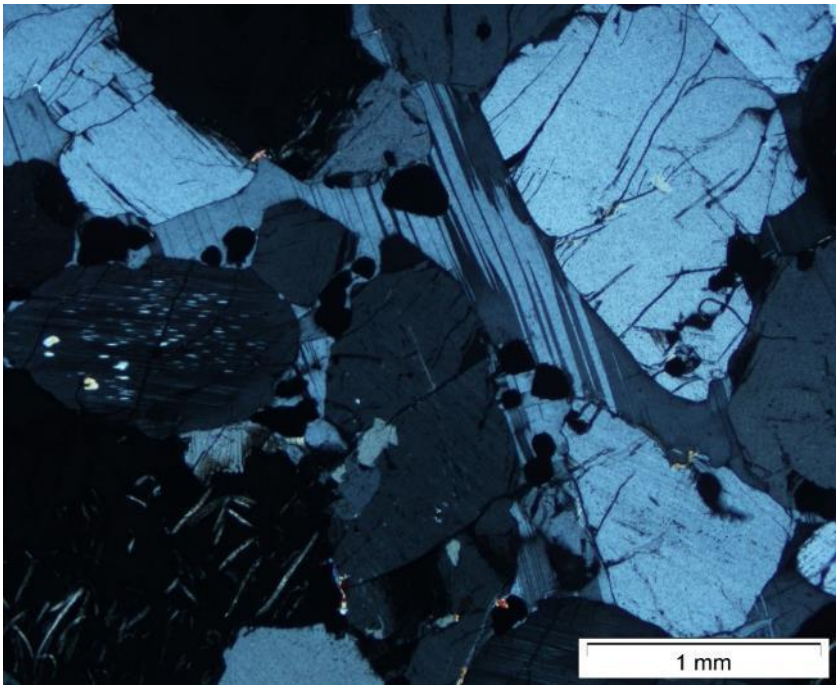

Figure 3.2: Opaque Cr-spinel crystal (black/opaque) inclusions in plagioclase (multiple twinning) and orthopyroxene (light grey). Cross polarised transmitted light (sample: 13R-3/150.88 – 151 m).

3.2.2 LG-6A Chromitite

The leader reef is primarily composed of Cr-spinel with interstitial pyroxenes mainly orthopyroxene (Table 3.1). The Cr-spinel crystals range in size from 0.05 mm up to 1.00 mm and display features of textural coarsening including annealed grains and apparent dihedral angles approaching 120°. Where the Cr-spinel crystals are texturally coarsened they display a thin alteration rim of an oxide material. The thin rim can neither be seen in transmitted light as it is opaque, nor can it be seen in reflected light as it has a comparable reflectance to that of the interstitial silicate minerals. It was identified using a combination of both transmitted and reflected light (Figure 3.3).

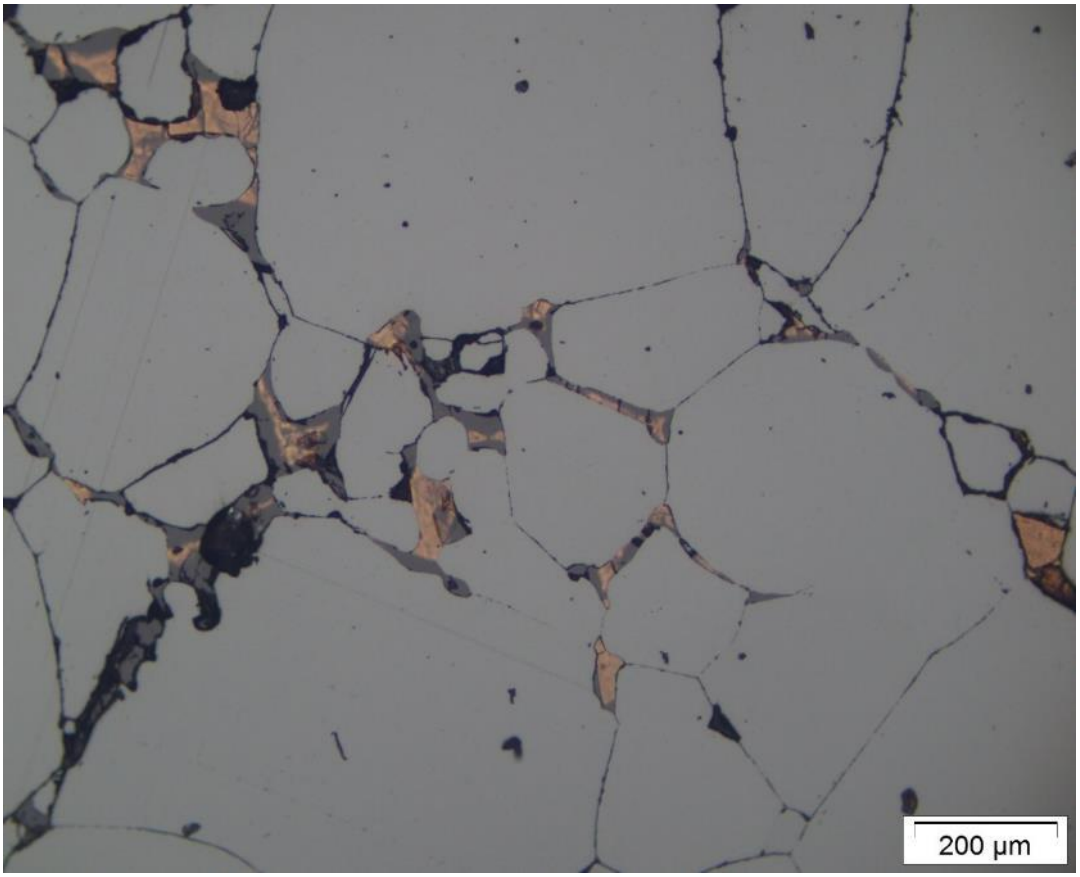

Figure 3.3: High reflectance Cr-spinel (light grey) with creamy-orange interstitial silicate and oxide rim (darker grey) around the Cr-spinel in LG-6A. A combination of plane polarised transmitted and reflected light (sample: 13R-3/152.80A).

A silicate-rich band of orthopyroxenite (75% orthopyroxene, 20% Cr-spinel, 4% plagioclase and 1% clinopyroxene) occurs ~ 3 cm above the base of the seam. The orthopyroxene crystals range in size from 0.2mm to 1.5 mm. The reef contains less than 1% sulphides, which are hosted along Cr-spinel

grain boundaries and triple junctions. In the silicate rich band the Cr-spinel is chain textured around orthopyroxene crystals and the sulphides occur as inclusions within the Cr-spinel crystals (Figure 3.4).

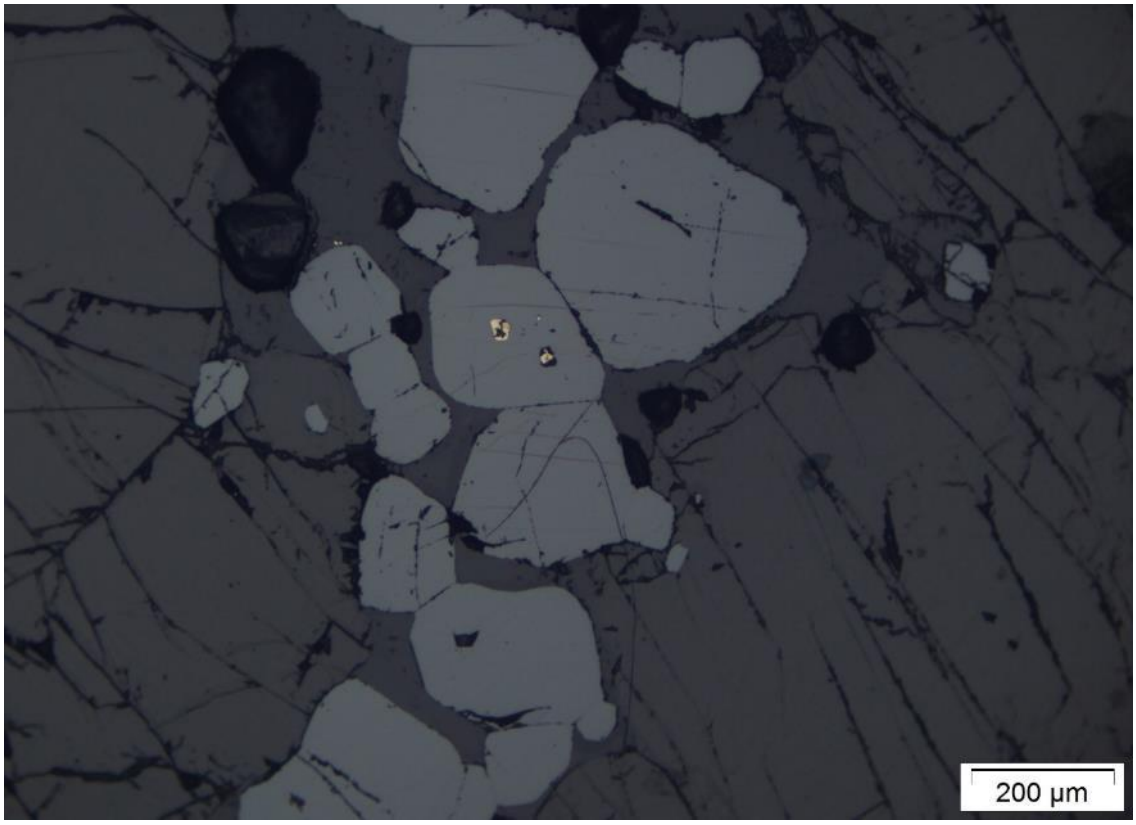

Figure 3.4: Cr-spinel (grey) displaying chain texture around orthopyroxene with sulphide inclusions (yellow). Plane polarised reflected light (sample: 13R-3/152.95A m).

3.2.3 Middling

The middling occurs between LG-6 and LG-6A (Figure 1.4), and is predominantly composed of orthopyroxene with interstitial clinopyroxene, plagioclase and disseminated Cr-spinel (Table 3.1). Cr-spinel crystals rapidly decrease in abundance downwards from the base of the LG-6A and then gradually increase again towards the top of the LG-6. The main central section is predominantly deficient in Cr-spinel with a corresponding slight increase in abundance of interstitial clinopyroxene (Table 3.1). The clinopyroxene usually forms oikocrysts (Figure 3.5) but also occurs as exsolution lamellae from orthopyroxene. Orthopyroxene crystals are euhedral to subhedral and range in size from 0.2 mm to 4.5 mm. Cr-spinel crystals range from 0.05 mm to 0.7 mm and near the reefs where their abundance increases they form chain textures around orthopyroxene. Cr-spinel crystal sizes also typically increase with proximity to the reefs.

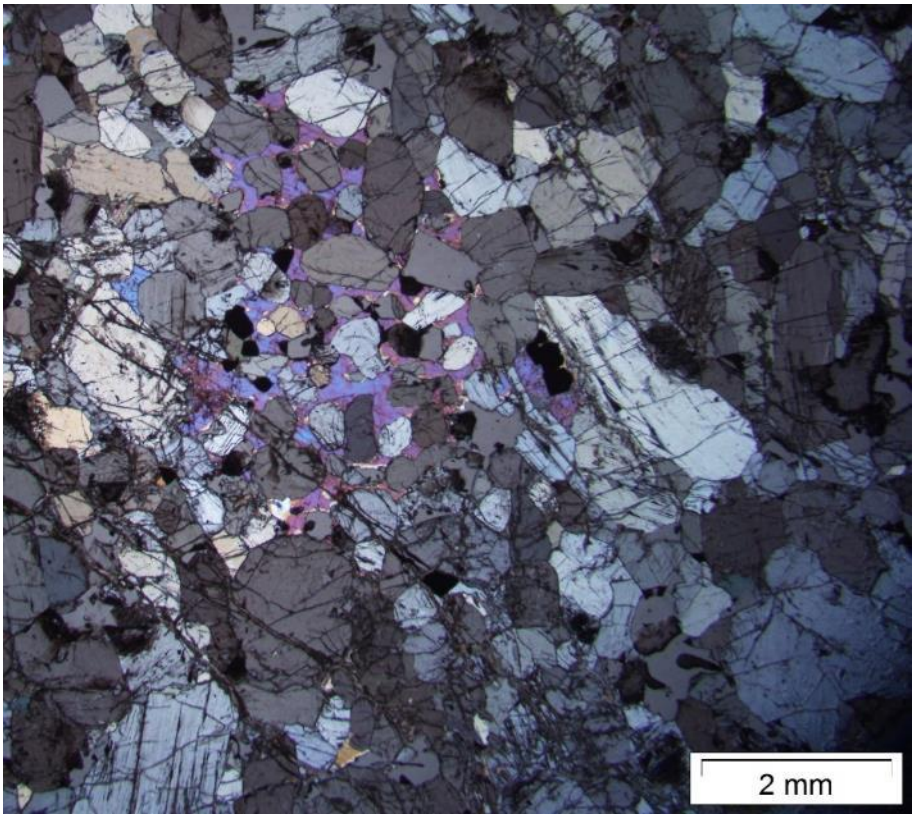

Figure 3.5: Orthopyroxenite with oikocrystic clinopyroxene (purple and blue) and disseminated Cr-spinel (opaque). Cross polarised transmitted light (sample: 13R-3/152.95E).

3.2.4 LG-6 chromitite

Predominantly composed of chromite with minor interstitial orthopyroxene and clinopyroxene (Table 3.1). Cr-spinel crystals typically range in size from 0.05 mm to 1.00 mm, some texturally coarsened areas have grains up to 1.30 mm. Sulphides form <1% of the reef.

3.2.5 Footwall

Predominantly composed of orthopyroxene with decreasing disseminated Cr-spinel away from the base of the LG-6, minor amounts of interstitial clinopyroxene and plagioclase are present (Table 3.1). Orthopyroxene crystals are euhedral to subhedral and display exsolution lamellae of clinopyroxene. Orthopyroxene crystals range in size from 0.1 mm to 3.5 mm with the mean crystal size increasing from 2.33 mm to 3.25 mm with the decreasing abundance of Cr-spinel. Cr-spinel develops a chain texture around orthopyroxene where the abundance is greater than 4%.

Table 3.1: Borehole 13R-3

Unit	Depth	Thickness	Lithology	Mineralogy
HW	150.88 m to 152.80 m	1.92 m	Orthopyroxenite with disseminated Cr-spinel	76% Orthopyroxene 16% Cr-spinel 5% Plagioclase 3% Clinopyroxene
LG-6A	152.80 m to 152.95 m	0.15 m	Chromitite	10% Orthopyroxene 87% Cr-spinel 2% Clinopyroxene
Middling 1	152.95 m to 152.99 m	0.04 m	Orthopyroxenite with disseminated Cr-spinel	49% Orthopyroxene 49% Cr-spinel 1% Plagioclase 1% Clinopyroxene
Middling 2	152.99 m to 166.78 m	13.79 m	Orthopyroxenite	88% Orthopyroxene 3% Cr-spinel 1% Plagioclase 8% Clinopyroxene
Middling 3	166.78 m to 167.46 m	0.68 m	Orthopyroxenite with disseminated Cr-spinel	74% Orthopyroxene 22% Cr-spinel 2% Plagioclase 2% Clinopyroxene
LG-6	167.46 m to 168.24 m	0.78 m	Chromitite	11% Orthopyroxene 87% Cr-spinel 1% Clinopyroxene
FW 1	168.24 m to 168.68 m	0.44 m	Orthopyroxenite with disseminated Cr-spinel	83% Orthopyroxene 11% Cr-spinel 2% Plagioclase 4% Clinopyroxene
FW 2	168.68 m to 172.00 m	3.32 m	Orthopyroxenite	87% Orthopyroxene 3% Cr-spinel 3% Plagioclase 7% Clinopyroxene

3.3 Borehole 13R-9

3.3.1 Hanging wall

Predominantly composed of orthopyroxene and serpentinised olivine with disseminated Cr-spinel and interstitial clinopyroxene (Table 3.2). The hanging wall grades from a highly serpentinised harzburgite to orthopyroxenite, then becoming a chromitiferous orthopyroxenite (Figure 3.6) nearer the LG-6A reef contact. The orthopyroxene ranges in grain size from 0.5 to 4.0 mm with varying degrees of clinopyroxene exsolution lamellae (Figure 3.7). The olivine grains range from 1.5 to 4.0 mm and are usually highly fractured and altered to serpentine and magnetite with decreasing abundance towards the reef. Cr-spinel crystals occur both at the grain boundaries and as inclusions within silicate minerals. They range in grain size from 0.05 to 0.4 mm and where their abundance is greater than 5%, the Cr-spinel form a chain texture. There is less than 0.5% sulphides and they occur either hosted within, or in close proximity to the Cr-spinel (Figure 3.8) or along/within silicate veins (Figure 3.9).

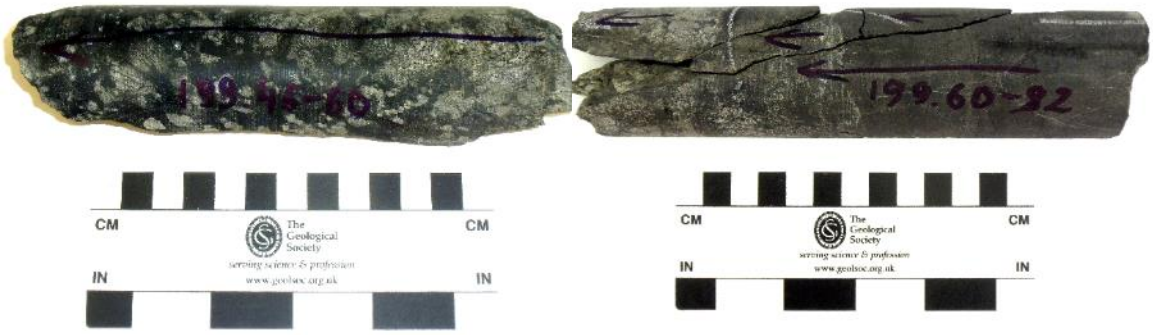

Figure 3.6: Serpentinised (black, left side) harzburgite `

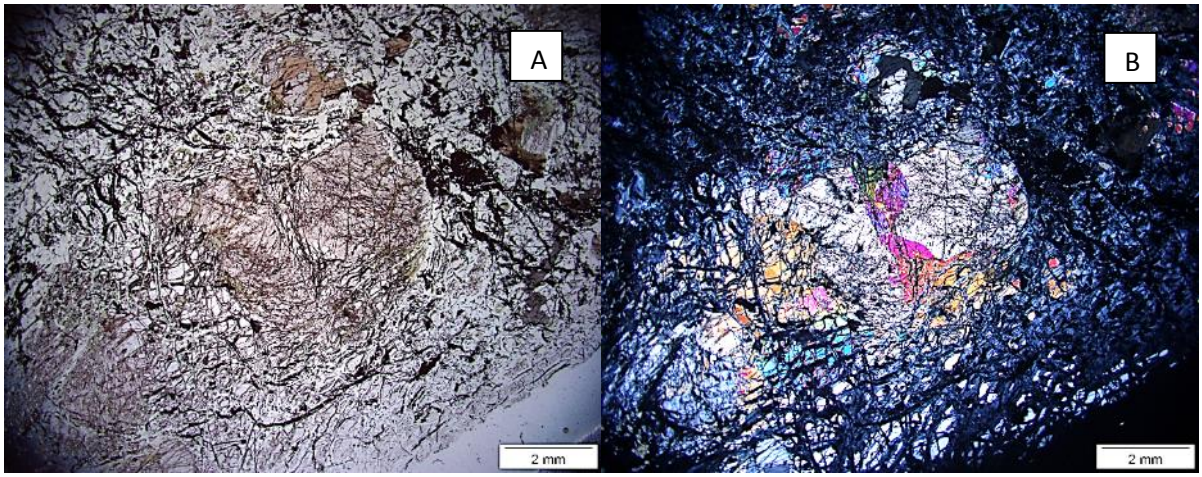

Figure 3.7: Typical hanging wall orthopyroxenite from BH 13R-9. A- PPL, Orthopyroxene (light brown, centre) surrounded by serpentine (black and white/clear). B- XPL, Orthopyroxene (light brown), Olivine (High birefringence, multi-coloured) surrounded by serpentine (black).

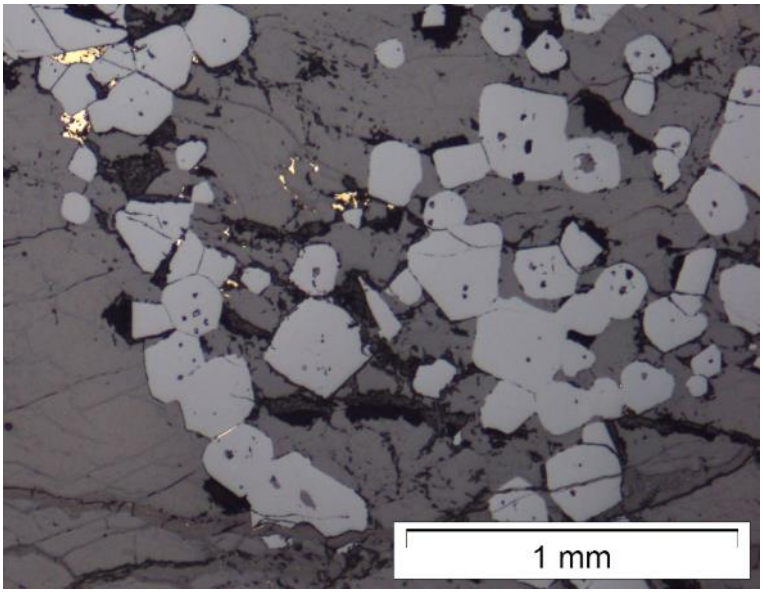

Figure 3.8: Sulphides (yellows) hosted within orthopyroxene (dark grey) and Cr-spinel (light grey) from 13R-9/199.60A using reflected light.

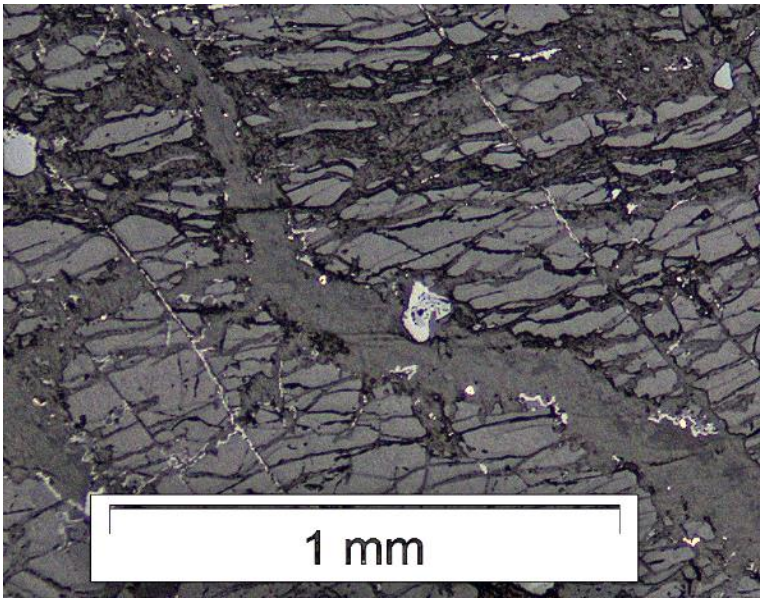

Figure 3.9: Sulphides (yellow) seen along silicate veins from 13R-9/199.60A using reflected light.

3.3.2 LG-6A

Predominantly composed of massive chromitite with interstitial orthopyroxene and clinopyroxene (Table 3.2). Cr-spinel has been texturally coarsened with a crystal size range from 0.05 – 1.20 mm. There are typically less than 1% sulphides, which commonly occur within grain triple junctions or along the crystal boundaries of Cr-spinel crystals. The sulphides also occur as inclusions within the Cr-spinel (Figure 3.4). The Cr-spinel displays some alteration to ilmenite/magnetite along the rims (Figure 3.3). Towards the bottom contact of the reef there is an increase in silicates particularly orthopyroxene (13R-9/199.82G, H and J), these silicate-rich portions contain greater abundances of sulphides (Figure 3.17Figure 3.18).

3.3.3 Middling

Predominantly composed of orthopyroxenite, however there are gradual changes from the base of the LG-6A contact to the top of the LG-6 (Table 3.2). It starts at the top as a chromitiferous orthopyroxenite which rapidly changes to an extensive (>10 m) central portion of orthopyroxenite with interstitial clinopyroxene, plagioclase, Cr-spinel, biotite and amphibole (Figure 3.10 and Figure 3.11). Cr-spinel then becomes the major mineral phase with olivine and serpentine alteration

appearing at the expense of orthopyroxene. Here the Cr-spinel is either massive or chain textured. At the base of the middling; orthopyroxene abundances increase whereas Cr-spinel decreases, olivine and serpentine alteration remain elevated (Table 3.2). The orthopyroxene crystals range in size from 0.1 to 2.5 mm and can be euhedral in the central section to anhedral nearer the top of LG-6 where there is significantly more alteration. All orthopyroxene crystals contain exsolution lamellae of clinopyroxene and may contain inclusions of olivine (Figure 3.12). The Cr-spinel crystals are disseminated and range in size from 0.05 to 0.4 mm. In some place where textural coarsening and annealing occurs to form chain textures another oxide mineral phase can be seen between the annealing Cr-spinel crystals (Figure 3.13). The olivine crystals range in size from 0.5 to 2.5 mm, they are usually highly fractured and heavily altered and typical sizes are at the smaller end of the size range. The serpentine alteration from olivine is also commonly associated with magnetite veins (Figure 3.10).

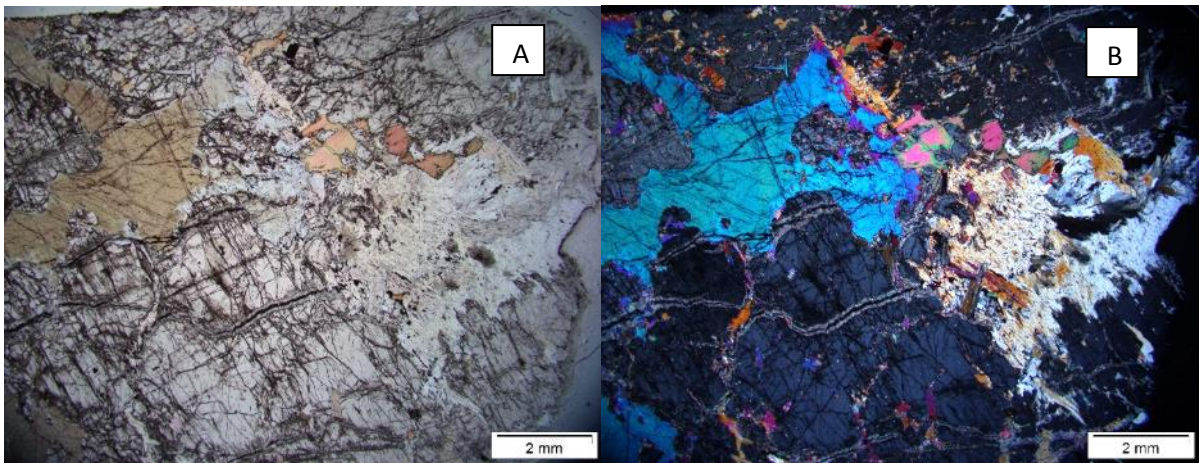

Figure 3.10: Typical Orthopyroxenite seen in the Middling 2 (sample: 13R-9/200.15B). A- PPL, Orthopyroxene (light grey), clinopyroxene (light brown), biotite (light pinkish brown to green) and serpentine (clear surrounding the thin black/opaque veins). With a single Cr-spinel crystal near the top in the middle (black/opaque). B- XPL, Orthopyroxene (grey), clinopyroxene (high birefringence, blue), biotite (high birefringence, bright pink to lime green) and serpentine (white rims along the black/opaque magnetite veins).

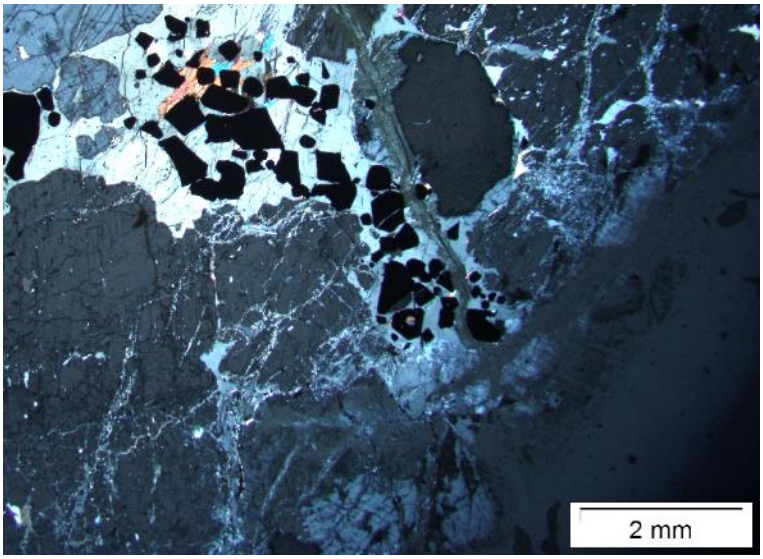

Figure 3.11: XPL of sample 13R-9/200.15E, Cr-spinel (black) and clinopyroxene (pale green to white) hosted interstitial to orthopyroxene (grey).

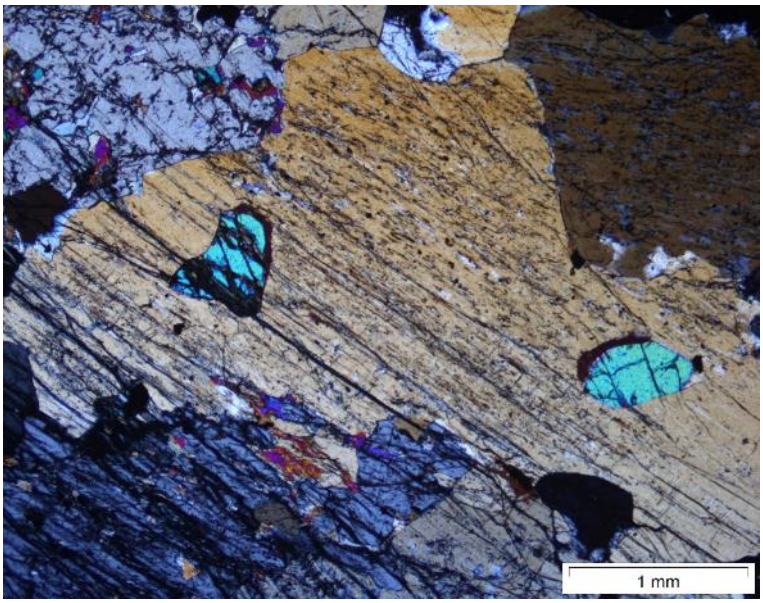

Figure 3.12: XPL of sample 13R-9/212.10A, Orthopyroxene (large, brown with NW-SE cleavage) crystal with inclusions of olivine (high birefringence, greenish blue, fractured).

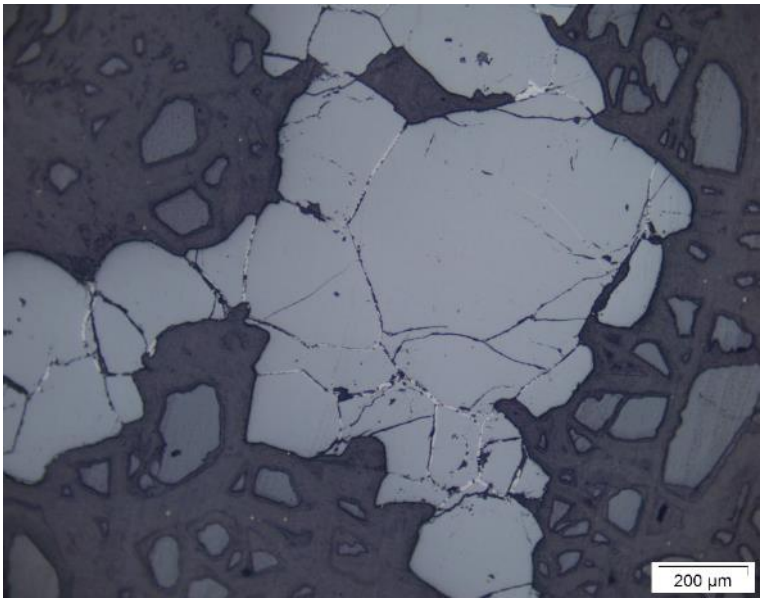

Figure 3.13: Reflected light image of sample 13R-9/212.68A. A second oxide mineral phase can be seen between the annealing Cr-spinel crystals.

When massive Cr-spinel occurs again in the lower part of the middling towards the top of the LG-6 contact both orthopyroxene and olivine are present (13R-9/212.68A – 13R-9/212.90D).

3.3.4 LG-6 chromitite

Predominantly composed of chromitite with minor interstitial orthopyroxene and less than 0.5% sulphides (Table 3.2). The Cr-spinel has been texturally coarsened with a crystal size range 0.05 to 0.8 mm (Figure 3.14). The orthopyroxene is primarily interstitial, however there are large silicate rich areas which occur near the top of the reef associated with serpentine alteration (e.g. Samples 13R-9/212.90G&H) (Figure 3.15). Also orthopyroxene veining occurs within the chromitite layer which is characteristically sulphide poor in contrast to orthopyroxene that occurs interstitially to the Cr-spinel (Figure 3.16). The orthopyroxene veining appears to run semi-parallel to the chromitite reef. Sample 212.90E has two severely altered oikocryst remnants that have higher abundances of sulphides (Figure 3.17 and Figure 3.18).

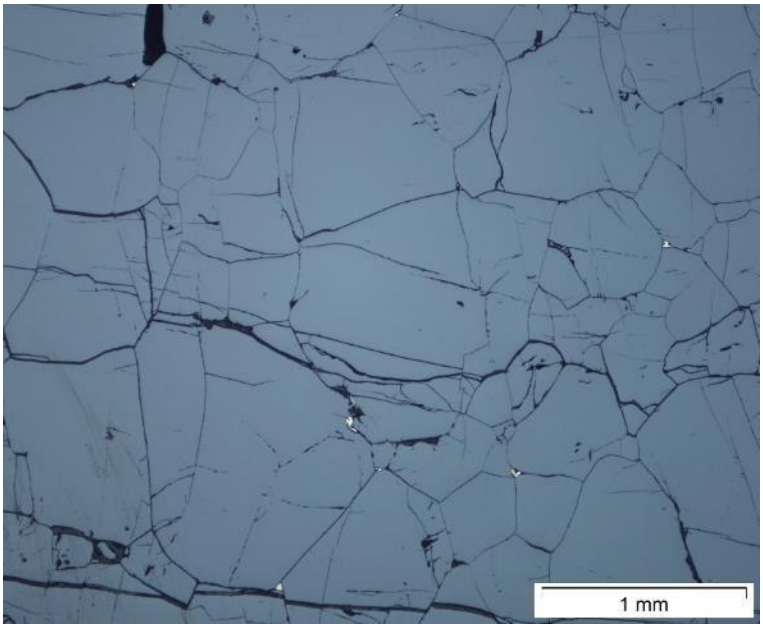

Figure 3.14: Texturally coarsened LG-6 massive chromitite with interstitial sulphides (tiny yellow specks), reflected light image of sample 13R-9/212.90E.

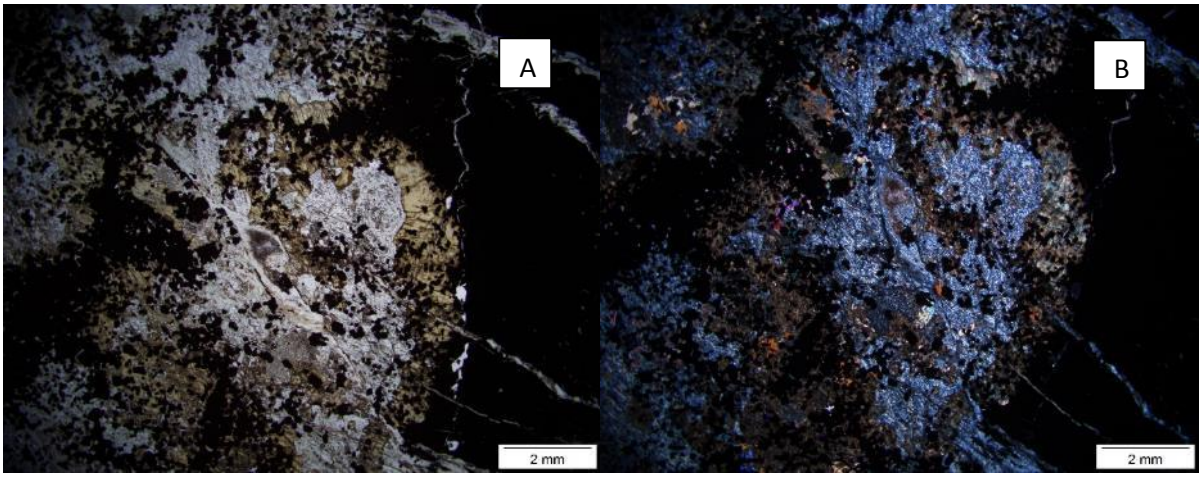

Figure 3.15: Image of sample 13R-9/212.90H. A- PPL, Silicate rich (brown and green) material in massive chromitite (black/opaque). B- XPL, Orthopyroxene (brown) surrounding alteration (serpentine?) both hosted in massive chromitite.

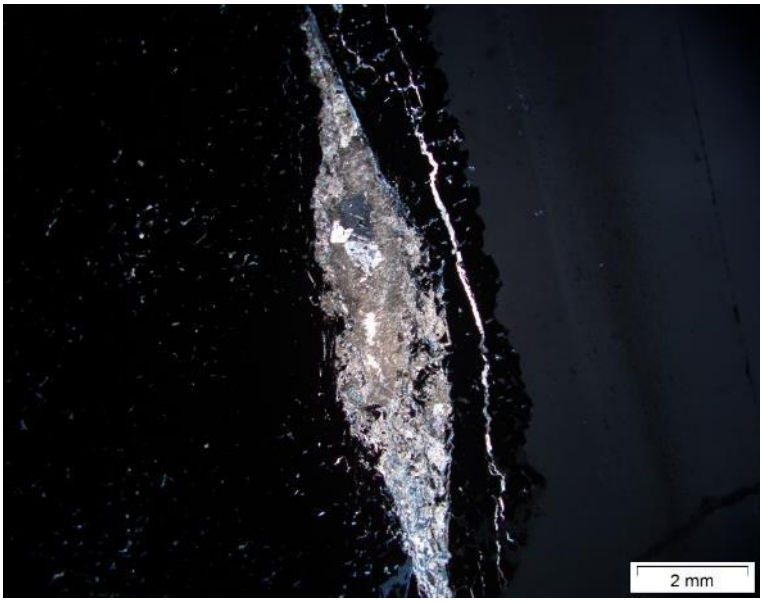

Figure 3.16: XPL image of sample 212.90L, Sulphide deficient late stage orthopyroxene (brown) in massive chromitite (black).

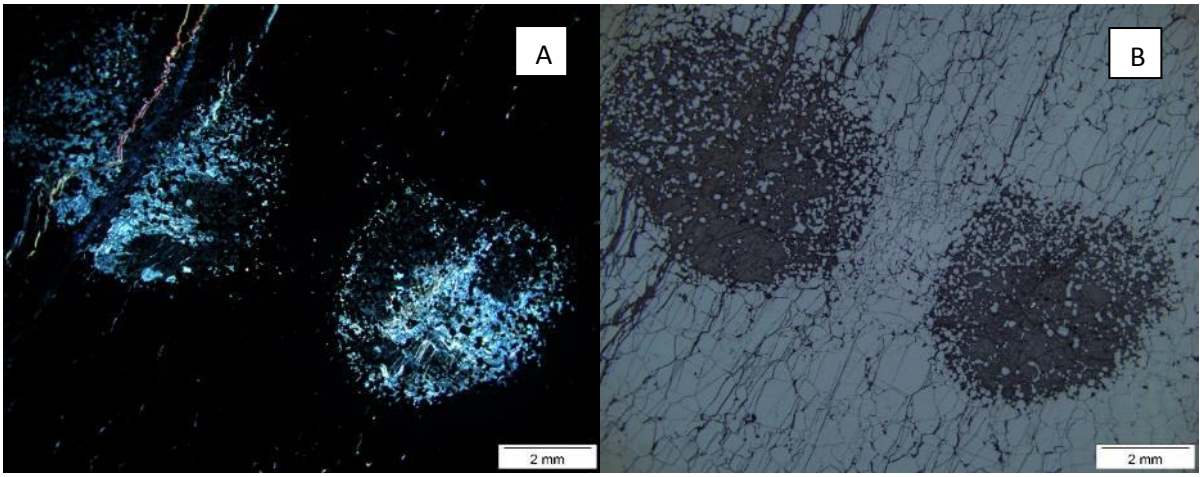

Figure 3.17: Image of sample 13R-9/212.90E. A- XPL, 2 remnant oikocrysts of silicate minerals which are heavily altered. B- Reflected light showing silicate remnants hosting Cr-spinel.

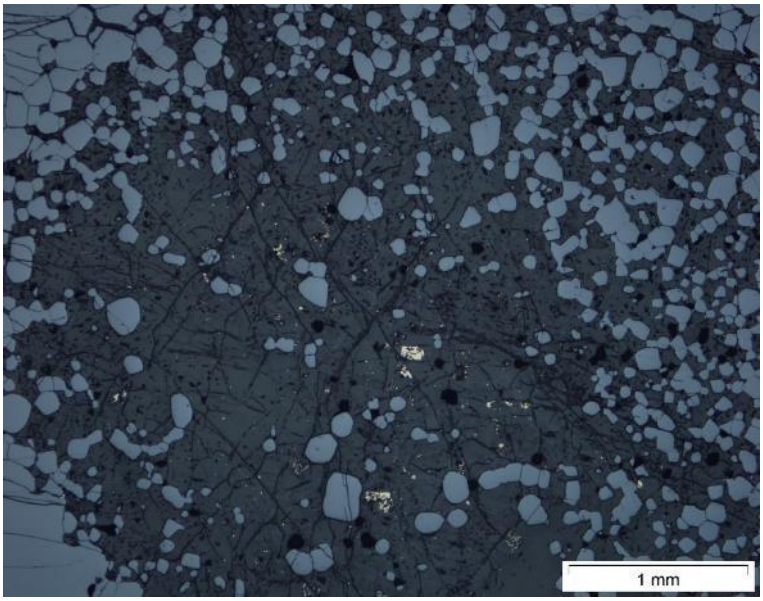

Figure 3.18: Reflected light, higher magnification image of Figure 3.17B showing that the silicate remnants preferentially concentrate sulphides.

3.3.5 Footwall

The footwall can be divided into two parts, the first part is the ~40 cm directly below the LG-6 chromitite which is composed of orthopyroxene, olivine and serpentine alteration with disseminated and chain textured Cr-spinel (Figure 3.19) (Table 3.2). The chain textured Cr-spinel occurs when there is more than 5% Cr-spinel. The second part is predominantly composed of orthopyroxene with interstitial clinopyroxene and disseminated Cr-spinel (Figure 3.20). The orthopyroxene crystals are euhedral to subhedral and display exsolution lamellae of clinopyroxene, however it is significantly less than that seen in the orthopyroxenes in the middling. Orthopyroxene crystals range in size from 0.3 to 2.0 mm with the average crystal size being greater where there is no olivine nor associated serpentine alteration.

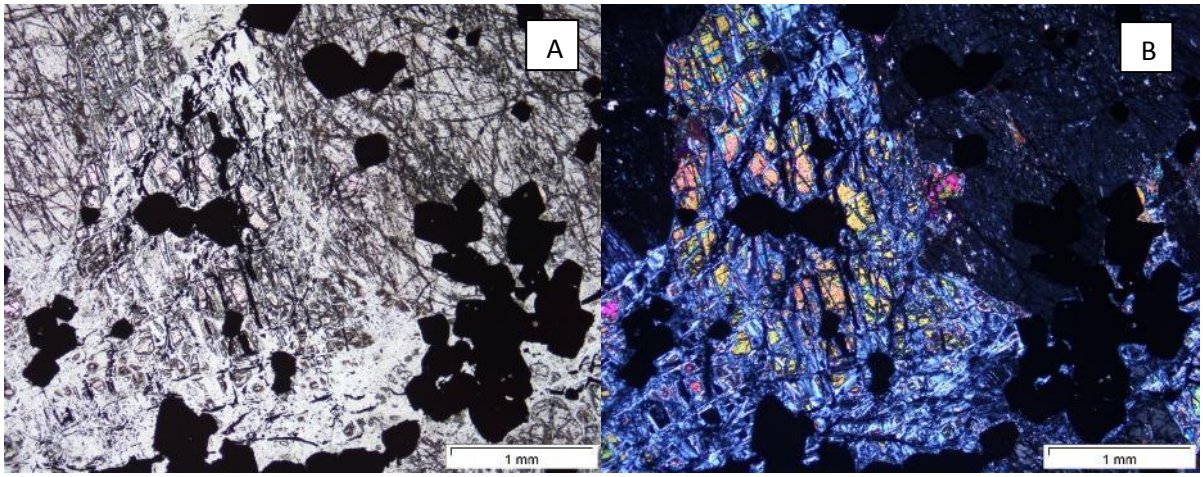

Figure 3.19: Representative image of the top 40 cm of the FW from sample 13R-9/213.63D. Containing Orthopyroxene (top right corner), olivine (high birefringence, multi-coloured), serpentine and disseminated Cr-spinel (black). (A-PPL, B-XPL)

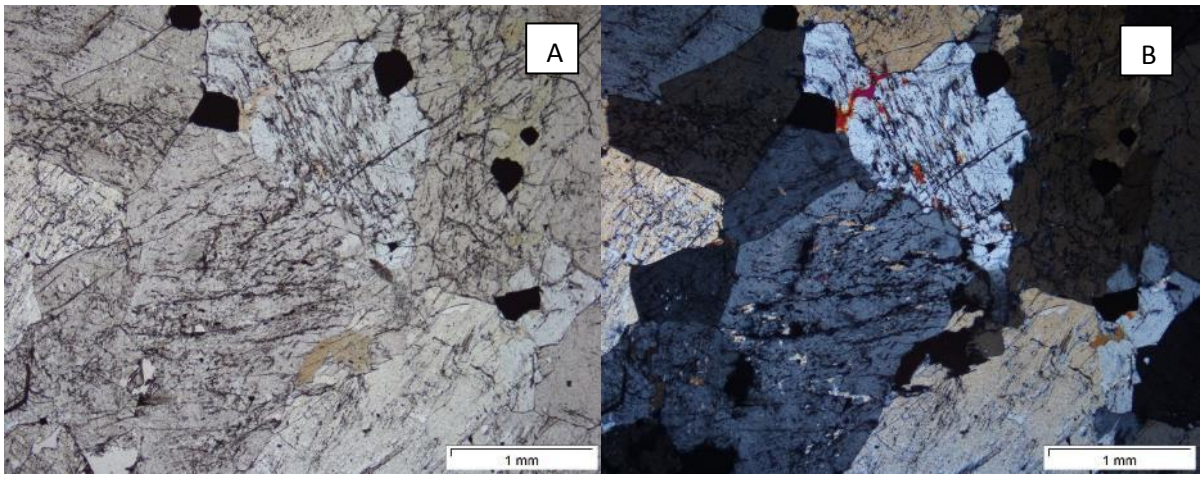

Figure 3.20: Images from sample 13R-9/214.60 – 214.80). A-PPL, Typical FW composed of predominantly orthopyroxene with interstitial clinopyroxene and disseminated Cr-spinel (black). B-XPL, Orthopyroxene (grey & light brown) with interstitial clinopyroxene (high birefringence, red and orange) and disseminated Cr-spinel (black).

Table 3.2: Borehole 13R-9

Unit	Depth	Thickness	Lithology	Modal abundance
HW 1	199.22 m to 199.60 m	0.38 m	Serpentinised harzburgite	18% Olivine 15% orthopyroxene 62% Serpentine 5% Magnetite
HW 2	199.60 m to 199.71 m	0.11 m	Olivine-bearing Orthopyroxenite with disseminated Cr-spinel	11% Olivine 69% Orthopyroxene 6% Serpentine 11% Cr-spinel 3% Clinopyroxene
LG-6A	199.72 m to 200.16 m	0.44 m	Chromitite	11% Orthopyroxene 87% Cr-spinel 1% Clinopyroxene
Middling 1	200.16 m to 200.19 m	0.03 m	Orthopyroxenite with disseminated Cr-spinel	93% Orthopyroxene 5% Cr-spinel 1% Other
Middling 2	200.19 m to 212.13 m	1.94 m	Orthopyroxenite	87% Orthopyroxene 2% Cr-spinel 1% Plagioclase 3/4% Clinopyroxene 2% Biotite 2% Amphibole 1% Olivine 1% Serpentine
Middling 3	212.68 m to 212.84 m	0.16 m	Orthopyroxenite	8% Orthopyroxene 23% Cr-spinel 1% Clinopyroxene 17% Olivine 50% Serpentine
Middling 4	212.84 m to 213.02 m	0.18 m	Harzburgite with disseminated Cr-spinel	47% Orthopyroxene 15% Cr-spinel 1% Plagioclase

				2% Clinopyroxene 16% Olivine 18% Serpentine
LG-6	213.02 m to 213.73 m	0.71 m	Chromitite	10% Orthopyroxene 89% Cr-spinel 1% Other
FW 1	213.73 m to 214.24 m	0.51 m	Harzburgite with disseminated Cr-spinel	37% Orthopyroxene 8% Cr-spinel 2% Clinopyroxene 11% Olivine 41% Serpentine
FW 2	214.24 m to 215.79 m	1.55 m	Orthopyroxenite	90% Orthopyroxene 4% Cr-spinel 5% Clinopyroxene

3.4 Summary

Regionally the LG-6 and LG-6A are hosted in orthopyroxenite (Teigler, 1990). However locally at Ruighoek mine in the north eastern corner of the property there are a few anomalous boreholes namely 13R-5, 13R-8 and 13R-9. The mine found that in this area there are olivine bearing harzburgites in close proximity to the LG-6 reef. Borehole 13R-9 was selected to be looked at in greater detail.

The main difference between boreholes 13R-3 and 13R-9 is the presence of olivine in 13R-9. For the most part the harzburgites are altered to magnetite with serpentine and there is very little remnant of the original olivine crystals. The orthopyroxenite host has interstitial clinopyroxene which occurs as oikocrysts as well as clinopyroxene exsolution lamellae. The chromitite reefs have been significantly texturally coarsened and contain very little sulphides typically less than 1 %. The sulphides that are there tend to occur at the triple junction and along the edges of Cr-spinel crystals and occasionally as inclusions within the Cr-spinel. Within the LG-6 reef for 13R-9 there are silicate remnants that preferentially concentrate sulphides (Figure 3.18) as well as 1% of other interstitial material that could not be identified, which is most likely either orthopyroxene or olivine remnants.

4. Geochemistry

4.1 Introduction

Whole rock data will identify large scale trends in geochemical evolution and help identify magmatic processes such as recharge events, giving insight into the formation of the LG-6 chromitite (Appendix A and B). The mean value and standard deviation calculations for the whole rock data is in Appendix C. Mineral chemistry will be used to identify differences between the two boreholes as well as differences between the hanging wall and footwall lithologies of elevated Cr/Fe ratio borehole 13R-9 (Appendix E to G).

Error analysis completed on the whole rock and EPMA data can be seen in Appendix D to G includes the calculation of two sigma (2σ) variations and analytical recovery (AR) for the whole rock data and calculation of the atoms per formula unit (APFU) for the mineral chemical data.

Nomenclature: The abbreviation PGE's refers to the platinum group elements, namely Pt, Pd, Rh, Ir, Os and Ru; these are further split into the Pt-group (PPGE's, Pt, Pd and Rh) and the Ir-group (IPGE's, Ir, Os and Ru). Calculated ratios are: Pt*/Ru* ([Pt+Pd+Rh]/ [Ir+Os+Ru]), Cr# (Cr/ [Cr+Al]*100), Mg# (Mg/ [Mg+Fe^{2+}]*100) and Cr/Fe (Cr/Fe^{2+}). The whole rock iron contents were corrected for Fe^{3+} and Fe^{2+}using a Fe^{3+}:Fe^{2+} ratio of 0.10: 0.9. This ratio was used because several authors (e.g. Eales et al. 1993; Naldrett et al, 2008; Teigler et al, 1992 and Wilson, 2012) use this ratio, which makes comparison between data from this study and published data easier. Based on titrations Wilson (2012) determined that the distribution of Fe^{3+} to $Fe_{(tot)}$ for the liquid is 0.15 and for orthopyroxene is 0.1.

4.2 Borehole whole rock data

Depth profiles for major elements from boreholes 13R-3 and 13R-9 are plotted below in Figure 4.1Figure 4.2Figure 4.3. The 2 boreholes both show abrupt changes in Al_2O_3, Cr_2O_3, $FeO_{(T)}$, MgO, SiO_2, TiO_2 and V at the base and top of the leader LG-6A chromitite (Figure 4.1Figure 4.2). Borehole 13R-3 has abrupt changes at the base and top of the LG-6 chromitite, whereas 13R-9 has a more gradational transition at the top of the LG-6 chromitite. The abrupt chemical changes usually correspond to changes in the bulk mineralogy. It should also be noted that the harzburgite bearing borehole, 13R-9

has a greater maximum MgO content of 38.8 wt. % and a mean of 21.4 wt. % (13R-3 maximum MgO content is 29.1 wt. % and a mean of 18.4 wt. %) (Figure 4.1). The TiO_2 content in 13R-3 ranges from 0.09 to 0.63 wt. % whereas in 13R-9 it ranges from 0.08 to 1.06 wt. %. Although in Figure 4.1, 13R-9 has a higher MgO content, it does not display a higher maximum Mg# value (Figure 4.3), 82.76 for 13R-9 compared to 82.817 for 13R-3. This is because it also has proportionally higher FeO. Both boreholes have a similar minimum Mg# of 40.53 for 13R-3 and 39.53 for 13R-9 (Figure 4.3). The LOI (loss on ignition) for each borehole is variable, for 13R-3 there is negligible LOI. However, 13R-9 has up to 10.86 wt. % LOI, the LOI spikes correspond with harzburgitic lithologies. The Ni content of the reef for 13R-9 (mean 579.7 ppm Ni) is depleted compared to 13R-3 (mean 886.2 ppm Ni), whereas the Total PGE content for the main reefs (means, 1077.7 ppb for 13R-3 and 1210.15 ppb for 13R-9) are comparable, whereas the LG-6A for 13R-9 (mean, 2365.6 ppb) is significantly enriched compared to 13R-3 (mean, 1629.7 ppb) although this could be analytical error as seen in the standard deviation for the Total PGE in LG-6A for 13R-9. Figure 4.4 displays the Cr/Fe ratio for each borehole next to its' cumulative calculated CIPWD normative values. 13R-9 does have a higher Cr/Fe ratio (max 2.11) for the lower chromitite reef (LG-6) compared to 13R-3 (max 1.63). For Figures 5.1, 5.2, 5.3 and 5.4 the data axes for similar elements on the different graphs are the same to make enrichment/depletion comparisons more visible.

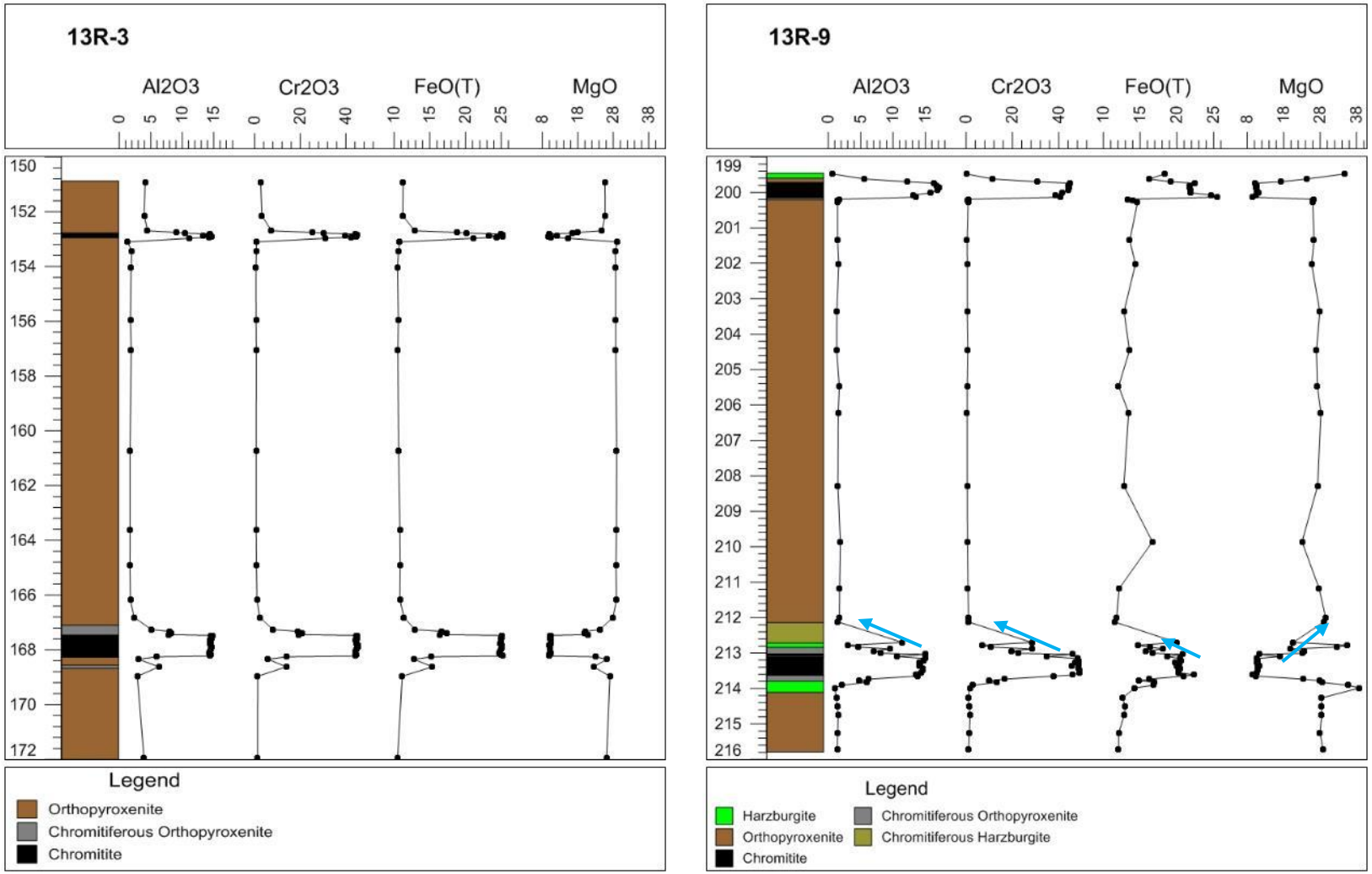

Figure 4.1: Whole rock chemistry comparing (a) 13R-3 and (b) 13R-9 and variations in Al_2O_3, Cr_2O_3, $FeO_{(T)}$ and MgO between the reef and host silicates. The blue arrows on 13R-9 highlighting the gradational change in chemistry in contrast to 13R-3, which changes abruptly.

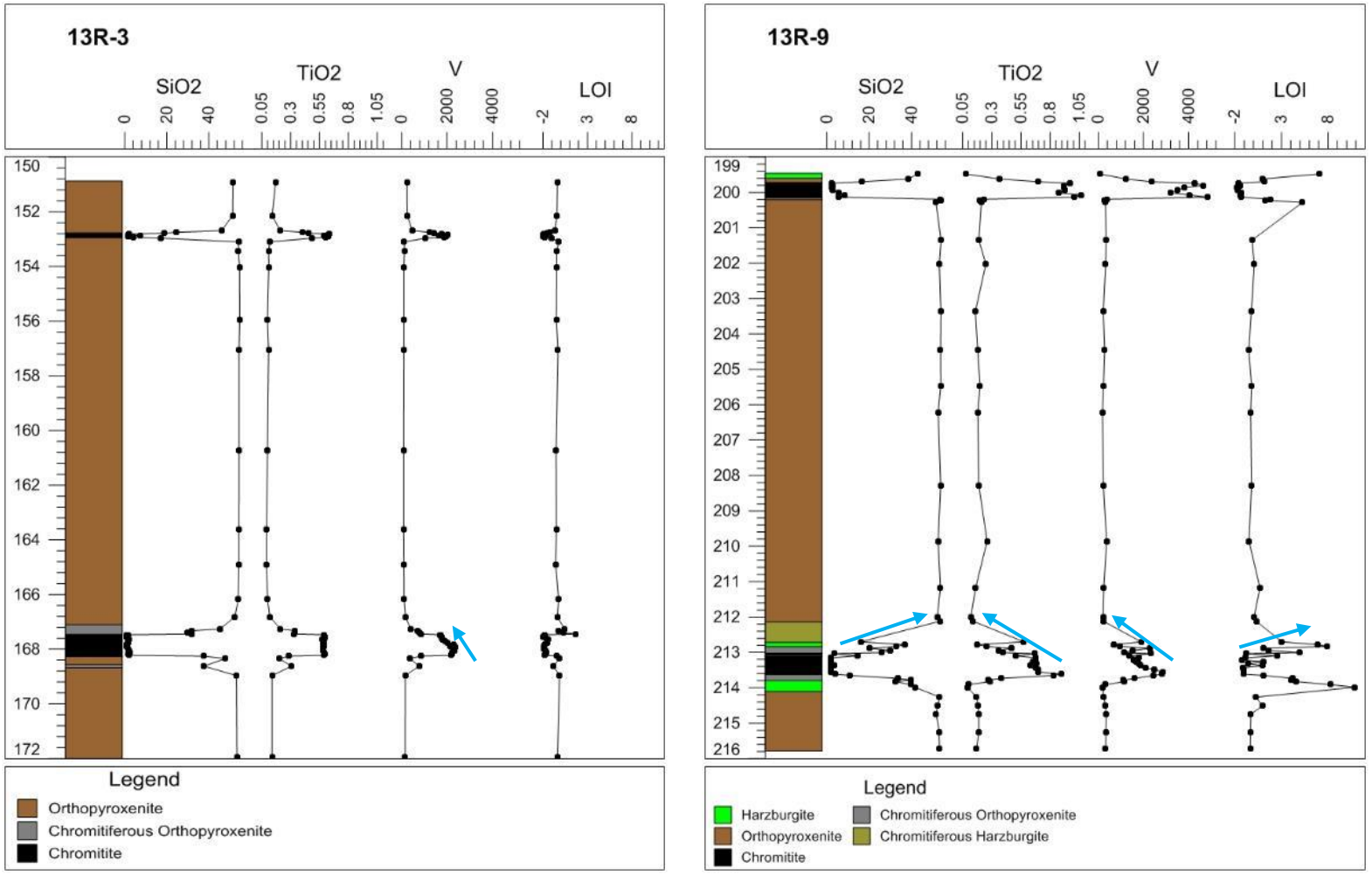

Figure 4.2: Whole rock chemistry comparing (a) 13R-3 and (b) 13R-9 and variations in SiO_2, TiO_2, V and the loss on ignition (LOI) between the reef and the host silicates. The blue arrows on 13R-9 highlighting the gradational change in chemistry in contrast to 13R-3 which changes abruptly.

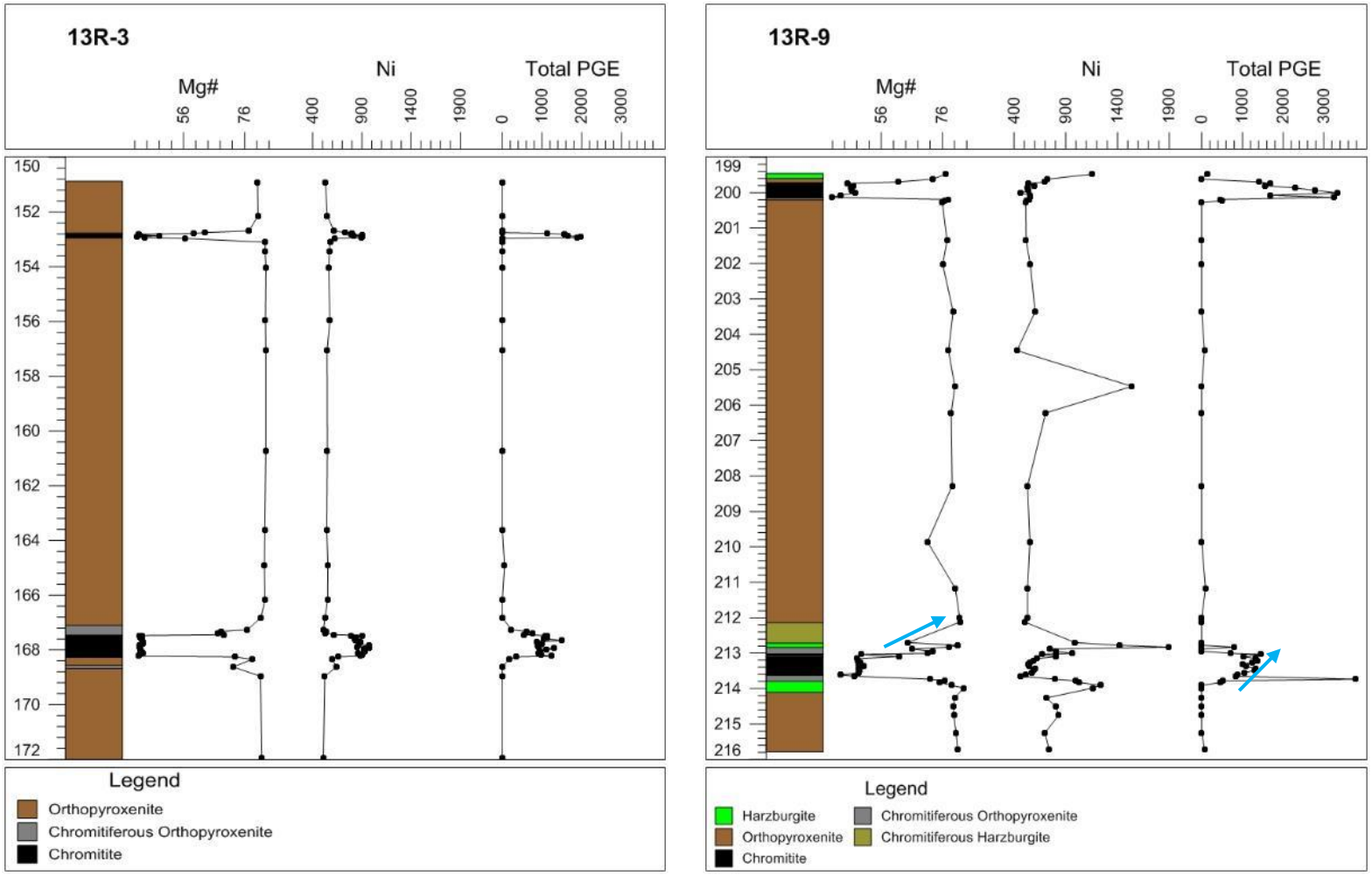

Figure 4.3: Whole rock chemistry comparing (a) 13R-3 and (b) 13R-9 and variations in the Mg# [Mg/ ($Mg+Fe^{2+}$)]*100, Ni as well as total PGE content between the reef and the host silicates. The blue arrows on 13R-9 highlighting the gradational contact.

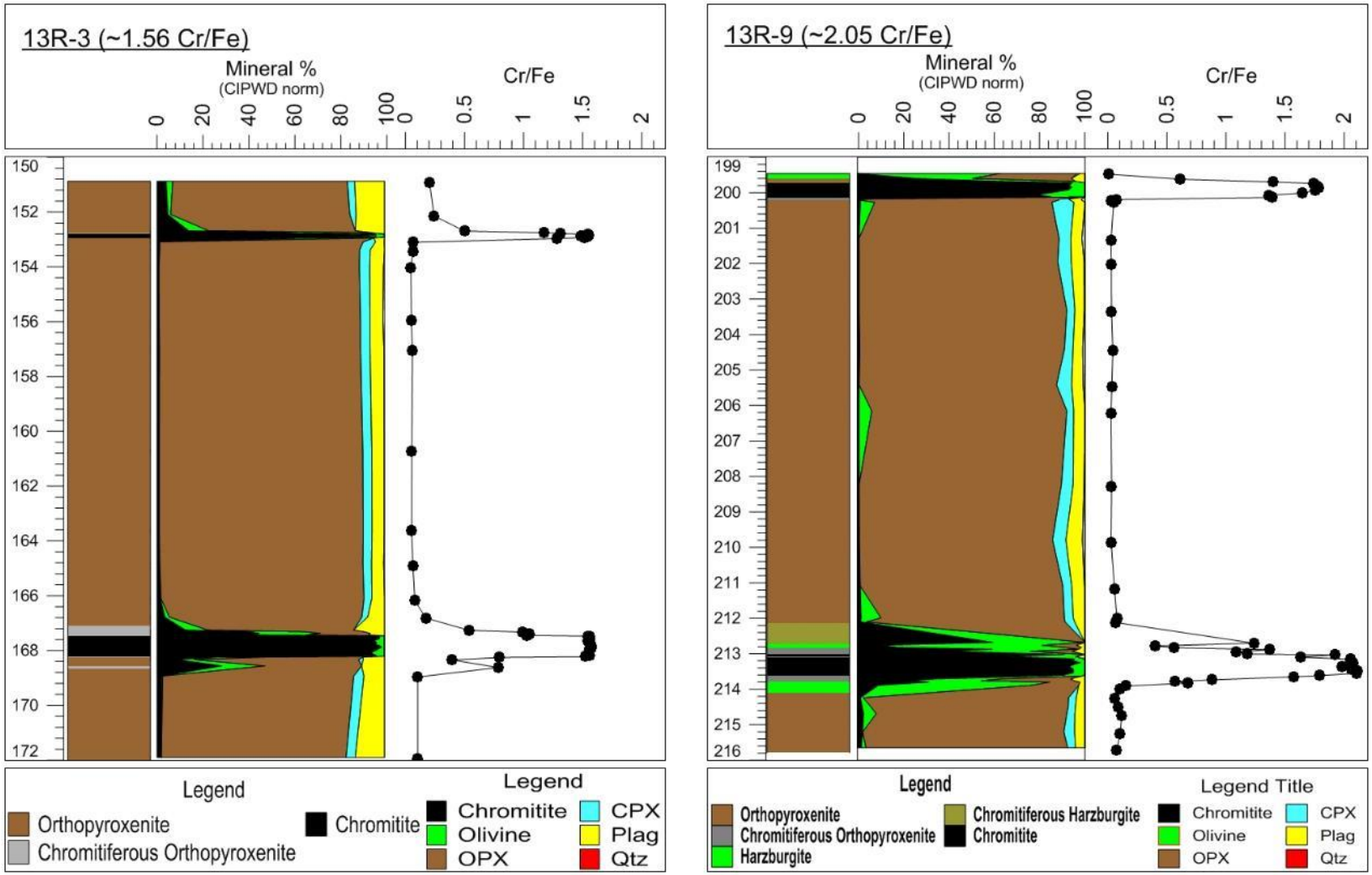

Figure 4.4: (a) 13R-3 and (b) 13R-9 indicating variations in the CIPWD calculated cumulative mineral percentages in comparison with the Cr/Fe ratio.

4.3 Chromitite reef whole rock major and minor data for LG-6

The depth profiles in the figures below (Figure 4.5 -Figure 4.9) are of the same major elements as the profiles above with the exception of LOI which is not described due to consistency throughout the reef. These profiles are not for the entire sampled length of the boreholes but only of the main LG-6 chromitite. The focus is shifted to the LG-6 chromitite to identify any smaller scale geochemical variations. The profiles below (Figure 4.5 -Figure 4.9) are solely comprised of one major mineral (Cr-spinel).

4.3.1 Borehole 13R-3

There are at least 2 trends seen in Figure 4.5, the one above the red line and one below. With both trends there is an upwards increase in Al_2O_3 (14.40 to 14.72 wt. %), Cr_2O_3 (44.1 to 45.3 wt. %) and $FeO_{(T)}$ (25.01 to 25.43 wt. %) and a corresponding upwards decrease in MgO (10.34 to 10.04 wt. %). In Figure 4.6 there is a slight decrease in V and Ni upwards through the reef. The trends seen in Figure 5.5 are likely due to the change in the interstitial SiO2 content as seen in Figure 5.6, they are opposite for Al_2O_3, Cr_2O_3 and FeO

4.3.2 Borehole 13R-9

With borehole 13R-9 the second topmost sample (Figure 4.7; red line) has anomalously high values for MgO (16.8 wt. %) and SiO_2 (14.5 wt. %), however, having low values for Al_2O_3 (10.6 wt. %), Cr_2O_3 (34 wt. %) and to a lesser degree $FeO_{(T)}$ (18.6 wt. %) compared to the other reef samples. Petrographic analysis of this sample (13R-9/212.90G) highlighted the presence of orthopyroxene oikocrysts/inclusions within the chromitite, see section 3.3.4 (Figure 3.15), which is inferred to have resulted in the chemical variations, thus this sample was excluded from the discussion of the chromitite reef. Data points highlighted by green circles in Figure 4.8 and 5.9 form another outlier with depleted Cr_2O_3 (45 wt. %) and elevated SiO_2 (3.8 wt. %), however there were no petrographic anomalies. However this datum point resembles those that occur at the contacts of the reef and as such may just be a result of partial fractional crystallisation, which causes the slight increase in SiO_2 and decrease in Cr_2O_3 or a very thin orthopyroxene vein. Borehole 13R-9 displays Al_2O_3 (13.5 to 15 wt.

%), Ni (512 to 676 ppm) contents that increase upwards and $FeO_{(T)}$ (19.9 to 22.6 wt. %) and MgO (9.4 to 11.4 wt. %) contents that display a slight increase upwards. Cr_2O_3 (45.5 to 48.9wt. %) and TiO_2 (0.89 to 0.66 wt. %) contents decrease slightly upward (trends arrowed in Figure 4.8 & 4.9). V (2843 to 1547 ppm) contents also decreases upwards, however, this is reversed at the top of the reef where it increases (from 1547 to 2321 ppm) (Figure 4.9).

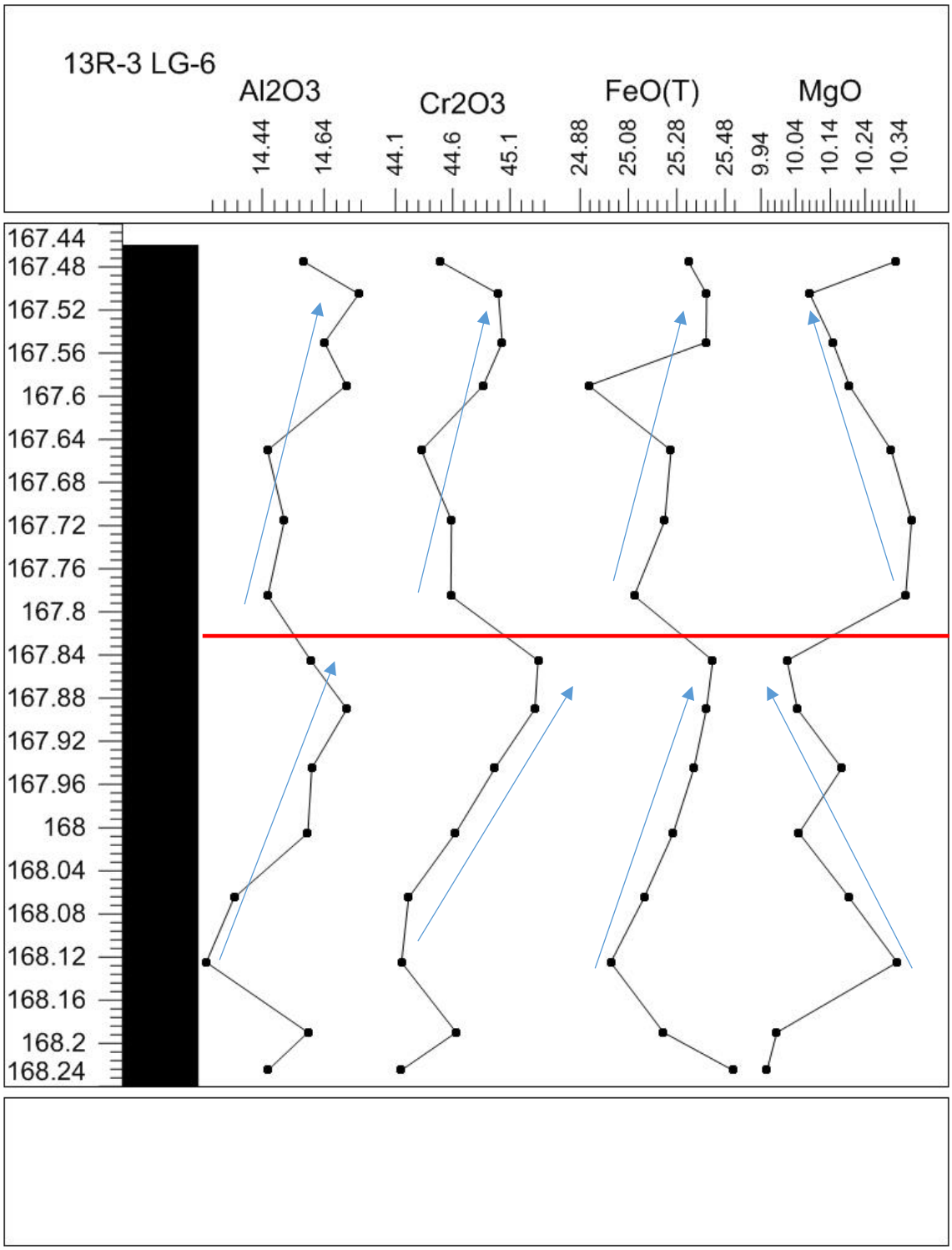

Figure 4.5: Major element (wt. % oxides) variation for the LG-6 reef intersection of BH 13R-3

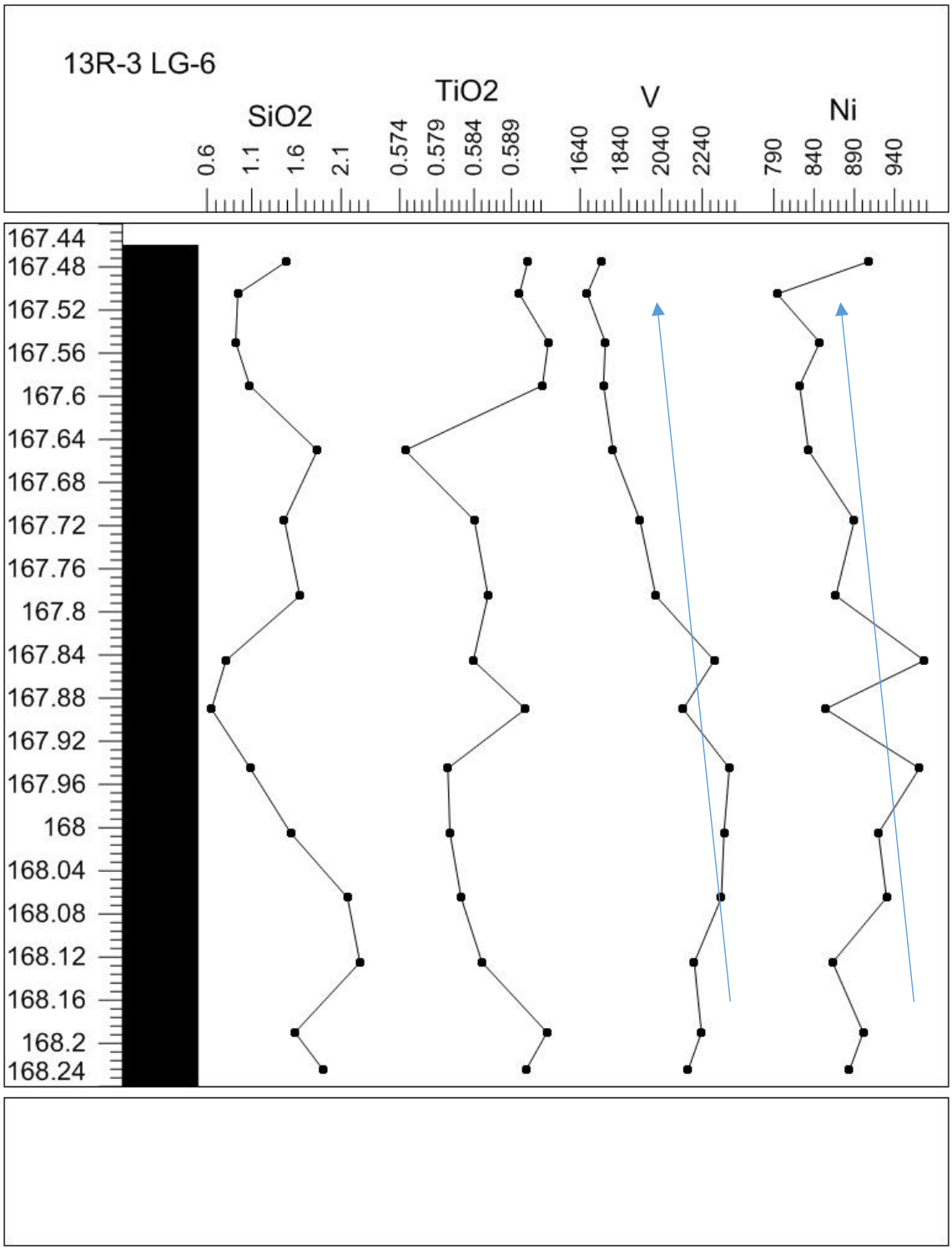

Figure 4.6: Major (wt. % oxides) and minor (ppm) element variation for the LG-6 reef intersection of BH 13R-3

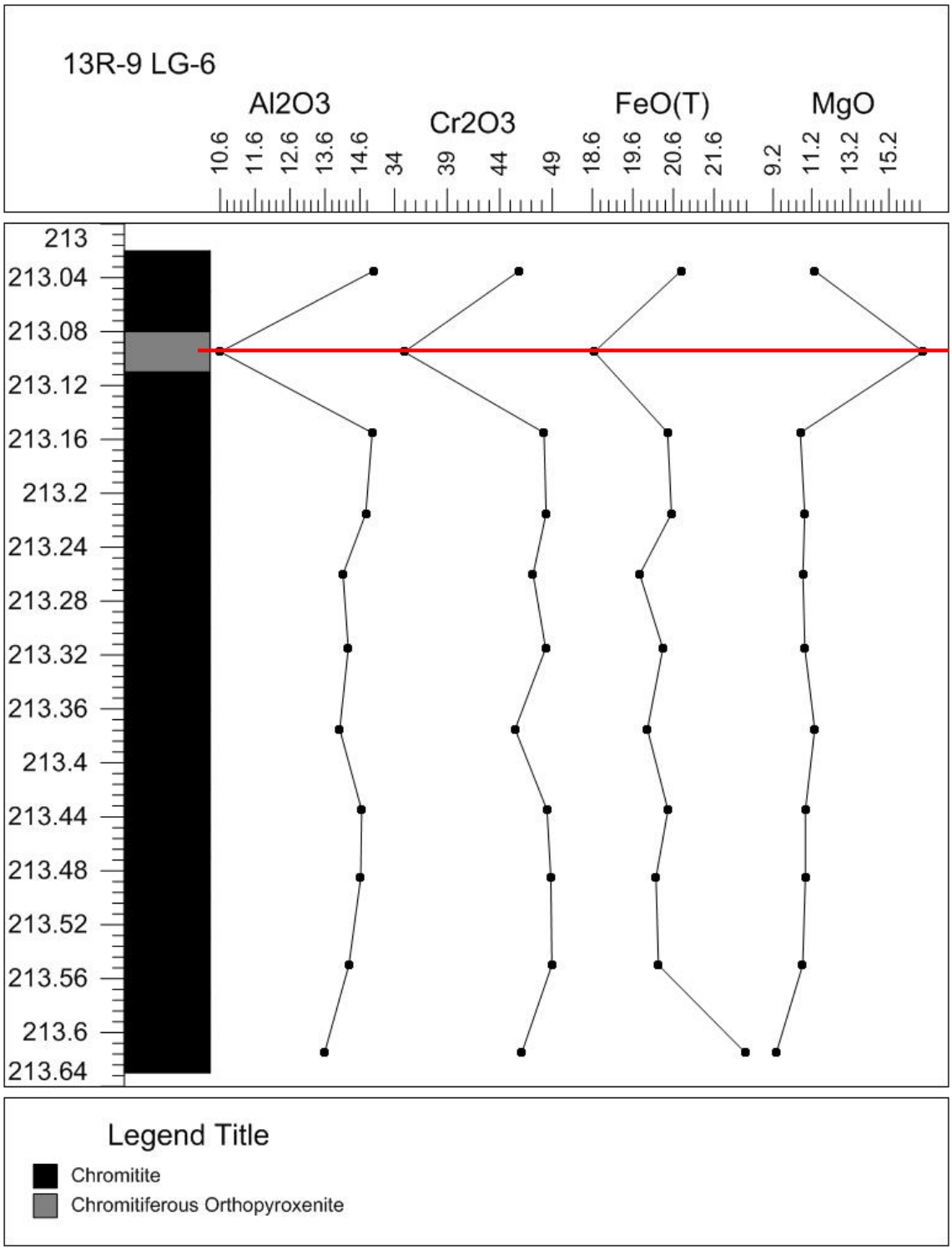

Figure 4.7: Major element (wt. % oxides) variation for the LG-6 reef intersection from 13R-9. Note the sample second from the top (red line) is anomalous and is hereafter omitted, due to the mineralogical variation (see section 3.3.4)

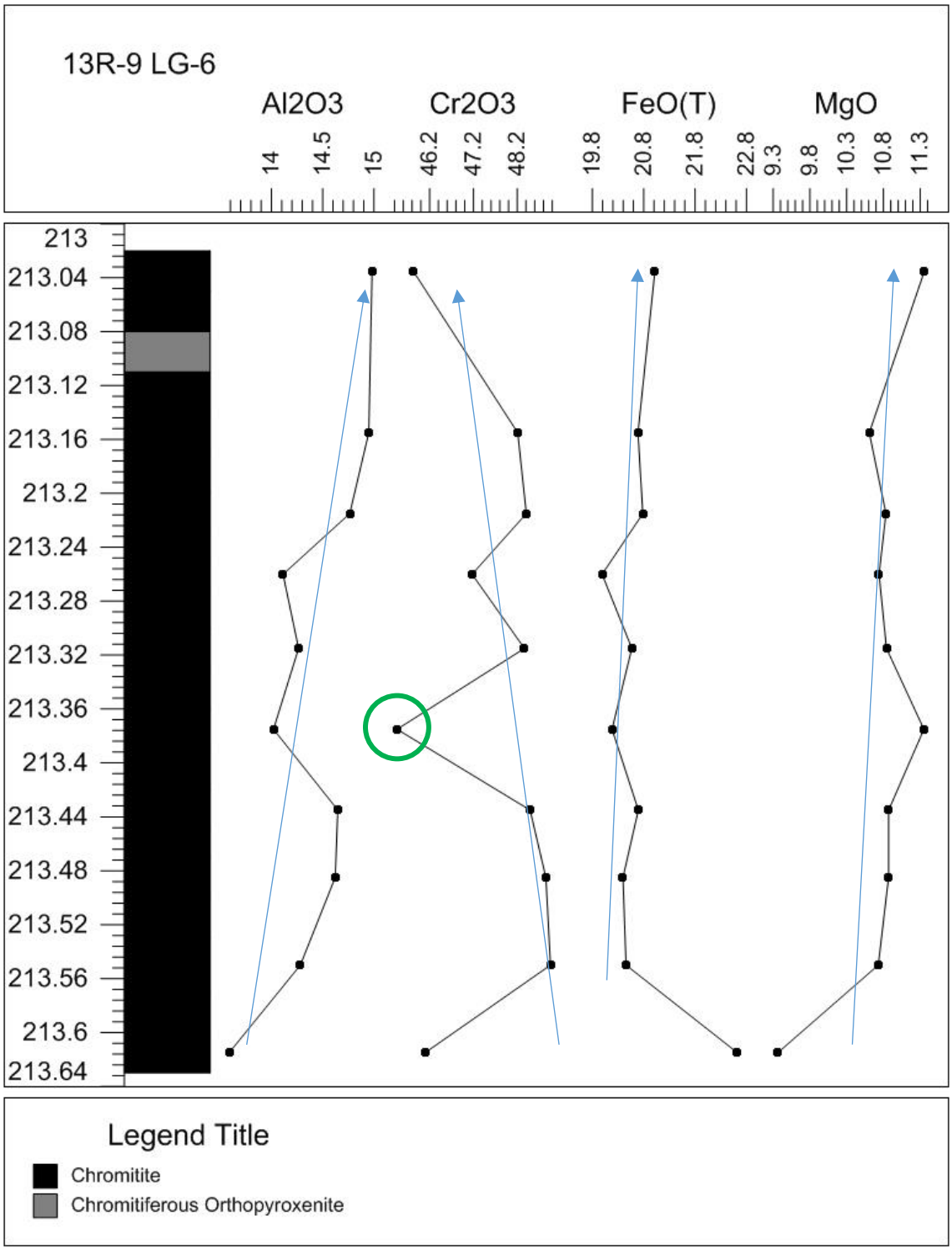

Figure 4.8: Major element (wt. % oxides) variation for the LG-6 reef intersection from 13R-9. The green circle represents a potential outlier.

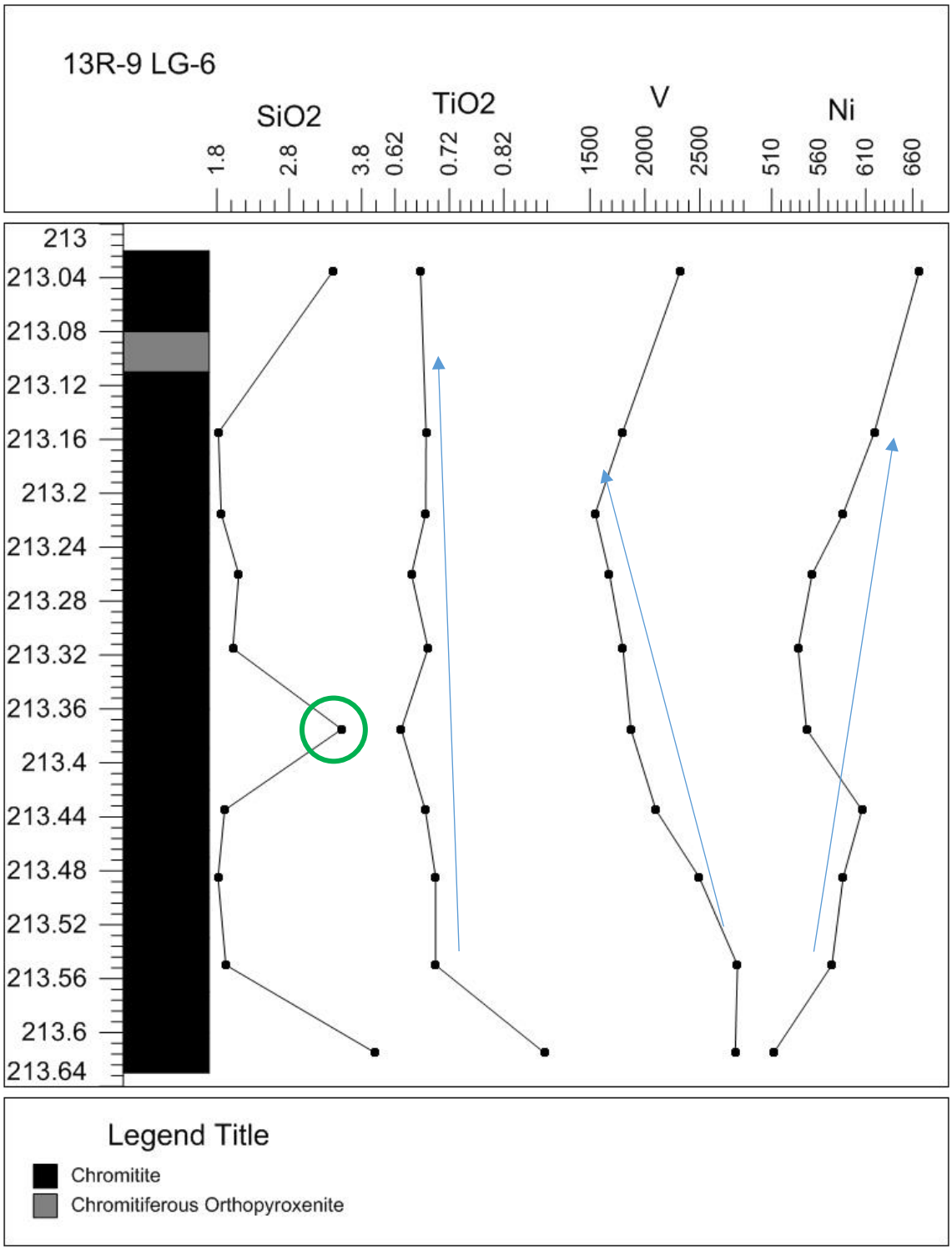

Figure 4.9: Major (wt. % oxides) and minor (ppm) element variation for the LG-6 reef intersection from 13R-9. The green circle represents a potential outlier

When comparing the means for the reef of 13R-3 and 13R-9, the Al_2O_3 (14.5 and 14.4 wt. % and a), SiO_2 (1.4 and 2.4 wt. %) and MgO (10.2 and 10.8 wt. %) contents are very similar. 13R-9, has a mean V content that is 66.6 ppm higher than the mean V of 13R-3, however the standard deviation for the difference of the two means is 153.7, therefore the difference in the means is insignificant. For 13R-9 the mean Ni content is 307.4 ppm lower, mean Cr_2O_3 content is 2.8 wt. % higher and the mean $FeO_{(Tot)}$ is 4.5 wt. % lower than the values for 13R-3. These differences between the means are real differences because the standard deviation for the different elements are Ni std dev is 18.3, Cr_2O_3 std dev is 0.4 and $FeO_{(tot)}$ std dev is 0.2 which is reasonable for each of the corresponding mean differences. This translates to 13R-9 having higher Mg# (mean 48.0 and 41.7), Cr# (mean 68.9 and 67.4) and Cr/Fe (mean 2.0 and 1.6) ratio values than 13R-3 (Figure 4.10 and 5.11). The mean 307.4 ppm less Ni for the LG-6 reef in 13R-9 compared to 13R-3 is because Ni has a higher partition coefficient for olivine (5.9 to 29) than for orthopyroxene (5) (Rollinson, using geochemical data).

There is a break In the Mg# of 13R-3 (Figure 4.10, red line), both sections decrease upwards. 13R-9 displays a very slight decrease in Mg# (Figure 4.11, red line) upwards through the reef as well as a break in both the Cr/Fe and Cr#.

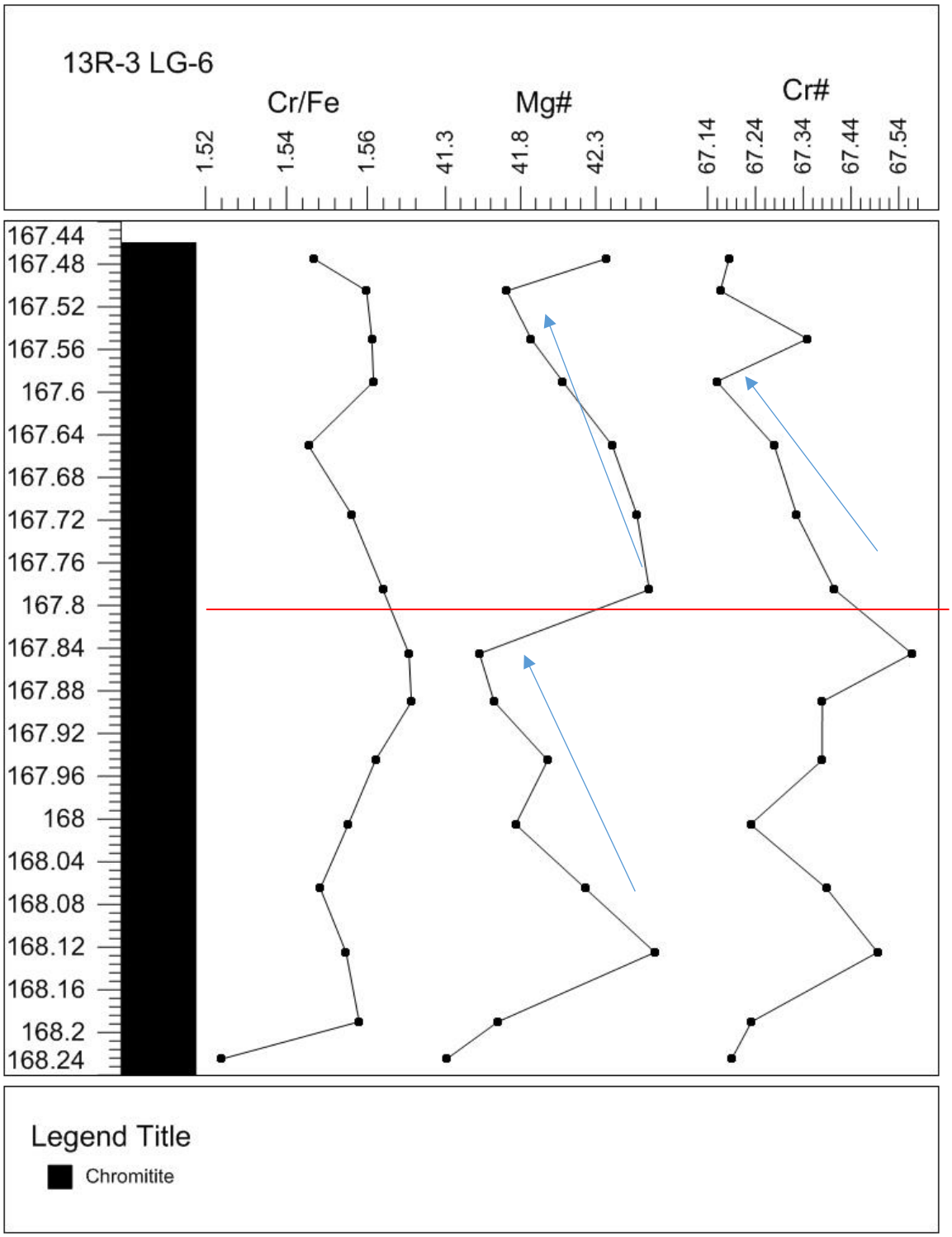

Figure 4.10: Cr/Fe, Mg# and Cr# of the LG-6 reef from 13R-3 (blue arrows highlighting trends and the red line indicating the break).

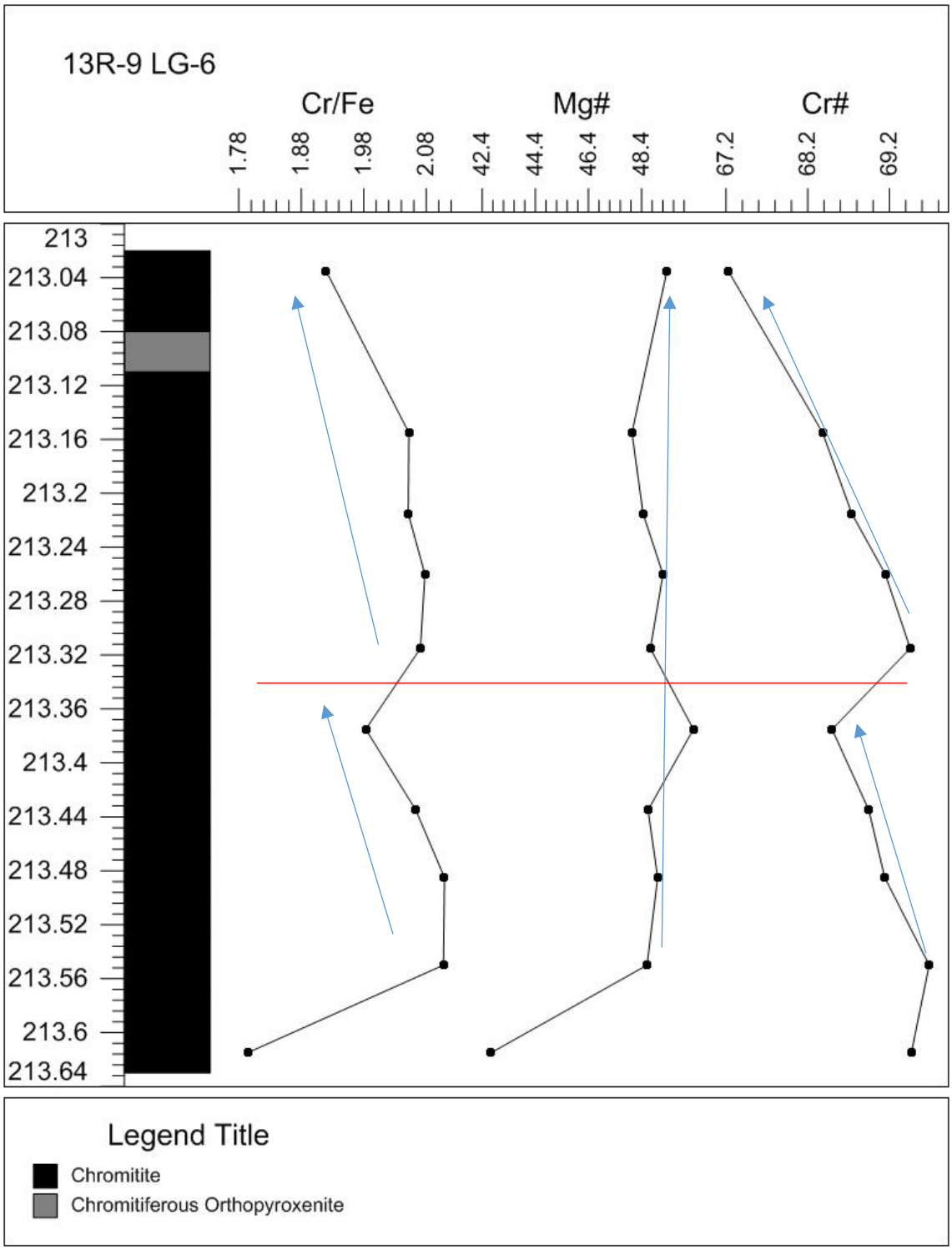

Figure 4.11: Cr/Fe, Mg# and Cr# of the LG-6 reef from 13R-9 (blue arrows highlighting trends and the red line indicating the break).

4.4 Trace element and PGE data for chromitite reef only

Most of the data collected for trace elements are below the limit of detection due to additional dilution required by the high concentration of Cr_2O_3.

Figure 4.12, 4.13 and 4.14 display the variation in S, Cu, PGEs and Pt*/Ru* ratio with depth. 13R-3 has negligible S in comparison to 13R-9; 13R-3 has a mean S content of 26.6 ppm whereas 13R-9 has a mean S content of 339.6 ppm. In Figure 4.12 for 13R-9 S displays a gradually upward increasing trend. 13R-3 has a mean Cu content of 13.4, and displays with no discernible trend. Whereas 13R-9 has 76.4 ppm mean Cu and displays an upward decreasing trend, it also has a small amount of S (up to 436.5 ppm) which increases upward. Both 13R-3 and 13R-9 have similar quantities of PPGEs (Pt, Pd and Rh), 463.1 ppb and 430.5 ppb means, however 13R-9 is slightly enriched in IPGE (Ir, Os and Ru) with 779.7 ppb mean compared to 614.6 ppb mean for 13R-3. The difference between the two IPGE mean values is 165.1 with the std dev of the mean difference being 46.2, indicating that the difference is real. The IPGE values (Figure 4.13) increase upward although more so for 13R-9. The PPGE values (Figure 4.14) differ slightly in that for 13R-3 there is very little variation between the top and the bottom of the reef. Whereas for 13R-9 the Pd value decreases slightly going upward in contrast the Pt and Rh values increase going upward.

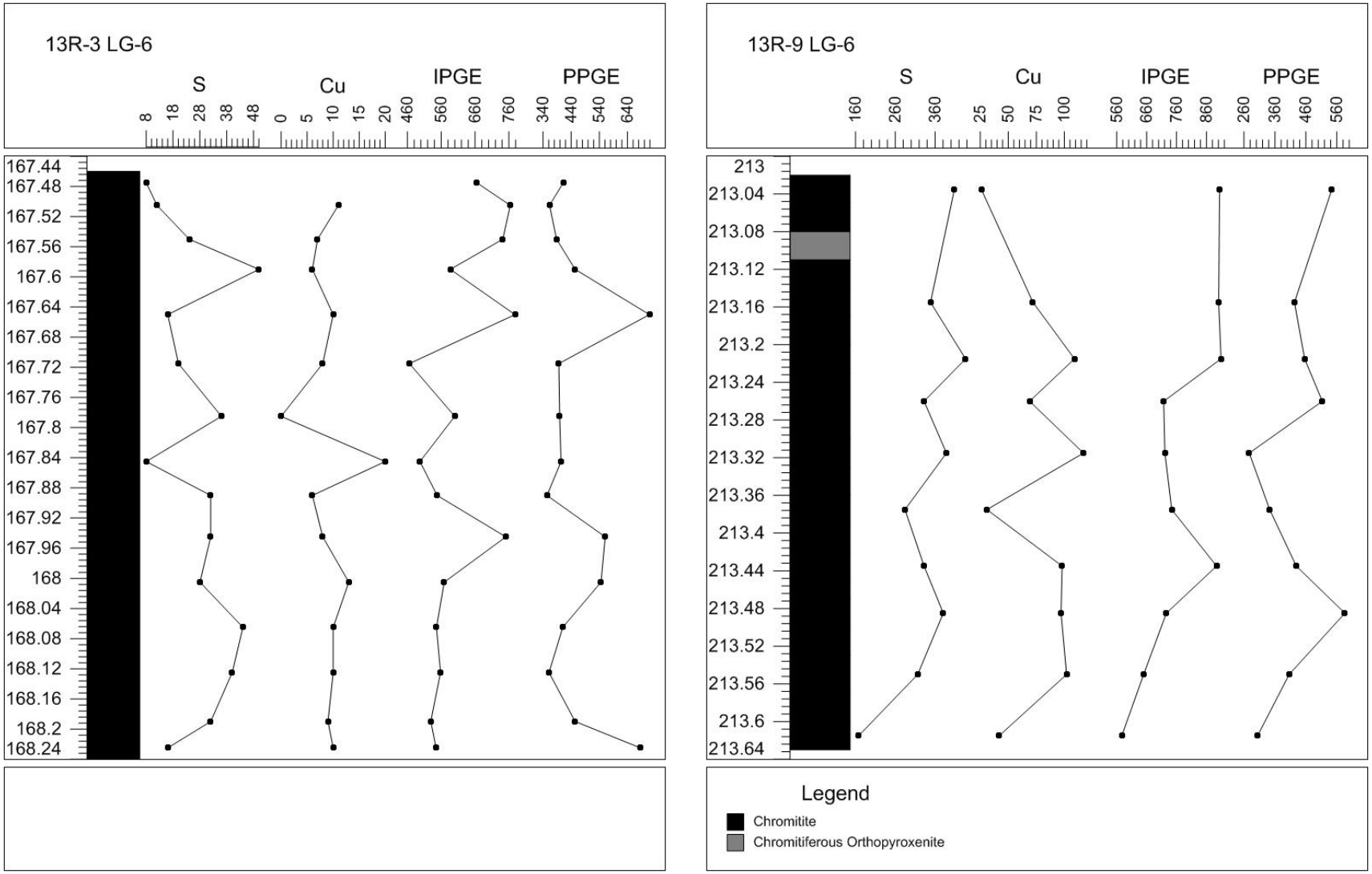

Figure 4.12: S (ppm), Cu (ppm), IPGE (ppb) and PPGE (ppb) variation for the LG-6 reef intersection from (a) 13R-3 and (b) 13R-9.

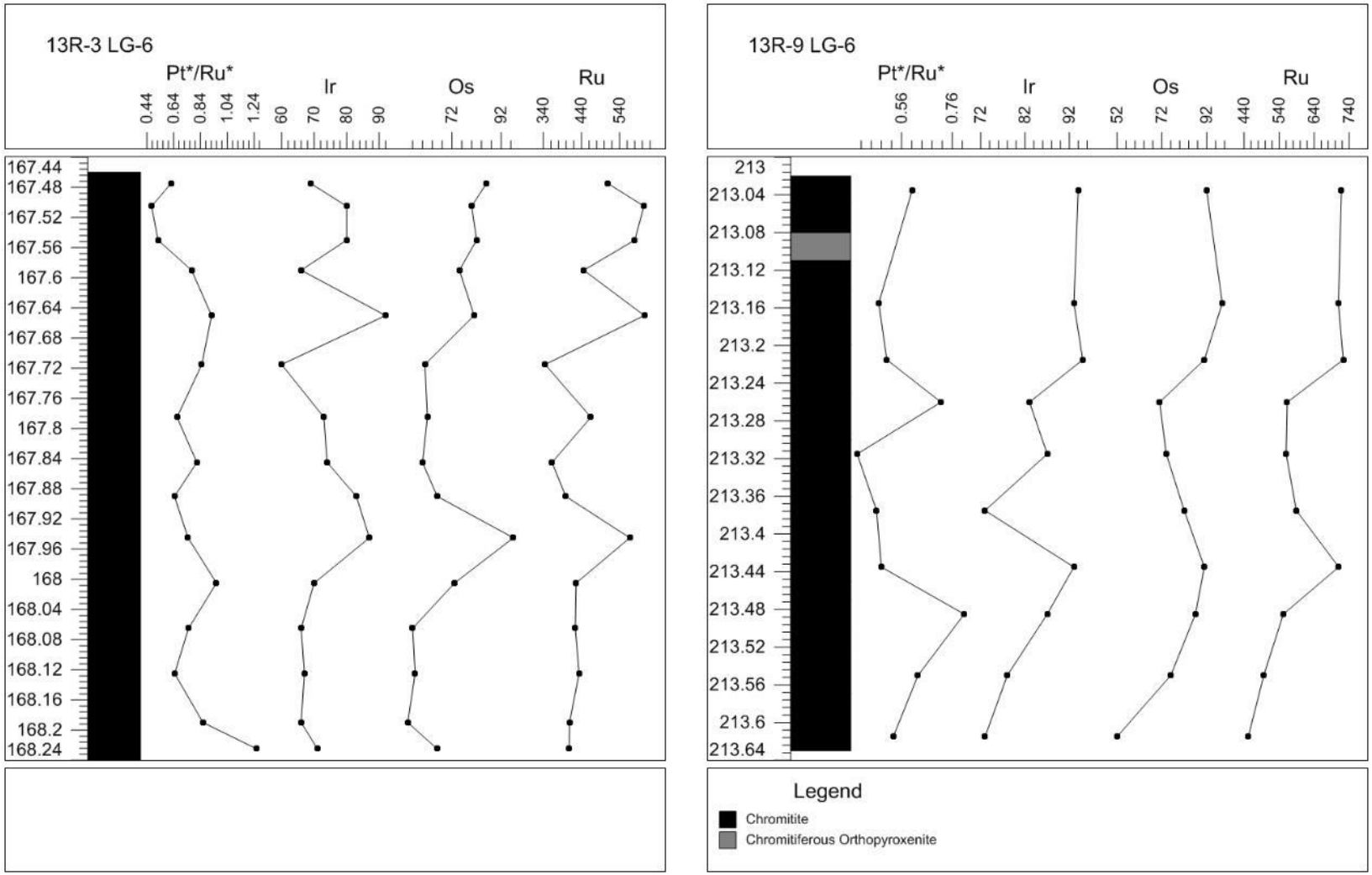

Figure 4.13: Pt*/Ru*, Ir (ppb), Os (ppb) and Ru (ppb) variation for the LG-6 reef intersection from (a) 13R-3 and (b) 13R-9.

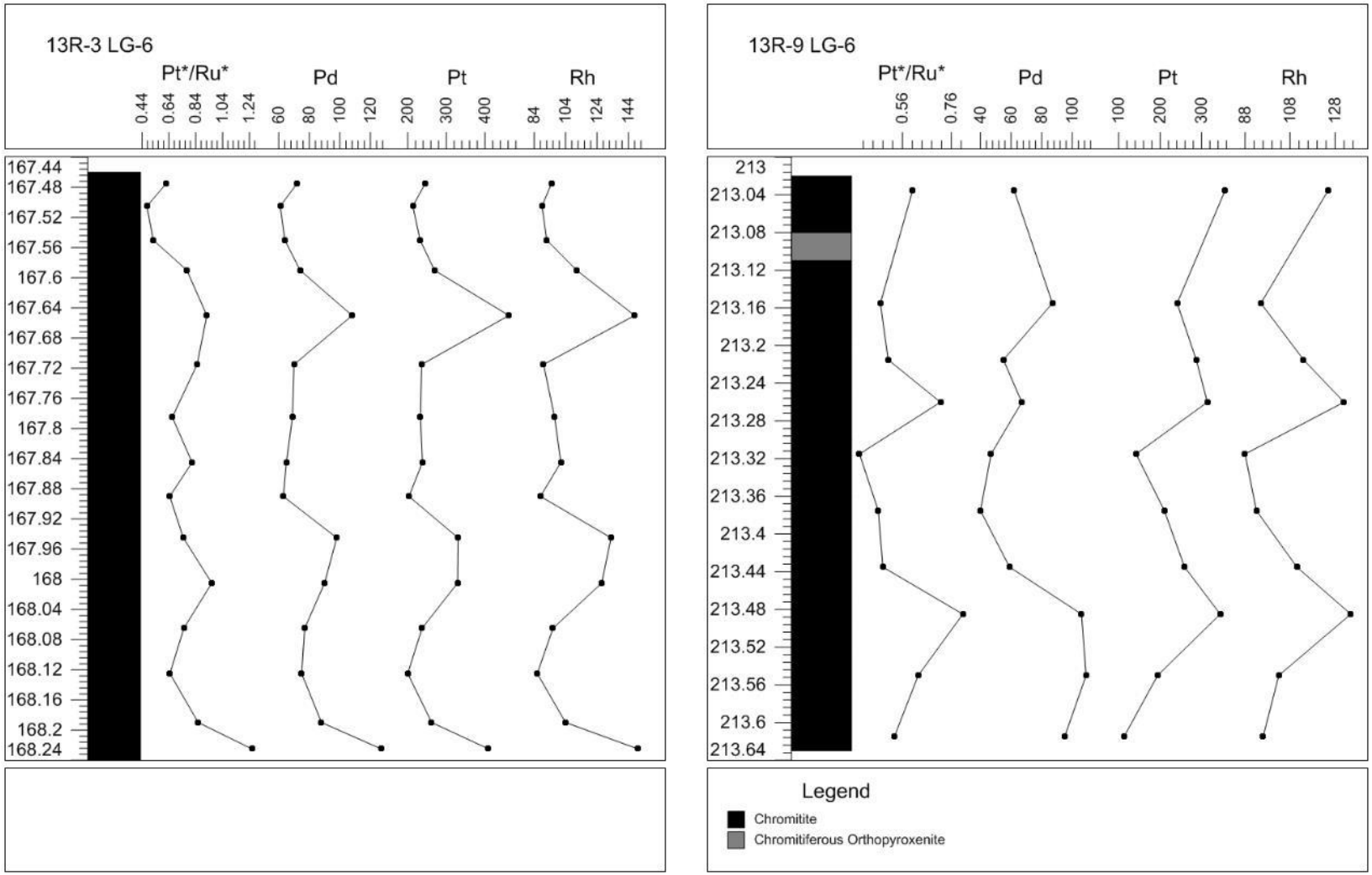

Figure 4.14: Pt*/Ru*, Pd (ppb), Pt (ppb) and Rh (ppb) variation for the LG-6 reef intersection from (a) 13R-3 and (b) 13R-9.

Figure 4.15 displays minimal variation in the Ni content of both boreholes, although each borehole has a different mean (13R-3 = 886.2 ppm mean, 13R-9 = 578.8 ppm). The difference of the mean Ni contents is 307.4 ppm with a std dev of the difference of the means being 18.3. Of greater significance is the S content, 13R-3 has a mean S of 26.6 ppm whereas 13R-9 has a mean S of 339.6 ppm, the difference of the means is 313.0 ppm with a std dev of the difference of the means being 22.9 (Figure 4.15). Figure 4.16 displays that 13R-3 has negligible Cu content (13.4 ppm mean Cu) in contrast to 13R-9 which has a mean Cu content of 76.4 ppm, this means that 13R-9 has more than 5 times the amount of Cu compared to 13R-3. The difference of the means for Cu is 63 ppm with the std dev of the difference of the means being 10.6. Figure 4.17 demonstrates that both 13R-3 and 13R-9 have similar Zn contents. 13R-3 has 599.2 ppm mean Zn whereas 13R-9 has 607.6 ppm Zn, the difference being that 13R-9 exhibits a slightly negative correlation with S increasing as Zn decreases, with R^2 = 0.6. Figure 5.18 displays how 13R-9 is slightly depleted in Co (13R-3 = 269.0 ppm mean, 13R-9 = 243.7 ppm mean). It should be noted though that Co has limited solubility in sulphide. Figure 5.19 demonstrates that both 13R-3 and 13R-9 have similar total PGE contents, 13R-3 has 1077.7 ppb $PGE_{(tot)}$ mean and 13R-9 has 1207.8 ppb $PGE_{(tot)}$ mean. Both boreholes also display similar PPGE values, the difference is in their IPGE content, with 13R-3 having 614.6 ppb mean IPGE and 13R-9 having 779.7 ppb mean IPGE. The difference in their mean IPGE content is 165.1 ppb with the std dev of the difference of the means being 46.2.

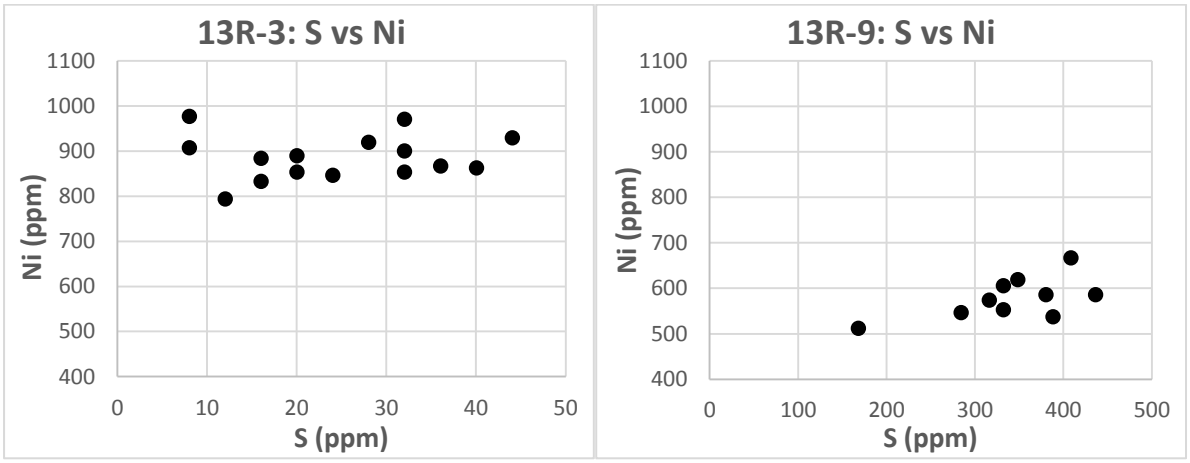

Figure 4.15: Ni vs V for LG-6 reef intersection from boreholes 13R-3 and 13R-9

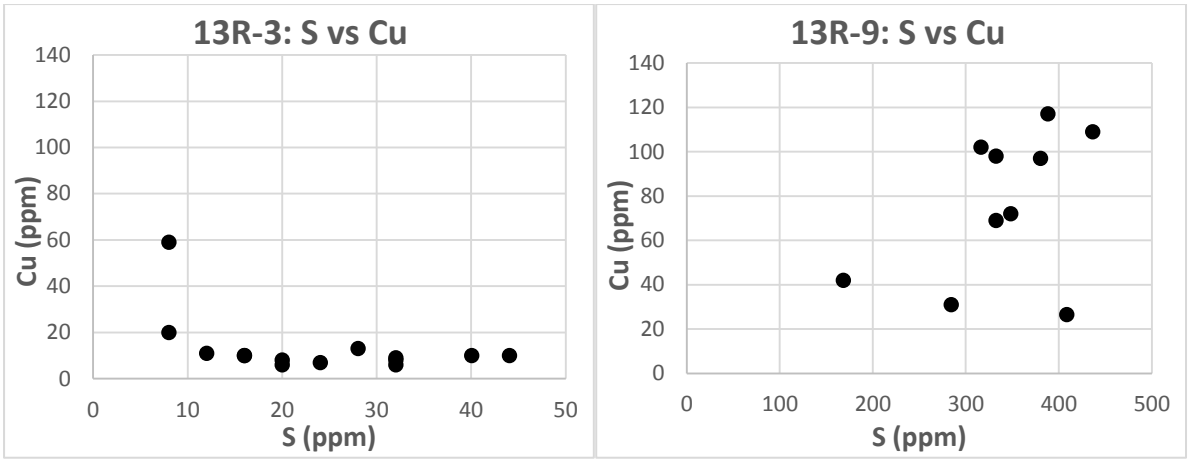

Figure 4.16: Cu vs Zn for LG-6 reef intersection from boreholes 13R-3 and 13R-9

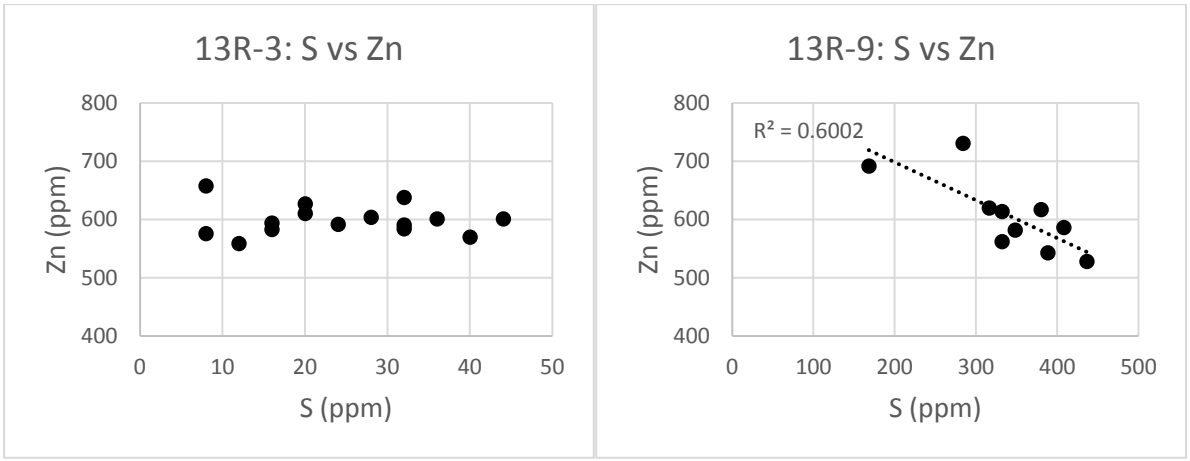

Figure 4.17: S vs Zn for the LG-6 reef intersection from boreholes 13R-3 and 13R-9

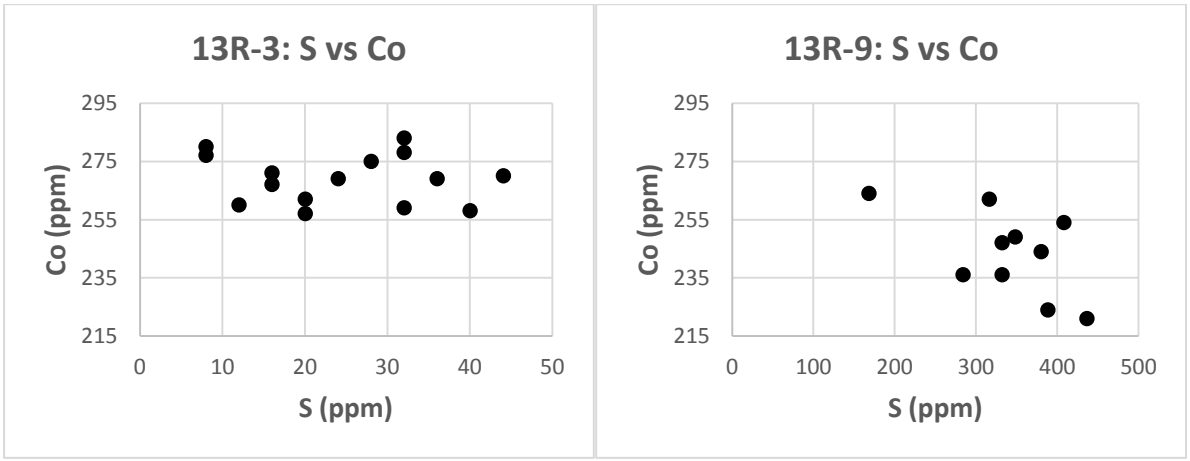

Figure 4.18: Co vs S for LG-6 reef intersection from 13R-3 and 13R-9

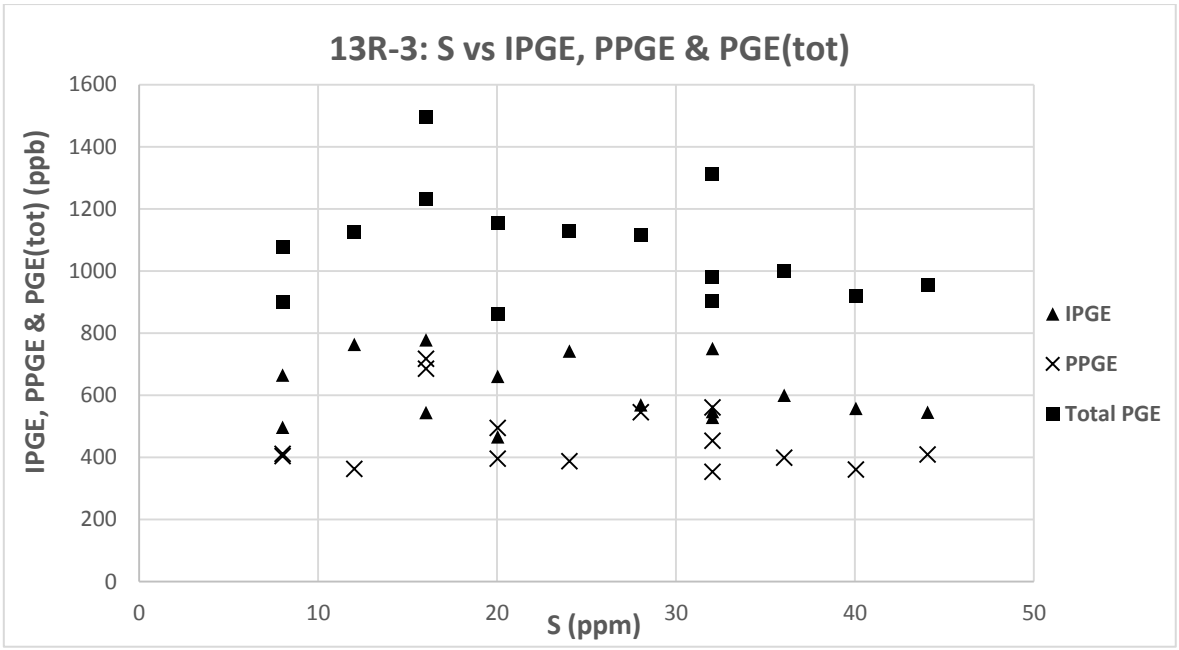

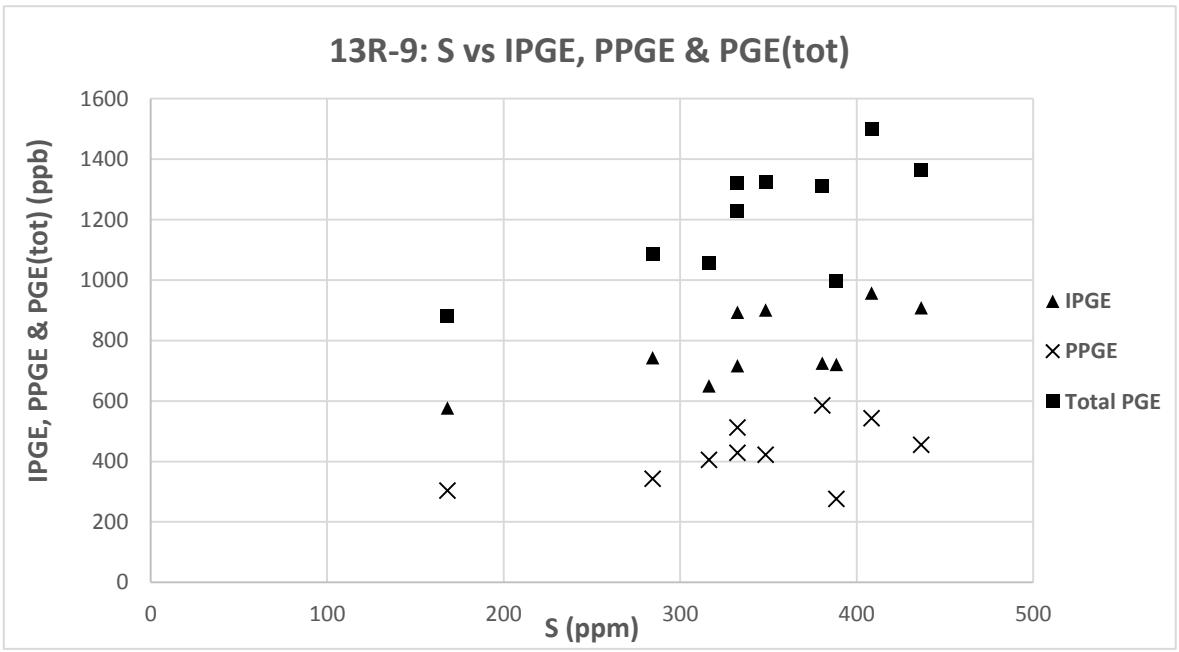

Figure 4.19: S vs IPGE, PPGE and $PGE_{(tot)}$ for LG-6 reef intersection from 13R-3 and 13R-9

Plotting PGE's against each other on a binary plot can be used to define the host minerals for the PGE's in mafic rocks. A linear trend illustrates a good chemical correlation between the two elements which can be interpreted as the two elements occurring in the same mineral phase.

For both boreholes the Ru has a slight positive correlation with both the Ir and Os (Figure 4.20), although more so for 13R-9. 13R-9 also has 142.0 ppb (with std dev of the difference of the means being 38.5) mean more Ru compared to 13R-3. Pt correlates positively with Rh for both boreholes

(Figure 4.21). Pt also correlates well with Pd for borehole 13R-3 however, has zero correlation for 13R-9.

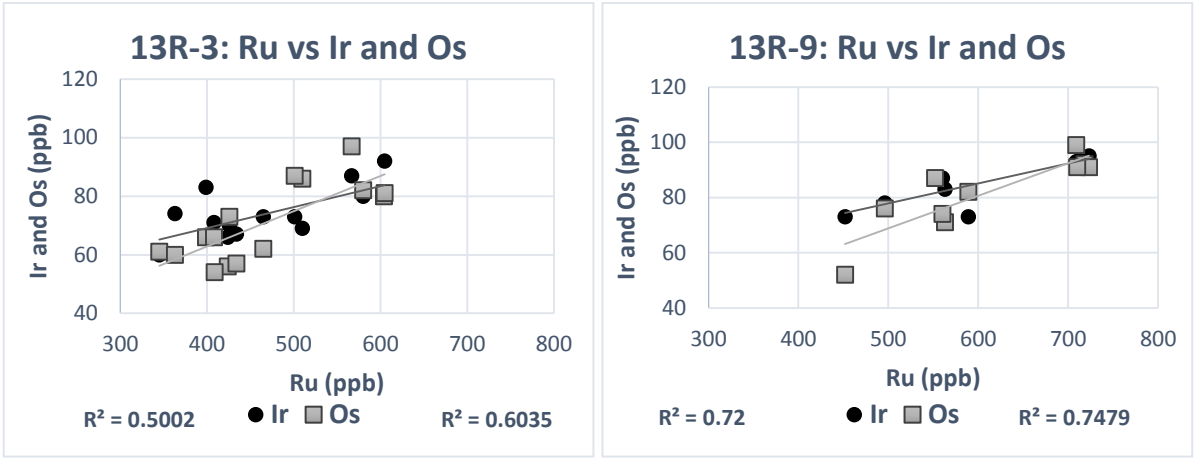

Figure 4.20: Ru vs Ir and Os for LG-6 reef intersection from boreholes 13R-3 and 13R-9

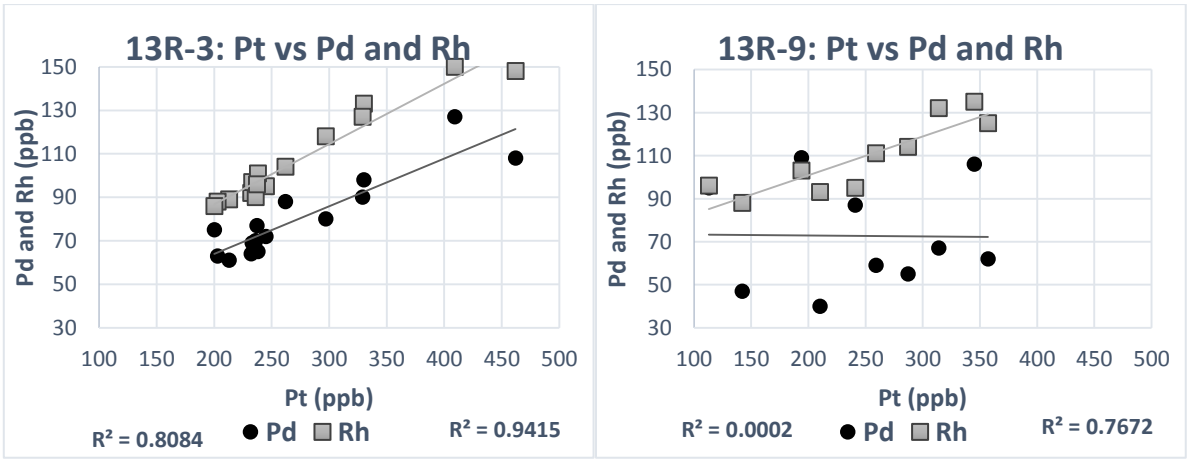

Figure 4.21: Pt vs Pd and Rh for LG-6 reef intersection from boreholes 13R-3 and 13R-9

4.5 Mineral chemistry

Due to technical difficulties with the electron probe only four thin sections were analysed, these four thin sections represent different stratigraphic heights in the boreholes (Figure 4.22). This means that unfortunately cr-spinel was not analysed directly from the reef. Representative thin sections were chosen for analysis of the footwall and hanging wall rocks in the normal borehole (13R-3) as well as

the borehole with elevated signatures (13R-9). The analyses 3FW, 9FWa, 9FWb and 9HW respectively correspond with samples 13R-3/168.24A, 13R-9/213.63D, 13R-9/213.63H and 13R-9/212.90B. They are renamed due to the repeated referral to each sample. Several analyses were done on each of the thin sections, to see the EPMA data go to Appendix E to G, the means and standard deviation calculations can be found in Appendix H and to see a breakdown of the analyses of each sample see Appendix J.

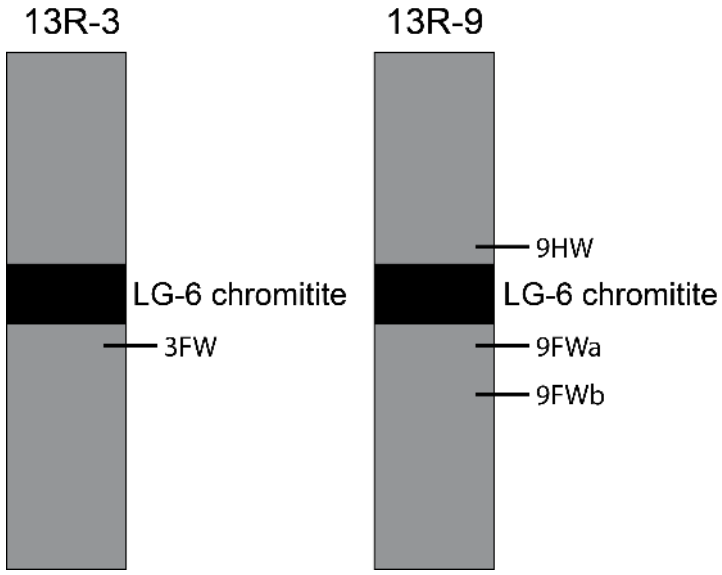

Figure 4.22: Sketch of boreholes 13R-3 and 13R-9 with the approximate location from where each of the thin sections that was used for mineral chemistry analysis is situated.

4.5.1 Cr-Spinel

The Mg# (Figure 4.23) for 9HW (mean 40.9) is higher than 9FWa and 9FWb (mean 33.1). The Cr# of 3FW (mean 70.6) is higher than 9FWa (mean 57.5) although they are from a comparable level in the stratigraphy (Figure 4.23). This is unlikely to be related to Cr_2O_3 contents (3FW = 43.2 wt. % mean, 9FWa = 40.5 wt. % mean), but due to significantly more Al_2O_3 (Figure 4.24) in 13R-9 (3FW = 12.1 wt. % mean, 9FWa = 20.1 wt. % mean). 9FWa and 9FWb have a mean Cr/Fe ratio of 1.3 (Figure 4.25), whereas 3FW is slightly depleted at 1.2 mean Cr/Fe and 9HW has an elevated Cr/Fe ratio of 1.7 mean. Borehole 13R-3 has higher mean Ni content (Figure 4.25) than 13R-9 (9HW = 513.4 ppm mean, 9FWa = 602.4 ppm mean, 9FWb = 377.2 ppm mean, 3FW = 1021.5 ppm mean). Therefore the olivine that occurs in 13R-9 would preferentially concentrates the Ni leaving the Cr-spinel reef of 13R-9 relatively depleted in Ni compared to 13R-3.

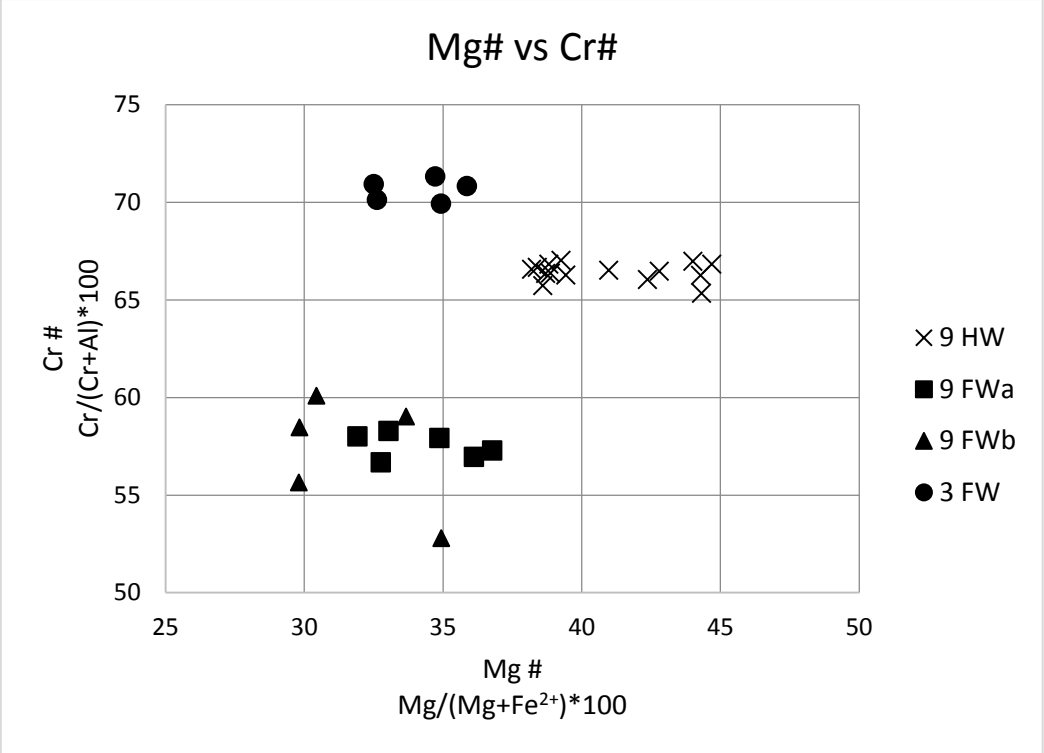

Figure 4.23: Mg# vs Cr# from mineral chemistry of boreholes 13R-3 and 13R-9 for Cr-spinel.

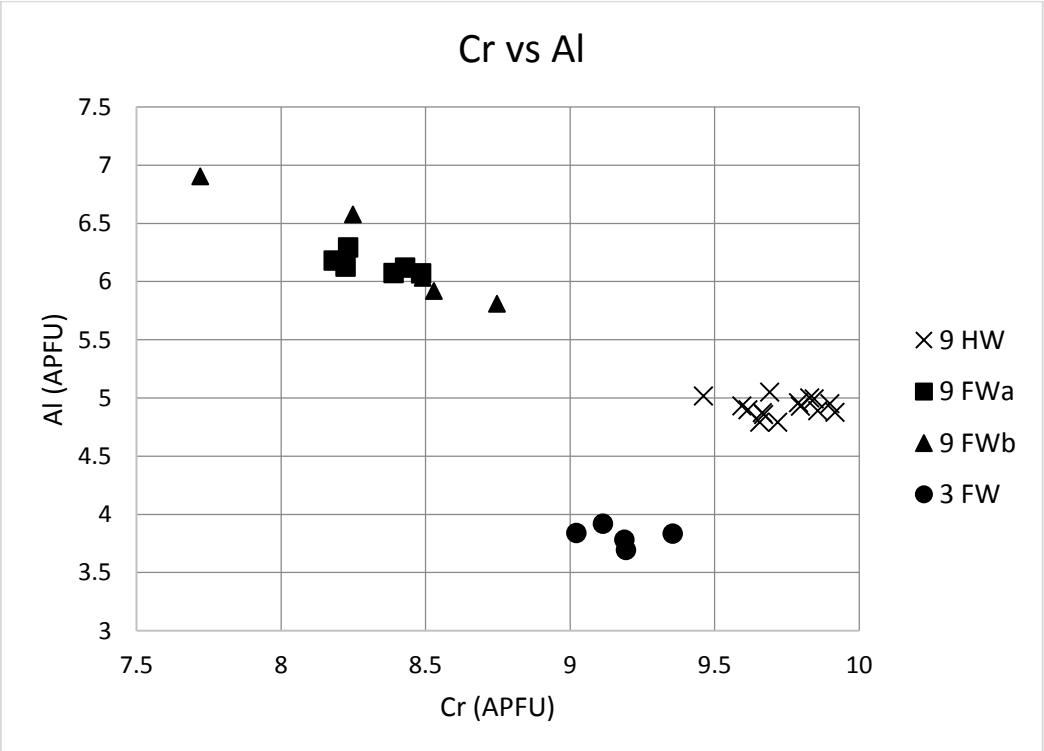

Figure 4.24: Cr vs Al from mineral chemistry of boreholes 13R-3 and 13R-9 for Cr-spinel.

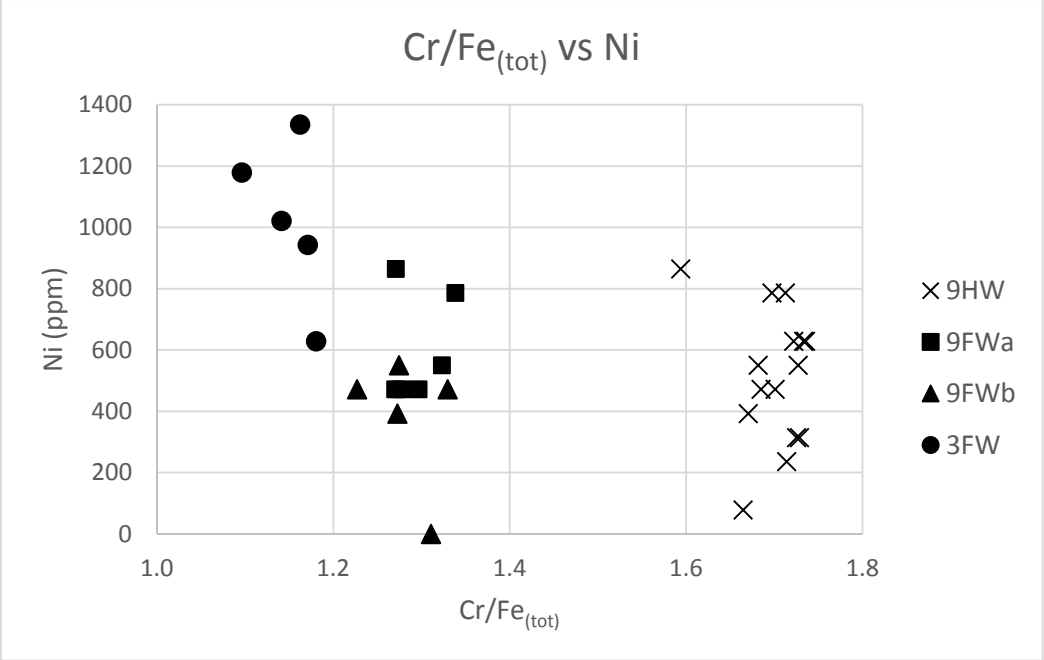

Figure 4.25: Cr/Fe ratio vs Ni from mineral chemistry of boreholes 13R-3 and 13R-9 for Cr-spinel.

4.5.2 Orthopyroxene

3FW and 9HW have a higher Mg# (Figure 4.26) than 9FWa and 9FWb (3FW = 84.4 mean, 9HW = 85.8 mean, 9FWa = 82.7 mean, 9FWb = 81.7 mean).

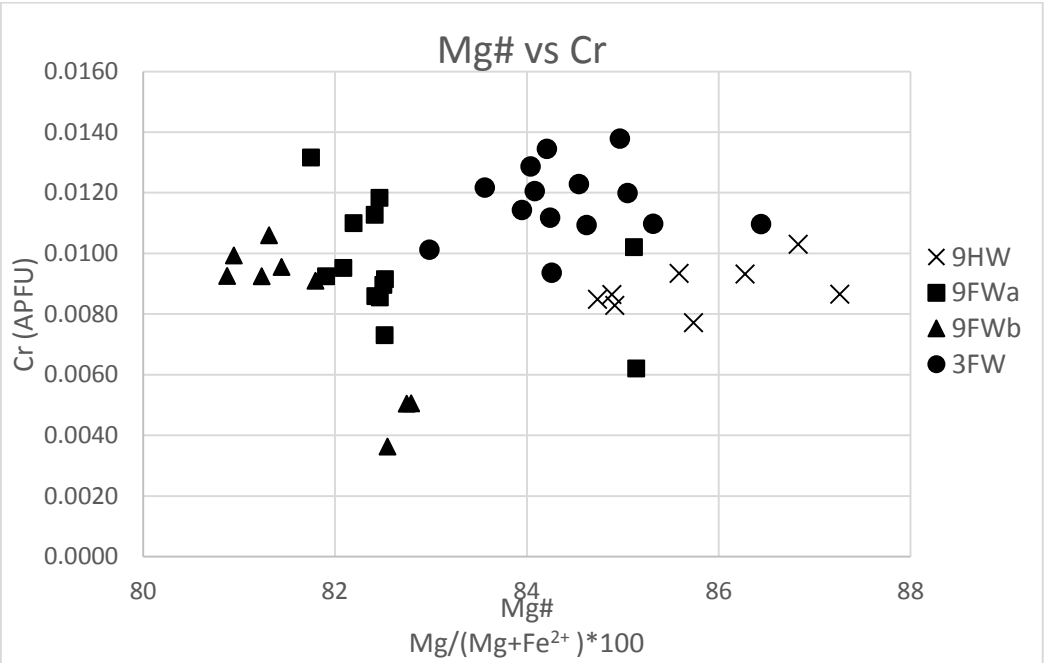

Figure 4.26: Mg# vs Cr from mineral chemistry of boreholes 13R-3 and 13R-9 for orthopyroxene.

4.5.3 Olivine

9HW has a higher Mg# (Figure 4.27) than 9FWa and 9FWb (9HW = 85.3 mean, 9FWa = 81.0 mean, 9FWb = 79.9 mean). There is no significant variation in the nickel content between the hanging wall and the foot wall (HW 1938.3 ppm mean Ni, FW 1993.6 ppm mean Ni).

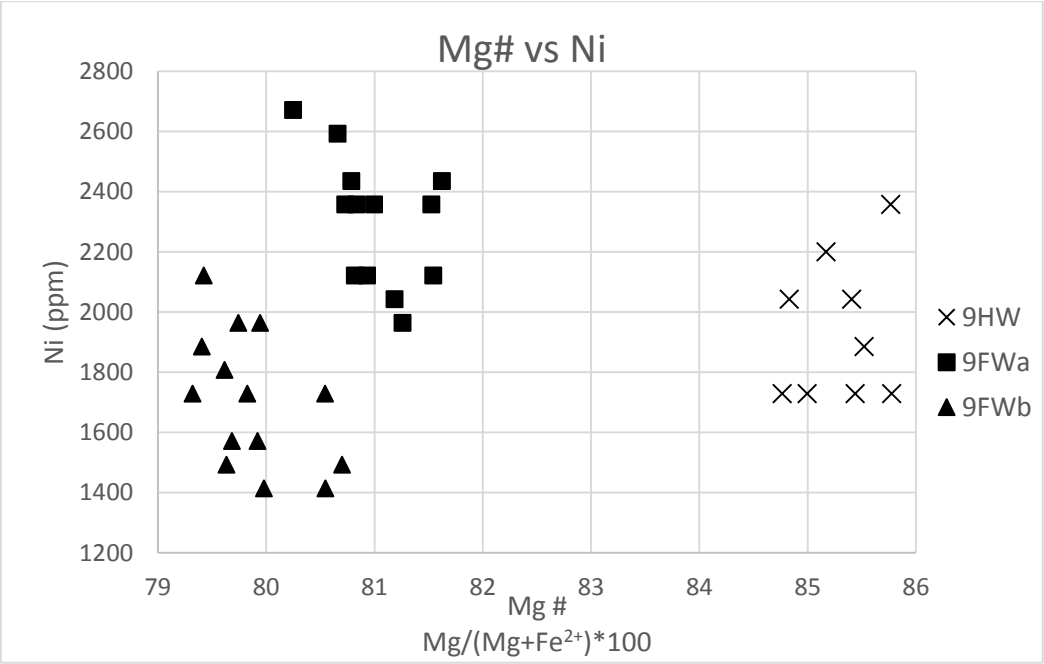

Figure 4.27: Mg# vs Ni from mineral chemistry of borehole 13R-9 for olivine.

4.6 Summary

The major differences occur in 13R-9 where harzburgite occurs as well as within the main chromitite reef (LG-6). There is evidence from both boreholes to suggest that there were multiple magma pulses involved in the formation of the reef (Figure 4.10 and Figure 4.11), seen in the reversals of the geochemical trend. A closer look focusing on the chromitite reef reveals that 13R-3 is deficient in Cu and S. As expected with the increased Cu and S in 13R-9, there is a corresponding increase in the $PGE_{(tot)}$ content specifically IPGE. However Figure 4.12 shows that the upward increase in PGE's corresponds with an upward increase in S and that the Cu is decoupled as it decreases going upward. Although 13R-9 has more than 10 times the amount of S (Figure 4.18) and more than 5 times the

amount of Cu (Figure 4.16) compared to 13R-3, it only has 1.1 times the amount of total PGE (13R-3 = 1077.7 ppb, 13R-9 = 1207.8 ppb) (Figure 4.12). The Mg# calculated from the mineral chemistry of the Cr-spinel (Figure 4.23), orthopyroxene (Figure 4.26) and olivine (Figure 4.27) crystals separate borehole 13R-9 into two groups, namely the HW and the FW. 9HW has a higher Mg# than both 9FWa and 9FWb this is due to a lower FeO and a slightly higher MgO. For the Cr-spinel mineral chemistry, 9HW has a higher Cr/Fe ratio than 9FWa and 9FWb (Figure 4.25).

5. Discussion

The LG-6 chromitite is laterally consistent along the entire western limb of the Bushveld Complex. Typically it is hosted by orthopyroxenite and has a Cr/Fe ratio between 1.56 and 1.60 (Kinnaird et al, 2002), but this varies in the Ruighoek area where it can be hosted harzburgite and when hosted in these rocks it displays elevated Cr/Fe ratios up to 2.11.

From the models introduced in Section 1.6; magma mixing, addition of a crystal-poor chromite-saturated magma and magma stratification are considered to be the most important when evaluating development of the LG-6 chromitite at Ruighoek, in the context of the data presented above. Whereas gravity settling, ephemeral pressure increase, addition of H_2O and addition of a new magma with suspended Cr-spinel are unlikely to be involved in the formation of the LG-6 chromitite.

Gravity settling is discounted because separating the Cr-spinel crystals from the orthopyroxene or olivine crystals is implausible. It also cannot explain why there is an isolated area with an increased Cr/Fe ratio, even with the depression it could not explain the different geochemistry (e.g. Cr/Fe ratio) between the enriched and the normal reef.

Ephemeral pressure increase is a relevant mechanism for triggering Cr-spinel crystallisation throughout the entire magma chamber, but also cannot account for the geochemical differences between the normal and enriched reef in the Ruighoek area. This mechanism is also not plausible as experimental work by Roeder and Reynolds (1991) suggests that Cr solubility might actually increase with pressure and not decrease as previously thought.

Formation of the chromitite following addition of H_2O, as proposed by Nicholson and Mathez (1991) is unlikely because of the thickness of the LG-6 chromitite and the sheer volume of pyroxene host rock required to be dissolved to form the reef. Another limiting factor is the large mass of water needed to be added to a partially molten rock pile (Mondal and Mathez, 2007).

Addition of a new magma with suspended Cr-spinel crystals is implausible as it cannot account for the geochemical differences between borehole 13R-3 and 13R-9. If the LG-6 formed from a crystal slurry it would not be expected to have a different geochemistry in the depression. This is because the reef in both boreholes would have crystallised from the same crystal laden slurry. Another key aspect to this model from Mondal and Mathez (2007) is that the hanging wall and footwall have very similar geochemistry. However the mineral chemistries for Cr-spinel, orthopyroxene and olivine from this study for the enriched borehole 13R-9 display that all three minerals have a higher Mg# for the

hanging wall than for the footwall (Table 5.1). It should be noted that the compositions of Cr-spinel are not primary as they were done on Cr-spinel hosted in the hanging wall and footwall orthopyroxenite, as such the Cr-spinel would have been competing with orthopyroxene for Fe, Mg and other elements. The results are still significant particularly the Cr/Fe ratio, Mg#, Cr# and the Ni content of the hanging wall over the footwall. This provides evidence for a compositional reversal and testifies against the addition of a new magma with suspended Cr-spinel crystals as a model.

Table 5.1: Mean mineral Mg# for borehole 13R-9 hanging wall and footwall comparison

Mineral	Hanging wall Mg# (mean)	Standard Deviation	Footwall Mg# (mean)	Standard Deviation
Cr-spinel	40.9	2.4	33.0	2.0
Orthopyroxene	85.8	0.9	82.3	1.0
Olivine	85.3	0.4	80.4	0.4

Magma mixing is invoked because it explains how Cr-spinel can be the sole crystallising phase, it also explains why the reef geochemistry does not have a continuous fractionation trend. Magma mixing is also crucial in the formation of a stratified magma. In Figure 4.10 the Mg# for 13R-3 decreases upward from the base until the red line, where it resets and then decreases upward again. In Figure 4.11 the Cr# for 13R-9 decreases upward from the base until the red line, where it resets and then continues to decrease upward. The upward decreasing Mg# and Cr# is considered to be due to normal crystal fractionation trends, which is then reset by a new magma pulse followed by normal crystallisation again.

The addition of a new crystal-poor, chromite-saturated magma solves the chromium mass balance problem, while also explaining geochemical differences between the reef and host rocks (HW and FW) as well as discontinuities in geochemistry of the reef. If the reef and host rocks crystallised from the same magma source, the transition between the two would be gradational or at the very least they would have an upward fractionating trend. Figure 4.10 and 4.11 display an upward decreasing trend in Mg# and Cr# respectively, however, half way through the reef there is a sudden increase in Mg# and Cr# followed again by an upward decrease. The sudden break is interpreted to reflect a new pulse of magma (e.g. Sharpe, 1981; Hatton, 1984). These breaks and sudden increases may seem insignificant in size and some might attribute them to changes in the SiO_2 content, however they do

represent inconsistencies in the trend of the reef as a whole and the abrupt change in SiO_2 content would still need to be explained. Which the addition of a new magma does. Figure 4.23 illustrates how different the Cr-spinel mineral chemistry of the hanging wall and footwall of 13R-9 are from each other. The hanging wall has a higher Mg# (mean 40.9) and Cr# (mean 66.4) than the footwall (Mg# mean = 33.1, Cr# mean = 57.4). This means the magma from which the hanging wall crystallised was relatively more primitive than the magma that crystallised the footwall. The footwall of 13R-3 does have a higher Cr# than the footwall of 13R-9, however this has less to do with the Cr_2O_3 content and more to do with the fact that 13R-3 has a distinctly lower Al_2O_3 content. The reason 13R-9 has a higher Al2O3 content is because in an olivine-rich environment, chromitites have elevated Al compositions resulting from the co-precipitation of olivine (Eales et al, 1988). For the orthopyroxene mineral chemistry the Mg# of 13R-3 footwall is higher than the Mg# of 13R-9 footwall, this is because 13R-3 has a higher proportion of Fe^{3+} to Fe^{2+}. The reason for the higher Fe^{3+} to Fe^{2+} ratio is conceivably due to the presence of olivine in 13R-9. This is because olivine accommodates only Fe^{2+} in its crystal structure leaving less Fe^{2+} for other minerals like orthopyroxene. Figure 4.26 and 4.27 illustrate that for both the pyroxene and olivine mineral chemistry, the hanging wall has a higher Mg# than the footwall. As such, the sudden change in Mg# and Cr# within the reef; the increased Mg# and Cr# of the hanging wall mineral chemistry compared to the footwall; and the Cr-spinel in the hanging wall of borehole 13R-9 having a higher Cr/Fe ratio compared to the footwall all indicate that the reef formed from at least two magma pulses.

Magma stratification provides a means to crystallise a thick pile of chromitite, while also explaining why locally at Ruighoek, LG-6 has an elevated Cr/Fe ratio. As the lower most cell crystallises Cr-spinel the chemistry and temperature of that cell change, thus the cell becomes compositionally and thermally similar to the overlying cell, resulting in mixing and reviving of Cr-spinel crystallisation. The process repeats itself, forming a thick accumulation of Cr-spinel and a similar process results in the formation of the harzburgites from the addition of an olivine-saturated magma. Figure 2.1 illustrates a depression in the LG-6 reef, which is situated near borehole 13R-9. Figure 2.2 indicates that the elevated Cr/Fe associated with the reef for borehole 13R-9 corresponds with the depression (Figure 2.1). This is consistent with the conclusions made by Cawthorn et al (2016) that the addition of a relatively dense, primitive magma results in ponding at the base of depressions in the floor of the chamber. The more primitive melt at the base of the depression can account for the presence of olivine and the elevated Cr/Fe ratio.

Spatial variation of the LG-6 reef chemistry illustrates a depression in the vicinity of borehole 13R-9 (Figure 2.1). Associated with borehole 13R-9 and hence also the depression, there is relatively more primitive harzburgites and elevated Cr/Fe ratio (Figure 2.2). Whereas more typical characteristics like those of borehole 13R-3 occur at normal reef elevations (i.e. where the reef follows the regional dip).

Viljoen and Scoon (1985) looked at satellite iron-rich ultra-mafic pegmatites related to the Bushveld Complex and noted that they formed perpendicular to the plane of layering in the cumulate pile and as such suggested that the floor of the Bushveld magma chamber was sub-horizontal at the time of formation. Palaeomagnetic studies of the Bushveld Complex by Letts et al (2009) indicate that the Bushveld Complex was near horizontal at time the Rustenburg layered suite crystallised (Figure 5.1). If the floor was horizontal at the time of formation of the LG-6 chromitite, a stratified magma would produce a chromitite with the same Cr/Fe ratio everywhere. Some researchers (e.g. Carr et al, 1994) however, argue that the cumulate floor was inclined during crystallisation of the Critical Zone (specifically the Merensky Unit in the Upper Critical Zone). There is a lack of data to the east (down dip) of borehole 13R-9 (Figure 2.2) the trend of the data may be interpreted to mean that the cumulate floor was inclined during formation of the LG-6. This inclined cumulate floor in combination with the stratified magma (Figure 5.2) could account for the increasing Cr/Fe ratio down dip (eastward), however if you look at the wireframe model (Figure 2.1) it shows that the topography dips inward towards borehole 13R-9, as such I propose that the magma within the depression was stratified (Figure 5.3). To the north of Ruighoek on Assores Groenfontein farm another high Cr/Fe area was identified (Christelle van der Merwe, 2016, pers comm). This area has now been mined out and was found to be surrounded by normal Cr/Fe ratio reef on all sides, including down dip to the east (Figure 5.3).

Figure 5.1: Sketch of a stratified magma overlying a horizontal cumulate floor based on description by Viljoen and Scoon (1985). Due to the same cell within the stratified magma being in contact with the entire cumulate pile, the chromitite reef is expected to have similar geochemistry (e.g. Cr/Fe ratio) laterally.

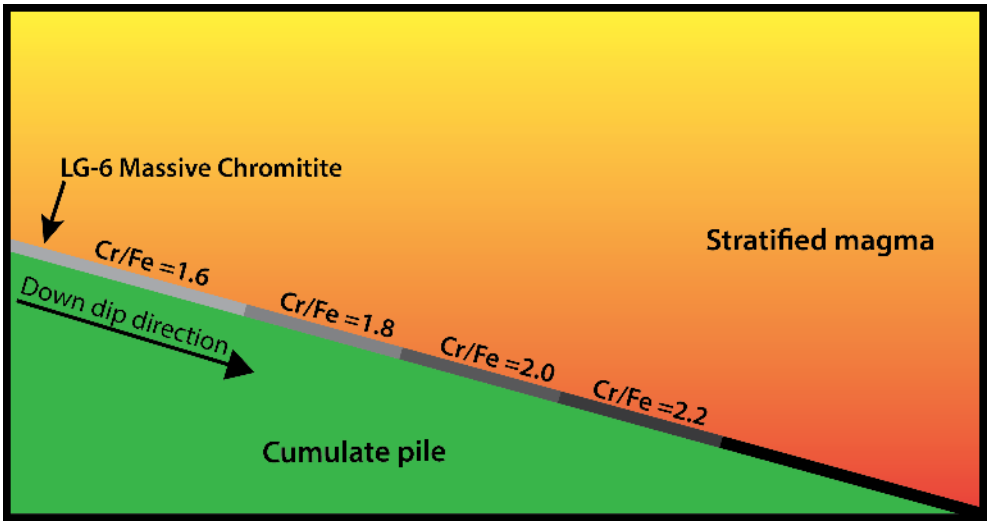

Figure 5.2: Sketch of a stratified magma overlying an inclined cumulate floor, illustrating how the Cr/Fe ratio would change down dip as layers from different heights of the stratified magma are in contact with the cumulate floor.

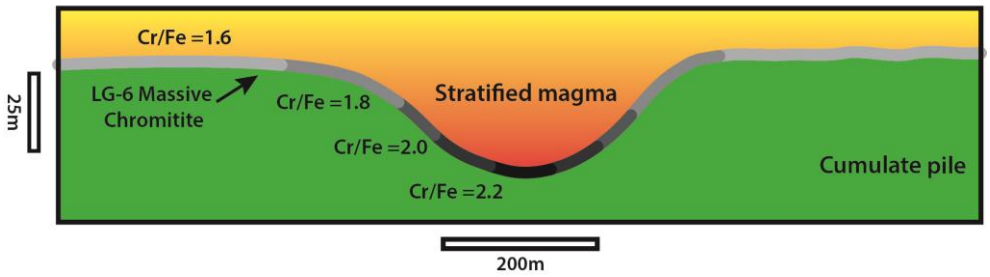

Figure 5.3: Sketch of a stratified magma overlying a depression in a cumulate floor with scale bars representing the dimensions of the depression found at Ruighoek. The massive chromitite reef displays how the Cr/Fe ratio would vary traversing from normal reef elevations into the depression.

Petrographically both boreholes 13R-3 and 13R-9 are very similar. The major difference between them is the presence of harzburgite rocks in 13R-9. The presence of olivine is interpreted to be an indication of relative primitivity of parental melt from which these rocks formed (Irvine, 1977; Eales et al, 1993), therefore the rock sequence in borehole 13R-9 is considered to be more primitive than that in 13R-3. The presence of olivine occurring stratigraphically above orthopyroxenite is also evidence that there were multiple magma pulses as it explains reversals in the fractionation trend seen in the geochemistry (e.g. Hatton (1984); Cawthorn and Walraven (1998)). The occurrence of orthopyroxene veins within the chromitite reef of 13R-9 (Figure 3.16) are likely a later stage compared to the co-magmatic and interstitially formed orthopyroxene (Figure 3.17). Evidence for the orthopyroxene veins

crystallising at a later stage is that they are characteristically lacking in interstitial sulphides, unlike the co-magmatic orthopyroxene.

The geochemical data confirm that the LG-6 reef in 13R-9 has an elevated Cr/Fe (max 2.11) ratio as previously identified by mining operations. The large scale, whole rock geochemical differences between the two boreholes are that borehole 13R-9 displays a more gradational contact between the LG-6 reef and the host harzburgites compared to borehole 13R-3, where the LG-6 reef has a sharp contact with the host orthopyroxenite. This is interpreted to be associated with greater thermal, chemical and/or mechanical erosion of the footwall followed by fractional crystallisation within borehole 13R-9. The presence of olivine in 13R-9 is the cause of the greater maximum MgO content in borehole 13R-9 compared to 13R-3. However, the total MgO content is affected by late stage alteration of olivine to serpentine with magnetite veins.

Previous work by Mitchell and Scoon (2007) produced a graph for several Bushveld Complex chromitite reefs. They plotted Cr/Fe ratio vs Pt*/Ru* ([Pt+Pd+Rh]/ [Ru+Os+Ir]) which showed that the chromitite reefs formed distinct groups. The data from this study has been added to their diagram and the LG-6 reef from the enriched 13R-9 borehole can be seen to plot very differently to the LG-6 reef from other areas of the Bushveld Complex (Figure 5.4). The LG-6 for borehole 13R-9 plots in the same area as the LG-1 to LG-4 chromitites from Mitchell and Scoon (2007). This indicates that the LG-6 from 13R-9 in the Ruighoek area is more primitive than the LG-6 from elsewhere in the Bushveld Complex.

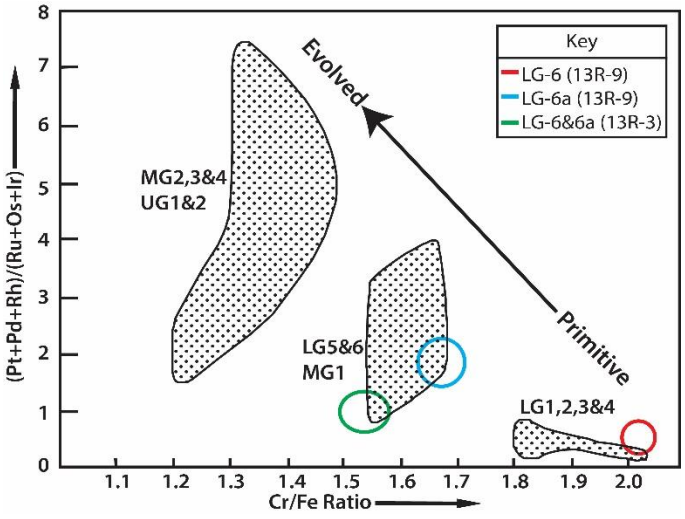

Figure 5.4: Plot illustrating the grouping of the different chromitite reefs based on plotting of Cr/Fe ratio vs Pt*/Ru*. Notably LG-6 from borehole 13R-9 plots with a different group than expected (adapted from Mitchell and Scoon, 2007).

For 13R-3 the fact that the mean S content is 26.6 ppm with a std dev of 12.6, indicates that the Sulphur content is actually negligible. Especially in comparison to 13R-9 which has a mean S content of 339.6 ppm with a std dev of 71.7. Borehole 13R-9 also has a higher IPGE content than 13R-3 with the difference of the means being 165.1 ppb and the std dev of the difference of the means being 46.2. More notably Figure 5.19 indicates that 13R-9 has a slightly positive correlation with respect to S and the IPGE content. The elevated IPGE and S content of the reef in borehole 13R-9 compared to 13R-3 is likely due to the addition of the new Cr saturated magma, which is likely enriched in S and also IPGE's. The enrichment of IPGE's in 13R-9 also causes it to have a lower than expected Pt*/Ru* ratio (Figure 5.4).

5.1 Model for formation of LG-6 at Ruighoek

The following syntheses the postulated sequence of events that is consistent with the data available, and arguments presented, for the formation of the LG-6 chromitite at Ruighoek.

At the time of formation of the LG-6 there is a pre-existing depression in the cumulate pile, which is situated in the vicinity of borehole 13R-9 (Figure 5.5A). The resident magma is stratified and crystallising orthopyroxene.

The chamber is replenished with a new, relatively primitive and olivine-saturated magma from a local feeder into the depression (Figure 5.5B). This new magma mixes with the basal layer and due to differences in composition and temperature, it stratifies and forms double diffusive convection cells (Figure 5.5B). This newly stratified basal layer crystallises harzburgites in the depression.

There are multiple pulses of new, relatively primitive, chromite-saturated magma into the depression (Figure 5.5C). The new magma mixes with the current basal layer and due to compositional and temperature differences it stratifies. Once stratified, it crystallises Cr-spinel, which develops the LG-6 chromitite with varying Cr/Fe ratios (visualized as different shades of grey, Figure 5.5C). The highest Cr/Fe values occur in the depression with the Cr/Fe ratio decreasing gradually up the slope to normal values within the flat lying areas outside the depression. Multiple replenishments of chromite-saturated magma are inferred responsible for the formation of the LG-6, as indicated by the geochemical data (Figure 4.10 and Figure 4.11). The multiple replenishments act to thicken the LG-6 chromitite and as such satisfy the mass balance issue (Figure 5.5D).

After formation of the LG-6 there is a pulse of relatively primitive, olivine-saturated magma that enters into the depression through the local feeder (Figure 5.5D). This pulse mixes with the current basal layer and stratifies, once stratified it crystallises harzburgites in the depression (Figure 5.5D).

A further replenishment by an orthopyroxene-saturated magma occurs. This mixes with the current basal layer and then stratifies. Once stratified it crystallises the orthopyroxenite (Figure 5.5E). After all the magma replenishment events, the magma chamber undergoes fractional crystallisation (Figure 5.5F), forming the orthopyroxenite hanging wall. Figure 5.5F illustrates the relative position of two boreholes from this study (13R-3 and 13R-9).

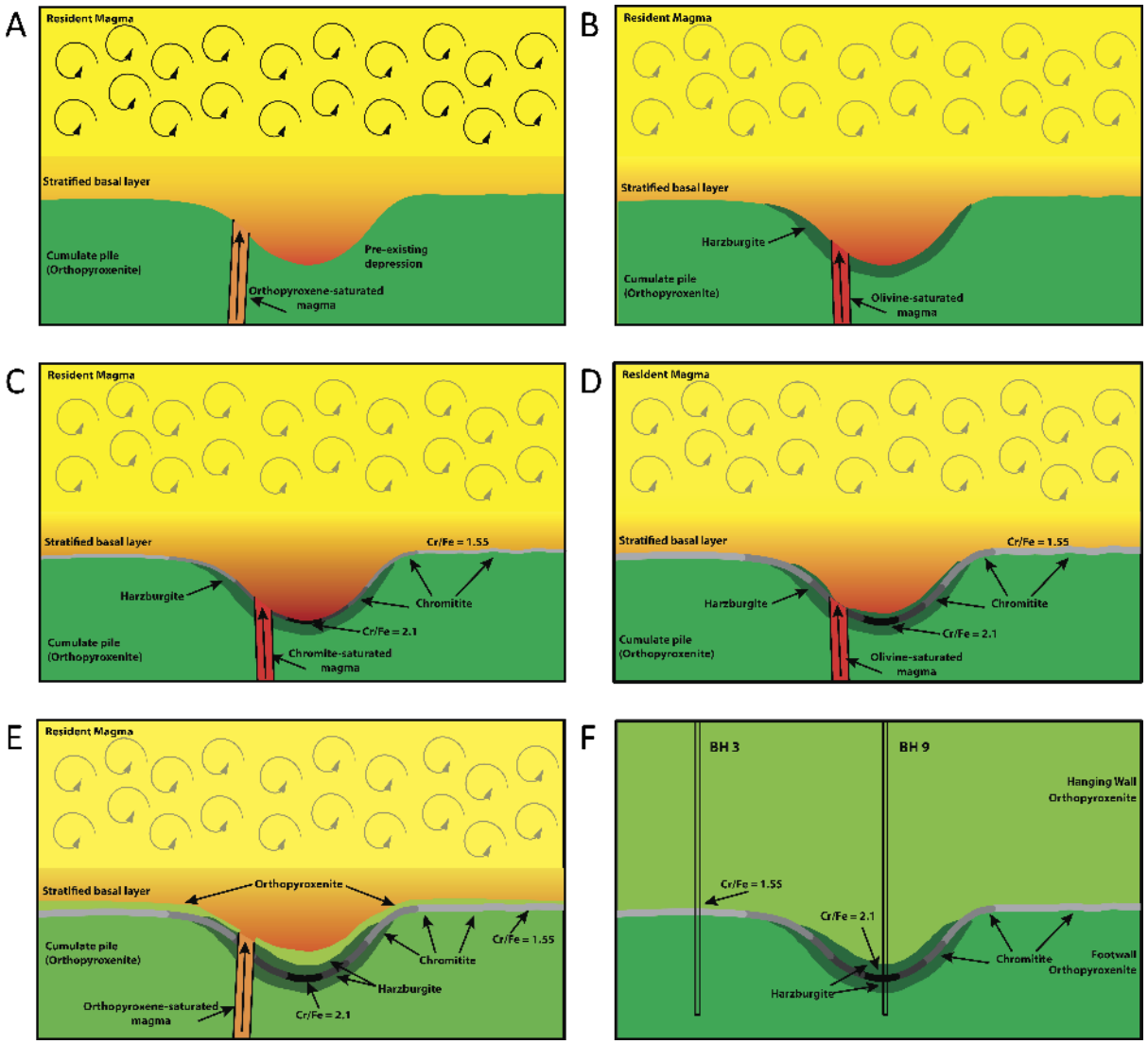

Figure 5.5: Cartoon illustrating the processes involved in the formation of the LG-6 chromitite at Ruighoek mine (see text for further discussion).

6. Summary and Conclusions

The vertical and lateral variations in the Cr/Fe ratio at Ruighoek provided the opportunity to study the processes involved in the formation of the LG-6 chromitite. The LG-6 chromitite formed in association with multiple replenishment events. The new magma was relatively primitive, chromite-saturated, with the compositional and temperature differences between the replenishing and resident magmas resulting in magma stratification. This stratification in combination with a pre-existing depression in the footwall rocks caused the densest and thus most primitive magmas to accumulate in the depression, forming harzburgite and crystallising chromitite with an elevated Cr/Fe ratio. The addition of a relatively more primitive magma is suggested to form the hanging wall with the higher Mg# ratios compared to the footwall.

Recommended future work:

To further test this model, it is recommended a smaller scale, more detailed study of the reef intersections geochemistry would be helpful in identifying other potential magma additions. Electron probe microanalysis of the more than 40 polished thin sections from this study should include. Finally a more detailed investigation into the second high Cr/Fe area to the north of Ruighoek at Assores Groenfontein farm could provide further evidence for the findings of this study.

References

Ashwal, D. L., Webb, S. J., and Knoper, M. W., 2005, Magmatic stratigraphy in the Bushveld Northern Lobe: continuous geophysical and mineralogical data from the 2950 m Bellevue drillcore: South African Journal of Geology, v. 108, p. 199-232.

Bailie, R. H., and Robb, L., 2004, Polymetallic Mineralization in the granites of the Bushveld Complex - Examples from the central south eastern lobe. : South African Journal of Geology, v. 107, no. 4, p. 633-652.

Cameron, E. N., 1977, Chromite in the central sector of the Eastern Bushveld Complex, South Africa: American Mineralogist, v. 62, p. 1082-1096.

Campbell, I. H., and Turner, J., 1986, The influence of viscosity on fountains in magma chambers: Journal of Petrology, v. 27, no. 1, p. 1-30.

Carr, H. W., and Groves, D. I., 1994, The importance of synmagmatic deformation in the formation of Merensky Reef potholes in the Bushveld Complex: Economic Geology, v. 89, no. 6, p. 1398-1410.

Cawthorn, R. G., 2015, The Bushveld Complex, South Africa, Layered Intrusions, Springer, p. 517-587.

Cawthorn, R. G., Eales, H. V., Walraven, F., Uken, R., and Watkeys, M. K., 2006, The Bushveld Complex, *in* Anhaeusser, M. R., and Thomas, R. J., eds., The Geology of South Africa: Pretoria, Geological Society of South Africa, Johannesburg, p. 261-282.

Cawthorn, R. G., and Walraven, F., 1998, Emplacement and crystallization time for the Bushveld Complex: Journal of Petrology, v. 39, no. 9, p. 1669-1687.

Cawthorn, R. G., Lundgaard, K. L., Tegner, C., and Wilson, J. R., 2016, Lateral variations in plagioclase compositions, Main Zone, Bushveld Complex, South Africa: Evidence for slow mixing of magmas in basinal structures: Mineralogical Magazine, v. 80, no. 2, p. 213-225.

Cawthorn, R. G., and Webb, S. J., 2001, Connectivity between the western and eastern limbs of the Bushveld Complex: Tectonophysics, v. 330, p. 195-209.

Coertze, F., Walraven, F., Marlow, A., MacCaskie, D., and Burger, A., 1978, Field relations and age determinations in the Bushveld Complex.

Cousins, C. A., and Feringa, G., 1964, The chromite deposits of the western belt of the Bushveld Complex., *in* Haughton, S. H., ed., The Geology of some Ore Deposits in Southern Africa.: Johannesburg, Geological Society of South Africa, p. 183-202.

Droop, G., 1987, A general equation for estimating Fe3+ concentrations in ferromagnesian silicates and oxides from microprobe analyses, using stoichiometric criteria: Mineralogical Magazine, v. 51, no. 361, p. 431-435.

Du Toit, A. L., 1926, The Bushveld Igneous Complex and the associated rocks, London: Oliver & Boyd, p. 136 – 150.

Eales, H., Field, M., De Klerk, W., and Scoon, R., 1988, Regional trends of chemical variation and thermal erosion in the Upper Critical Zone, western Bushveld Complex: Mineralogical Magazine, v. 52, no. 364, p. 63-79.

Eales, H., Teigler, B., and Maier, W., 1993, Cryptic variations of minor elements A1, Cr, and Mn in Lower and Critical Zone orthopyroxenes of the Western Bushveld Complex: Mineralogical Magazine, v. 57, p. 257-264.

Eales, H. V., 2000, Implications of the chromium budget of the Western Limb of the Bushveld Complex: South African Journal of Geology, v. 103, no. 2, p. 141-150.

Eales, H. V., and Cawthorn, R. G., 1996, The Bushveld Complex, *in* Cawthorn, R. G., ed., Layered Intrusions. Developments in Petrology, Volume 15, p. 181-229.

Eales, H. V., and Costin, G., 2012, Crustally Contaminated Komatiite: Primary Source of the Chromitites and Marginal, Lower, and Critical Zone Magmas in a Staging Chamber Beneath the Bushveld Complex: Economic Geology, v. 107, no. 4, p. 645-665.

Eriksson, P.G., Altermann, W., and Hartzer, F.J., 2006, The Transvaal Supergroup, *in* Anhaeusser, M. R., and Thomas, R. J., eds., The Geology of South Africa: Pretoria, Geological Society of South Africa, Johannesburg, p. 237-260.

Ford, C., Biggar, G., Humphries, D., Wilson, G., Dixon, D., and O'Hara, M., Role of water in the evolution of the lunar crust; an experimental study of sample 14310; an indication of lunar calc-alkaline volcanism, *in* Proceedings Lunar and Planetary Science Conference Proceedings 1972, Volume 3, p. 207.

Gaetani, G. A., Grove, T. L., and Bryan, W. B., 32. Experimental phase relations of basaltic andesite from hole 839B under hydrous and anhydrous conditions, *in* Proceedings Proceedings of the Ocean Drilling Program, scientific results1994, Volume 135, p. 557-563.

Glazner, A. F., 2014, Magmatic Life at low Reynolds number: Geology, V42, no. 11, p. 935 – 938.

Hatton, C. J., 1984, The effect of pressure, temperature and composition on the distribution of Fe and Mg between olivine, orthopyroxene and liquid; an appraisal of the reversal in the normal fractionation trend in the Bushveld Complex: Contributions to Mineralogy and Petrology, v. 86, no. 1, p. 45-53.

Irvine, T. N., 1975, Crystallization sequences in the Muskox intrusion and other layered intrusions—II. Origin of chromitite layers and similar deposits of other magmatic ores: Geochimica et Cosmochimica Acta, v. 39, no. 6-7, p. 991-1020.

Irvine, T.N., 1977, Origin of chromitite layers in the Muskox intrusion and other stratiform intrusions: A new interpretation: Geology, v. 5, p. 273-277.

Kinnaird, J. A., 2005, The Bushveld large igneous province: Review Paper, The University of the Witwatersrand, Johannesburg, South Africa, 39pp.

Kinnaird, J. A., Kruger, F. J., Nex, P. A. M., and Cawthorn, R. G., 2002a, Chromitite formation—a key to understanding processes of platinum enrichment: Applied Earth Science: Transactions of the Institutions of Mining and Metallurgy: Section B, v. 111, no. 1, p. 23-35.

Kinnaird, J. A., Kruger, F. J., Nex, P. A. M., and Cawthorn, R. G., 2002b, Chromitites of the Bushveld Complex - Processes of formation and PGE enrichment. Economic Geology Reasearch Institute (EGRI), Information Circular, 369, 33pp

Kleeman, G. J., and Twist, D., 1989, The compositionally-zoned sheet-like granite pluton of the Bushveld Complex: Evidence bearing on the nature of A-type magmatism.: Journal of Petrology, v. 30, no. 6, p. 1383-1414.

Kruger, F. J., 1994, The Sr isotopic stratigraphy of the Western Bushveld Complex: South African Journal of Geology, v. 97, p. 393-398.

Latypov, R., Chistyakova, S., Page, A., and Hornsey, R., 2015, Field Evidence for the In Situ Crystallization of the Merensky Reef: Journal of Petrology, p. egv023.

Latypov, R. M., Chistyakova, S. Yu., Barnes, S. J. & Hunt, M., 2017, Origin of platinum deposits in layered intrusions by in situ crystallization: evidence from undercutting Merensky Reef of the Bushveld Complex. Journal of Petrology (in press).

Letts, S., Torsvik, T. H., Webb, S. J., and Ashwal, L. D., 2009, Palaeomagnetism of the 2054 Ma Bushveld Complex (South Africa): implications for emplacement and cooling: Geophysical Journal International, v. 179, no. 2, p. 850-872.

Lipin, B. R., 1992, Pressure Increases, the Formation of Chromite Seams, and the Development of the Ultramafic Series in the Stillwater Complex, Montana: Journal of petrology, v. 34, no. 5, p. 995-976.

Maier, W., and Bowen, M., 1996, The UG2-Merensky reef interval of the Bushveld Complex northwest of Pretoria: Mineralium Deposita, v. 31, no. 5, p. 386-393.

Maier, W. D., Barnes, S.-J., and Groves, D., 2013, The Bushveld Complex, South Africa: formation of platinum–palladium, chrome-and vanadium-rich layers via hydrodynamic sorting of a mobilized cumulate slurry in a large, relatively slowly cooling, subsiding magma chamber: Mineralium Deposita, v. 48, no. 1, p. 1-56.

Manoochehri, S., and Schmidt, M. W., 2014, Settling and compaction of chromite cumulates employing a centifuging piston cylinder and application to layered mafic intrusions: Contributions to Mineral and Petrology, v. 168, p. 1091.

Marsh, B., 2004, A magmatic mush column rosetta stone: the McMurdo Dry Valleys of Antarctica: Eos, Transactions American Geophysical Union, v. 85, no. 47, p. 497-502.

McDonald, J. A., 1965, Liquid immiscibility as one factor in chromitite seam formation in the Bushveld igneous complex: Economic Geology, v. 60, no. 8, p. 1674-1685.

McDonald, J.A., 1967, Evolution of Part of the Lower Critical Zone, Farm Ruighoek, Western Bushveld: Journal of Petrology, v. 8, no. 2, p. 165-209.

Mitchell, A., A., and Scoon, R., N., 2007, The Merensky Reef at Winnaarshoek., eastern Bushveld Complex: a primary magmatic hypothesis based on a wide reef facies: Economic Geology, V. 102, no. 5, p. 971-1009.

Mondal, K. S., and Mathez, A. E., 2007, Origin of the UG2 chromitite layer, Bushveld Complex: Journal of Petrology, v. 48, no. 3, p. 495-510.

Mungall, J., 2002, A model for co-precipitation of platinum-group metals with chromite from silicate melts., Abstr. 9th Internat. Platinum Symp. July: Stillwater, USA.

Naldrett, A., Kinnaird, J., Wilson, A., Yudovskaya, M., McQuade, S., Chunnett, G., and Stanley, C., 2009, Chromite composition and PGE content of Bushveld chromitites: Part 1–the Lower and Middle Groups: Applied Earth Science: Transactions of the Institutions of Mining and Metallurgy: Section B, v. 118, no. 3-4, p. 131-161.

Naldrett, A., Wilson, A., Kinnaird, J., Yudovskaya, M., and Chunnett, G., 2012, The origin of chromitites and related PGE mineralization in the Bushveld Complex: new mineralogical and petrological constraints: Mineralium Deposita, v. 47, no. 3, p. 209-232.

Nex, P., 2004, Formation of bifurcating chromitite layers of the UG1 in the Bushveld Igneous Complex, an analogy with sand volcanoes: Journal of the Geological Society, v. 161, no. 6, p. 903-909.

Nex, P. A. M., Kinnaird, J. A., Ingle, L. J., Van Der Vyver, B. A., and Cawthorn, R. G., 1998, A New Stratigraphy for the Main Zone of the Bushveld Complex, in the Rustenburg Area.: South African Journal of Geology, v. 101, no. 3, p. 215-223.

Nicholson, D., and Mathez, E., 1991, Petrogenesis of the Merensky Reef in the Rustenburg section of the Bushveld Complex: Contributions to Mineralogy and Petrology, v. 107, no. 3, p. 293-309.

O'Driscoll, B., Butcher, A. R., and Latypov, R., 2014, New insights into precious metal enrichment on the Isle of Rum, Scotland: Geology Today, v. 30, no. 4, p. 134-141.

O'Driscoll, B., Emeleus, C. H., Donaldson, C. H., and Daly, J. S., 2010, Cr-spinel seam petrogenesis in the Rum Layered Suite, NW Scotland: cumulate assimilation and in situ crystallization in a deforming crystal mush: Journal of Petrology, v. 51, no. 6, p. 1171-1201.

Roeder, P. L., and Reynolds, I., 1991, Crystallization of Chromite and Chromium Solubility in Basaltic Melts: Journal of Petrology, v. 32, no. 5, p. 909-934.

Scoates, J.S., and Friedman, R.M., 2008, Precise age of the platiniferous Merensky reef, Bushveld Complex, South Africa, by the U-Pb Zircon chemical abrasion ID-TIMS technique: Economic Geology, v. 103, p. 465-471.

Scoon, R. N., and Teigler, B., 1994, Platinum-Group Element Mineralization in the Critical Zone of the Western Bushveld Complex: I. Sulfide Poor-Chromitite below the UG-2: Economic Geology, v. 89, p. 1094-1121.

Sharpe, M., 1981, The chronology of magma influxes to the eastern compartment of the Bushveld Complex as exemplified by its marginal border groups: Journal of the Geological Society, v. 138, no. 3, p. 307-326.

South African Committee for Stratigraphy, S., 1980, Stratigraphy of South Africa Part 1 (Comp. L. E. Kent). Lithostratigraphy of the Republic of South Africa, South West Africa/Namibia, and the Republics of Bophuthatswana, Transkei and Venda: Handb. Geol. Surv. S. Afr.

Spandler, C., Mavrogenes, J., and Arculus, R., 2005, Origin of chromitites in layered intrusions: Evidence from chromite-hosted melt inclusions from the Stillwater Complex: Geology, v. 33, no. 11, p. 893-896.

Teigler, B., 1990, Platinum group element distribution in the lower and middle group chromitites in the western Bushveld Complex: Mineralogy and Petrology, v. 42, no. 1-4, p. 165-179.

Teigler, B., 1999, Chromite chemistry and platinum-group element distribution of the LG6 Chromitite: South African Journal of Geology, v. 102, no. 3.

Turner, J. S., and Campbell, I. H., 1986, Convection and mixing in magma chambers: Earth-Science Reviews, v. 23, no. 4, p. 255-352.

Viljoen, M. J., and Scoon, R. N., 1985, The distribution and main geologic features of discordant bodies of iron-rich ultramafic pegmatite in the Bushveld Complex: Economic Geology, v. 80, no. 4, p. 1109-1128.

Walraven, F., 1997, Geochronology of the Rooiberg Group, Transvaal Supergroup, South Africa, Economic Geology Research Unit, University of the Witwatersrand, v. 316.

Walraven, F., and Hattingh, E., 1993, Geochronology of the Nebo Granite, Bushveld Complex: South African Journal of Geology, v. 96, p. 31-41.

Appendices

Appendix A

Whole rock geochemistry for borehole 13R-3

ELEMENTS	SiO2	Al2O3	TiO2	Fe2O3(T)	MgO	CaO	Na2O
UNITS	%	%	%	%	%	%	%
DETECTION	0.01	0.01	0.01	0.01	0.01	0.01	0.01
METHOD	FB1/RF	FB1/RF	FB1/RF	FB1/RF	FB1/RF	FB1/RF	FB1/RF
13R-3/150.88-151	51.53	4.12	0.17	12.71	25.77	2.75	0.36
13R-3/152.09-152.19	51.52	3.97	0.14	12.64	25.83	2.58	0.31
13R-3/152.68A	46.34	4.53	0.21	14.58	24.97	2.13	0.25
13R-3/152.68C	24.79	9.18	0.41	21.42	18.19	1.12	0.12
13R-3/152.68D	18.98	10.51	0.46	22.88	16.7	0.77	0.07
13R-3/152.80A	2.22	14.6	0.64	28.53	9.99	0.38	0.06
13R-3/152.80B	1.45	14.47	0.63	28.59	10.21	0.1	0.02
13R-3/152.80C	7.19	13.42	0.59	26.35	12.17	0.39	0.08
13R-3/152.80D	1.56	14.94	0.64	28.98	9.97	0.31	0.05
13R-3/152.80E	4.07	14.42	0.61	27.7	10.57	0.48	0.06
13R-3/152.95A	17.18	11.31	0.49	24.02	15.51	0.72	0.12
13R-3/152.95E	54.46	1.29	0.12	12.21	29.3	2.02	0.1
13R-3/153.38-153.48	54.44	2.01	0.11	12.01	28.73	2.14	0.15
13R-3/154-154.10	54.56	1.87	0.11	11.77	28.62	2.01	0.18
13R-3/155.92-156	54.98	1.79	0.1	11.98	28.84	1.9	0.14
13R-3/157-157.10	54.7	1.91	0.11	11.9	28.86	1.94	0.16
13R-3/160.70-160.78	54.74	1.72	0.1	12.02	29.15	1.8	0.13
13R-3/163.58-163.67	54.27	1.71	0.09	12.16	28.86	1.78	0.12
13R-3/164.83-165	54.8	1.7	0.09	12.33	29.01	1.76	0.12
13R-3/166.10-166.27	54.185	1.76	0.1	12.185	28.97	1.71	0.12
13R-3/166.78-166.85	52.59	2.36	0.12	12.88	28.06	1.79	0.16
13R-3/167.10F	45.06	5.15	0.21	14.47	24.05	1.99	0.31
13R-3/167.10H	32.01	7.99	0.34	18.82	20.15	1.42	0.21
13R-3/167.34B	29.36	8.12	0.33	19.33	19.73	0.98	0.14
13R-3/167.34D	31.2	7.7	0.32	18.03	20.32	1.06	0.16
13R-3/167.46A	1.51	14.79	0.6	28.56	10.48	0.17	0.01
13R-3/167.46B	0.96	15	0.6	28.7	10.25	0.19	0
13R-3/167.46D1	0.93	14.79	0.6	28.51	10.25	0.22	0
13R-3/167.46E	1.075	14.88	0.6	28.43	10.31	0.25	0
13R-3/167.60B	1.85	14.59	0.58	28.32	10.41	0.19	0
13R-3/167.70A	1.48	14.66	0.59	28.32	10.48	0.17	0.05
13R-3/167.70C	1.65	14.56	0.59	28.09	10.43	0.22	0.04
13R-3/167.80B	0.82	14.75	0.59	28.55	10.12	0.17	0
13R-3/167.80D	0.66	14.94	0.6	28.66	10.2	0.2	0.04
13R-3/167.80F	1.1	14.84	0.59	28.63	10.34	0.19	0.02
13R-3/167.80H	1.56	14.82	0.59	28.52	10.21	0.28	0.05
13R-3/168.02B	2.2	14.54	0.59	28.31	10.33	0.3	0.01
13R-3/168.02D	2.33	14.38	0.59	28.02	10.42	0.36	0
13R-3/168.02F	1.6	14.74	0.6	28.32	10.09	0.34	0.02
13R-3/168.02G	1.93	14.68	0.6	28.78	10.11	0.33	0.03
13R-3/168.24A	37.59	5.87	0.28	17.07	22.97	1.66	0.11
13R-3/168.24D	47.81	3.06	0.2	14.36	26.19	2.05	0.15
13R-3/168.56-168-68	37.95	6.33	0.31	17.43	22.64	1.79	0.14
13R-3/168.93-169	53.26	2.88	0.14	12.56	27.14	2.49	0.2
13R-3/171.90-172	53.57	3.94	0.14	11.84	26.22	2.8	0.42

ELEMENTS	K2O	Cr2O3	P2O5	MnO	SO3	LOI	Total
UNITS	%	%	%	%	%	%	
DETECTION	0.01	0.01 or 0.0	0.002	0.01	0.01 / 0.002	0.01	
METHOD	FB1/RF	FB1/RF	FB1/RF	FB1/RF	FB1/RF	/TGA	
13R-3/150.88-151	0.03	2.65	0.009	0.22	0.02	-0.38	99.959
13R-3/152.09-152.19	0.03	3.13	0.005	0.22	0.02	-0.42	99.975
13R-3/152.68A	0.03	7.44	0.009	0.23	0.01	-0.65	100.079
13R-3/152.68C	0.02	25.66	0.003	0.22	0.01	-1.2	99.943
13R-3/152.68D	0.01	30.66	0.004	0.22	0.006	-1.49	99.782
13R-3/152.80A	0.02	44.92	0.007	0.22	0.007	-1.91	99.686
13R-3/152.80B	0.05	45.31	0.005	0.22	0.008	-1.95	99.11
13R-3/152.80C	0.05	40.11	0.009	0.22	0.011	-1.74	98.847
13R-3/152.80D	0.02	45.44	0.007	0.22	0.005	-1.98	100.163
13R-3/152.80E	0.02	42.82	0.006	0.21	0.014	-1.75	99.23
13R-3/152.95A	0.04	31.43	0.005	0.23	0.02	-0.98	100.095
13R-3/152.95E	0.02	0.79	0.005	0.23	0.09	-0.21	100.425
13R-3/153.38-153.48	0.01	0.77	0.006	0.23	0.01	-0.45	100.166
13R-3/154-154.10	0.01	0.55	0.01	0.23	0.01	-0.46	99.47
13R-3/155.92-156	0.02	0.61	0.004	0.23	0	-0.49	100.104
13R-3/157-157.10	0.02	0.72	0.007	0.23	0	-0.31	100.247
13R-3/160.70-160.78	0.03	0.66	0.008	0.23	0	-0.51	100.078
13R-3/163.58-163.67	0.02	0.65	0.007	0.23	0	-0.48	99.417
13R-3/164.83-165	0.02	0.79	0.004	0.24	0	-0.56	100.304
13R-3/166.10-166.27	0.025	0.98	0.009	0.23	0	-0.24	100.029
13R-3/166.78-166.85	0.02	2.27	0.007	0.23	0	-0.38	100.107
13R-3/167.10F	0.06	8.00	0.01	0.22	0.01	0.43	99.97
13R-3/167.10H	0.03	19.02	0.01	0.22	0.01	-0.28	99.95
13R-3/167.34B	0.03	20.74	0.005	0.21	0.02	0.34	99.335
13R-3/167.34D	0.04	18.87	0.005	0.18	0.03	1.69	99.605
13R-3/167.46A	0	45.15	0.004	0.21	0.002	-1.75	99.738
13R-3/167.46B	0	45.76	0.005	0.22	0.003	-1.76	99.923
13R-3/167.46D1	0.01	45.49	0.006	0.21	0.006	-2	99.022
13R-3/167.46E	0	45.37	0	0.21	0	-1.695	99.434
13R-3/167.60B	0.02	44.73	0.006	0.22	0.004	-1.39	99.533
13R-3/167.70A	0	45.04	0.007	0.22	0.005	-1.54	99.486
13R-3/167.70C	0.01	44.90	0.007	0.21	0.009	-1.54	99.174
13R-3/167.80B	0.01	45.82	0.006	0.21	0.002	-1.79	99.259
13R-3/167.80D	0.01	46.02	0.004	0.21	0.008	-1.88	99.668
13R-3/167.80F	0.01	45.71	0.005	0.21	0.008	-1.89	99.76
13R-3/167.80H	0	45.34	0.008	0.22	0.007	-1.94	99.661
13R-3/168.02B	0.02	44.80	0.008	0.22	0.011	-1.73	99.611
13R-3/168.02D	0.01	44.53	0	0.21	0.01	-1.63	99.225
13R-3/168.02F	0.01	45.10	0.007	0.22	0.008	-1.73	99.321
13R-3/168.02G	0.02	44.83	0.004	0.22	0.004	-1.79	99.745
13R-3/168.24A	0.02	13.82	0.007	0.23	0.01	-0.42	99.217
13R-3/168.24D	0.03	5.81	0.022	0.23	0.01	-0.15	99.772
13R-3/168.56-168-68	0	14.00	0.003	0.22	0.02	-0.81	100.023
13R-3/168.93-169	0.05	1.33	0.011	0.23	0.01	-0.13	100.171
13R-3/171.90-172	0.04	1.25	0.013	0.22	0.02	-0.36	100.113

ELEMENTS	Au	Ag	Ba	Co	Cu	La	Ni
UNITS	ppb	ppm	ppm	ppm	ppm	ppm	ppm
DETECTION	2	0.5	1 or 2	1	5	0.1	5
METHOD	NS25/MS	4A/MS	4A/MS	4A/MS	4A/OE	4A/MS	4A/OE
13R-3/150.88-151			17	105	11	0.9	530
13R-3/152.09-152.19			19	108	13	0.8	548
13R-3/152.68A			15	125	11	0.7	616
13R-3/152.68C			9	189	6	0.5	731
13R-3/152.68D			5	212	9	0.5	795
13R-3/152.80A	2	5.6	10	255	8	0.9	791
13R-3/152.80B	2	1.2	16	258	8	0.2	905
13R-3/152.80C			10	243	6	0.5	815
13R-3/152.80D		1.9	6	280	13	0.7	900
13R-3/152.80E	6	0.8	10	275	16	0.7	897
13R-3/152.95A			16	167	7	0.4	620
13R-3/152.95E			5	105		0.4	578
13R-3/153.38-153.48			6	105	11	0.4	569
13R-3/154-154.10			8	102	8	0.6	562
13R-3/155.92-156			8	103	6	0.5	574
13R-3/157-157.10			9	102	6	0.6	547
13R-3/160.70-160.78			9	104		0.5	549
13R-3/163.58-163.67			7	101	6	0.4	544
13R-3/164.83-165	3		5	104		0.3	554
13R-3/166.10-166.27			7	102.5		0.5	552.5
13R-3/166.78-166.85			13	108	8	0.6	525
13R-3/167.10F	2		46	121	11	0.9	509
13R-3/167.10H			30	140		0.9	536
13R-3/167.34B	123		32	145		0.6	528
13R-3/167.34D			19	163		0.7	616
13R-3/167.46A	5			277	59	0.2	908
13R-3/167.46B				260	11		794
13R-3/167.46D1			5	269	7	0.2	847
13R-3/167.46E	4	0.5	3	257	6	0.15	854
13R-3/167.60B			5	267	10		833
13R-3/167.70A	3	0.8	2	262	8	0.3	890
13R-3/167.70C	2		8	269		0.3	867
13R-3/167.80B		0.7	3	280	20	0.3	977
13R-3/167.80D			3	259	6	0.3	854
13R-3/167.80F			6	283	8	0.1	971
13R-3/167.80H	2		9	275	13	0.2	920
13R-3/168.02B			25	270	10	0.2	930
13R-3/168.02D			4	258	10	0.3	863
13R-3/168.02F		0.6	7	278	9	0.2	901
13R-3/168.02G			14	271	10	0.3	884
13R-3/168.24A	2		5	153	7	0.4	659
13R-3/168.24D			7	115	9	0.7	602
13R-3/168.56-168-68			4	154	12	0.3	640
13R-3/168.93-169			14	103	5	0.7	523
13R-3/171.90-172			24	98	15	1.3	509

ELEMENTS	S	SO3	S	Sr	V	Y	Zn	Zr
UNITS	ppm	%	ppm	ppm	ppm	ppm	ppm	ppm
DETECTION	50	0.01 or 0.002		0.5	5	0.5	5	1
METHOD	4A/OE	FB1/RF	Calc	4A/MS	4A/OE	4A/MS	4A/OE	4A/MS
13R-3/150.88-151	87	0.02	80.090	37.7	238	2.3	97	5
13R-3/152.09-152.19	76	0.02	80.090	33.9	246	2.4	95	4
13R-3/152.68A	61	0.01	40.045	22.2	477	1.9	129	5
13R-3/152.68C		0.01	40.045	9	1224	1.1	280	3
13R-3/152.68D		0.006	24.027	5.8	1432	0.7	402	5
13R-3/152.80A		0.007	28.031	10.1	1760	0.7	502	4
13R-3/152.80B		0.008	32.036	2.3	2028		582	3
13R-3/152.80C		0.011	44.049	5.4	1667	1.1	486	3
13R-3/152.80D		0.005	20.022	5.9	1966		584	7
13R-3/152.80E	64	0.014	56.063	9.4	1876		556	5
13R-3/152.95A	60	0.02	80.090	7.7	1065	1.1	257	5
13R-3/152.95E	396	0.09	360.404	2.1	120	2.1	83	4
13R-3/153.38-153.48	71	0.01	40.045	12.7	125	1.9	78	4
13R-3/154-154.10	59	0.01	40.045	11	101	1.9	73	4
13R-3/155.92-156			0.000	7.4	106	1.6	75	4
13R-3/157-157.10			0.000	9.5	104	1.7	76	4
13R-3/160.70-160.78			0.000	4.8	93	1.6	72	4
13R-3/163.58-163.67			0.000	5.9	95	1.5	73	3
13R-3/164.83-165			0.000	5.8	104	1.4	76	3
13R-3/166.10-166.27			0.000	4.4	111.5	1.45	75.5	3
13R-3/166.78-166.85			0.000	10.1	170	1.5	87	5
13R-3/167.10F		0.01	40.045	33.3	402	1.6	133	4
13R-3/167.10H		0.01	40.045	21.4	717	1.5	205	4
13R-3/167.34B		0.02	80.090	11.5	789	1	204	4
13R-3/167.34D	72	0.03	120.135	10.8	854	1.4	210	5
13R-3/167.46A	206	0.002	8.009		1742		576	2
13R-3/167.46B		0.003	12.013	1.1	1675		559	2
13R-3/167.46D1		0.006	24.027	1.1	1764		592	4
13R-3/167.46E		0.005	20.022	1.2	1755		610.5	2
13R-3/167.60B		0.004	16.018	0.8	1802		594	1
13R-3/167.70A		0.005	20.022	1.2	1934	0.9	627	2
13R-3/167.70C		0.009	36.040	1.1	2012		601	2
13R-3/167.80B		0.002	8.009	1.6	2299		658	2
13R-3/167.80D		0.008	32.036	1.5	2147		584	3
13R-3/167.80F		0.008	32.036	0.8	2373	0.6	638	3
13R-3/167.80H		0.007	28.031	9.4	2347		604	2
13R-3/168.02B		0.011	44.049	12.2	2334		601	2
13R-3/168.02D		0.01	40.045	5.1	2201		570	3
13R-3/168.02F		0.008	32.036	2.8	2236		591	2
13R-3/168.02G		0.004	16.018	5.5	2170	0.7	583	3
13R-3/168.24A		0.01	40.045	9.5	840	2.8	195	3
13R-3/168.24D	68	0.01	40.045	7.8	359	2.6	114	6
13R-3/168.56-168-68	61	0.02	80.090	15.5	777	1.3	195	2
13R-3/168.93-169	73	0.01	40.045	25.7	161	2.6	80	5
13R-3/171.90-172	85	0.02	80.090	45.5	155	2.4	78	7

ELEMENTS	Ir	Os	Pd	Pt	Rh	Ru	IPGE	PPGE	Total PGE	Pt*/Ru*
UNITS	ppb	ppb	ppb	ppb	ppb	ppb	ppb	ppb	ppb	
DETECTION	1	1	1	1	1	1	3	3	6	
METHOD	NS25/MS						NS25/MS		NS25/MS	
13R-3/150.88-151							0	0	0	0.00
13R-3/152.09-152.19							0	0	0	0.00
13R-3/152.68A							0	0	0	0.00
13R-3/152.68C							0	0	0	0.00
13R-3/152.68D	72	60	117	366	104	402	534	587	1121	1.10
13R-3/152.80A	101	86	174	499	145	558	745	818	1563	1.10
13R-3/152.80B	104	109	179	471	147	571	784	797	1581	1.02
13R-3/152.80C	118	100	160	458	121	683	901	739	1640	0.82
13R-3/152.80D	133	111	215	627	159	732	976	1001	1977	1.03
13R-3/152.80E	142	117	241	661	161	574	833	1063	1896	1.28
13R-3/152.95A							0	0	0	0.00
13R-3/152.95E							0	0	0	0.00
13R-3/153.38-153.48							0	0	0	0.00
13R-3/154-154.10							0	0	0	0.00
13R-3/155.92-156							0	0	0	0.00
13R-3/157-157.10							0	0	0	0.00
13R-3/160.70-160.78							0	0	0	0.00
13R-3/163.58-163.67							0	0	0	0.00
13R-3/164.83-165	2		12	24	7	8	10	43	53	4.30
13R-3/166.10-166.27							0	0	0	0.00
13R-3/166.78-166.85							0	0	0	0.00
13R-3/167.10F	14	11	30	60	22	90	115	112	227	0.97
13R-3/167.10H	36	31	63	169	62	245	312	294	606	0.94
13R-3/167.34B	42	43	72	193	66	337	422	331	753	0.78
13R-3/167.34D	33	28	50	141	50	239	300	241	541	0.80
13R-3/167.46A	69	86	72	245	95	510	665	412	1077	0.62
13R-3/167.46B	80	80	61	213	89	604	764	363	1127	0.48
13R-3/167.46D1	80	82	64	232	92	580	742	388	1130	0.52
13R-3/167.46E	73	87	80	297	118	501	661	495	1156	0.75
13R-3/167.60B	92	81	108	462	148	605	778	718	1496	0.92
13R-3/167.70A	60	61	70	236	90	345	466	396	862	0.85
13R-3/167.70C	73	62	69	233	97	465	600	399	999	0.67
13R-3/167.80B	74	60	65	238	101	363	497	404	901	0.81
13R-3/167.80D	83	66	63	203	88	399	548	354	902	0.65
13R-3/167.80F	87	97	98	330	133	567	751	561	1312	0.75
13R-3/167.80H	70	73	90	329	127	426	569	546	1115	0.96
13R-3/168.02B	66	56	77	237	96	424	546	410	956	0.75
13R-3/168.02D	67	57	75	200	86	434	558	361	919	0.65
13R-3/168.02F	66	54	88	262	104	409	529	454	983	0.86
13R-3/168.02G	71	66	127	409	150	408	545	686	1231	1.26
13R-3/168.24A	24	14	32	132	48	100	138	212	350	1.54
13R-3/168.24D	10	6	21	58	20	53	69	99	168	1.43
13R-3/168.56-168-68							0	0	0	0.00
13R-3/168.93-169							0	0	0	0.00
13R-3/171.90-172							0	0	0	0.00

Appendix B

Whole rock geochemistry for borehole 13R-9

ELEMENTS	SiO2	Al2O3	TiO2	Fe2O3(T)	MgO	CaO	Na2O
UNITS	%	%	%	%	%	%	%
DETECTION	0.01	0.01	0.01	0.01	0.01	0.01	0.01
METHOD	FB1/RF	FB1/RF	FB1/RF	FB1/RF	FB1/RF	FB1/RF	FB1/RF
13R-9/199.46A	39.48	0.61	0.07	18.96	31.9	0.6	0.08
13R-9/199.60A	38.14	5.5	0.36	18.04	24.17	1.13	0.1
13R-9/199.60C	16.34	12.02	0.69	21.23	16.92	0.79	0.06
13R-9/199.60D	2.2	16.4	0.97	25.2	10.25	0.11	0
13R-9/199.60F	2.75	16.93	0.93	24.6	10.83	0.17	0.04
13R-9/199.82B	2.29	17.3	0.93	24.74	10.51	0.09	0.03
13R-9/199.82D	2.8	16.97	0.93	24.62	10.66	0.09	0.02
13R-9/199.82F	5.65	15.95	0.88	24.77	11.23	0.17	0.04
13R-9/199.82H	8.49	13.22	1.07	27.87	10.36	0.35	0.04
13R-9/199.82J	5.74	13.5	1.01	28.7	9.47	0.36	0.06
13R-9/200.15B	52.64	1.67	0.23	14.65	25.72	1.77	0.18
13R-9/200.15C	52.76	1.42	0.19	15.43	25.39	1.79	0.17
13R-9/200.15E	48.87	1.36	0.2	15.61	24.65	2.82	0.16
13R-9/201.29-201.41	54.16	1.45	0.19	15.34	26.44	1.89	0.15
13R-9/201.95-202.10	53.21	1.62	0.25	16.16	25.71	2.13	0.17
13R-9/203.30-203.43	54.04	1.33	0.16	14.45	28.03	1.53	0.09
13R-9/204.40-204.52	53.88	1.31	0.18	15.28	27.07	1.54	0.09
13R-9/205.42-205.52	53.895	1.71	0.205	13.605	27.255	2.555	0.165
13R-9/206.15-206.29	52.61	1.54	0.18	15.11	28.23	1.49	0.13
13R-9/208.22-208.34	54.03	1.5	0.19	14.44	27.46	1.99	0.13
13R-9/209.79-209.93	52.57	1.86	0.26	18.73	23.04	2.1	0.27
13R-9/211.09-211.26	53.23	1.74	0.16	13.55	27.5	1.79	0.14
13R-9/211.87D	52.15	1.72	0.12	13.26	29.56	1.85	0.08
13R-9/212.10A	53.37	1.49	0.14	12.92	29.01	1.8	0.09
13R-9/212.68A	15.37	10.98	0.55	21.5	19.73	0.28	0.03
13R-9/212.68C	34.23	2.84	0.16	15.34	32.88	0.65	0.07
13R-9/212.80B	29.99	4.16	0.23	16.69	29.74	0.26	0.07
13R-9/212.84B	20.02	9.4	0.46	20.01	19.51	0.51	0.03
13R-9/212.90B	29.24	6.88	0.35	17.3	23.04	1.07	0.06
13R-9/212.90D	24.21	7.61	0.37	17.64	21.79	0.7	0.06
13R-9/212.90E	3.42	15.05	0.67	23.46	11.41	0.19	0
13R-9/212.90G	14.11	10.26	0.49	20.27	16.43	1.12	0.03
13R-9/212.90I	1.83	15.01	0.68	23.08	10.65	0.52	0.01
13R-9/212.90K	1.87	14.84	0.68	23.21	10.89	0.15	0
13R-9/212.90M	2.07	13.89	0.64	21.86	10.57	2.71	0.02
13R-9/213.27B	2.02	14.25	0.68	22.83	10.83	0.74	0
13R-9/213.27D	3.46	13.76	0.62	22.01	11.14	2.21	0
13R-9/213.27F	1.92	14.74	0.68	23.14	10.94	0.17	0.02
13R-9/213.27H	1.83	14.73	0.7	22.83	10.95	0.23	0.02
13R-9/213.50B	1.94	14.39	0.7	22.9	10.81	0.42	0.03
13R-9/213.50D	4.01	13.67	0.9	25.29	9.42	0.45	0.03
13R-9/213.63A	10.58	13.51	0.81	23.02	10.25	1.36	0.11
13R-9/213.63C	32.12	5.9	0.36	17.34	22.22	1.12	0.13
13R-9/213.63D	37.8	4.53	0.26	15.98	26.54	0.82	0.05
13R-9/213.63E	30.56	5.57	0.27	17.95	26.95	0.4	0.09
13R-9/213.63G	36.11	1.86	0.09	17.17	32.47	0.49	0.08
13R-9/213.97A	36.74	0.88	0.08	14.14	34.25	0.46	0.07
13R-9/214.24A	53.28	1.25	0.17	14.19	28.42	1.45	0.09
13R-9/214.24G	51.45	1.38	0.18	14.31	27.91	1.48	0.1
13R-9/214.69-214.80	51.83	1.54	0.19	14.48	28.53	1.69	0.07
13R-9/215.20-215.30	53.36	1.47	0.19	13.64	28.09	1.88	0.1
13R-9/215.65-215.79	53.465	1.405	0.17	13.625	28.895	1.55	0.09

ELEMENTS	K2O	Cr2O3	P2O5	MnO	SO3	LOI	Total
UNITS	%	%	%	%	%	%	
DETECTION	0.01	0.01 or 0.005	0.002	0.01	0.01 / 0.002	0.01	
METHOD	FB1/RF	FB1/RF	FB1/RF	FB1/RF	FB1/RF	/TGA	
13R-9/199.46A	0.01	0.14	0.008	0.19	0.06	7.07	99.178
13R-9/199.60A	0.03	11.27	0.009	0.26	0.12	0.98	100.109
13R-9/199.60C	0.02	30.33	0.005	0.23	0.13	1.14	99.905
13R-9/199.60D	0	44.74	0.004	0.24	0.019	-1.62	98.517
13R-9/199.60F	0	44.46	0.003	0.23	0.042	-1.44	99.543
13R-9/199.82B	0	45.10	0.003	0.23	0.008	-1.82	99.41
13R-9/199.82D	0	44.16	0.006	0.22	0.015	-1.7	98.786
13R-9/199.82F	0	41.66	0.006	0.24	0.019	-1.36	99.252
13R-9/199.82H	0.01	38.89	0.005	0.27	0.021	-1.44	99.159
13R-9/199.82J	0.01	40.83	0.003	0.3	0.014	-1.31	98.687
13R-9/200.15B	0.08	1.11	0.025	0.24	0.023	1.81	100.149
13R-9/200.15C	0.08	0.45	0.004	0.27	0.01	1.28	99.244
13R-9/200.15E	0.08	0.78	0.009	0.29	0.06	5.26	100.149
13R-9/201.29-201.41	0.07	0.42	0.006	0.27	0.02	-0.16	100.246
13R-9/201.95-202.10	0.12	0.49	0.013	0.28	0.01	0.09	100.253
13R-9/203.30-203.43	0.02	0.46	0.005	0.25	0.02	-0.23	100.155
13R-9/204.40-204.52	0.03	0.66	0.003	0.27	0	-0.5	99.813
13R-9/205.42-205.52	0.06	0.47	0.024	0.235	0.365	-0.225	100.314
13R-9/206.15-206.29	0.06	0.42	0.014	0.25	0.05	-0.3	99.784
13R-9/208.22-208.34	0.03	0.47	0.012	0.26	0.03	-0.21	100.332
13R-9/209.79-209.93	0.26	0.53	0.061	0.31	0.01	-0.48	99.521
13R-9/211.09-211.26	0.05	0.78	0.009	0.23	0.04	0.69	99.909
13R-9/211.87D	0.01	1.04	0.006	0.22	0.02	0.05	100.086
13R-9/212.10A	0	0.90	0.006	0.23	0.02	0.3	100.276
13R-9/212.68A	0	27.13	0.003	0.18	0.14	3.05	98.943
13R-9/212.68C	0	6.30	0.01	0.12	0.32	6.87	99.79
13R-9/212.80B	0	9.62	0.009	0.12	0.37	7.94	99.199
13R-9/212.84B	0.01	27.96	0.009	0.22	0.09	1.08	99.309
13R-9/212.90B	0.02	19.21	0.008	0.22	0.11	1.64	99.148
13R-9/212.90D	0.02	21.28	0.004	0.26	0.25	4.92	99.114
13R-9/212.90E	0	46.04	0.004	0.22	0.102	-0.81	99.751
13R-9/212.90G	0.01	33.78	0	0.25	0.172	2.53	99.453
13R-9/212.90I		48.41	0.003	0.22	0.087	-0.89	99.607
13R-9/212.90K		48.66		0.22	0.109	-1.22	99.406
13R-9/212.90M		46.42	0.006	0.23	0.083	1.12	99.623
13R-9/213.27B		48.31	0.004	0.23	0.097	-0.63	99.365
13R-9/213.27D		44.61	0.004	0.33	0.071	1.03	99.249
13R-9/213.27F		48.80	0.004	0.22	0.083	-1.18	99.537
13R-9/213.27H		49.21	0.007	0.23	0.095	-1.04	99.796
13R-9/213.50B		49.33	0.008	0.23	0.079	-1.01	99.824
13R-9/213.50D	0.17	46.38	0.035	0.26	0.042	-1.08	99.575
13R-9/213.63A	0.67	37.01	0.201	0.31	0.037	1.08	98.951
13R-9/213.63C	0.04	15.61	0.007	0.26	0.144	4.24	99.495
13R-9/213.63D	0.05	9.29	0.011	0.23	0.129	4.04	99.731
13R-9/213.63E		12.42	0.01	0.18	0.15	4.59	99.14
13R-9/213.63G		2.68	0.007	0.1	0.24	8.28	99.577
13R-9/213.97A		1.45	0.006	0.14	0.23	10.86	99.306
13R-9/214.24A	0.01	0.85	0.005	0.24	0.04	0.24	100.235
13R-9/214.24G	0.01	1.30	0.007	0.23	0.08	0.98	99.417
13R-9/214.69-214.80		1.74	0.008	0.24	0.06	-0.29	100.088
13R-9/215.20-215.30	0.01	1.45	0.006	0.23	0.01	-0.31	100.126
13R-9/215.65-215.79		1.05	0.006	0.23	0.03	-0.325	100.186

ELEMENTS	Au	Ag	Ba	Co	Cu	La	Ni
UNITS	ppb	ppm	ppm	ppm	ppm	ppm	ppm
DETECTION	2	0.5	1 or 2	1	5	0.1	5
METHOD	NS25/MS	4A/MS	4A/MS	4A/MS	4A/OE	4A/MS	4A/OE
13R-9/199.46A	3		5	194	10	0.2	1156
13R-9/199.60A			6	167	128	0.3	723
13R-9/199.60C			2	190	39	0.6	694
13R-9/199.60D				279	23		540
13R-9/199.60F	4			288	107	0.1	599
13R-9/199.82B				238	8		526
13R-9/199.82D	13			254	10		536
13R-9/199.82F	12	0.7	4	268	12	0.2	466
13R-9/199.82H	5			281	19	0.2	557
13R-9/199.82J	3		3	292	10		553
13R-9/200.15B	4		10	85	12	1.4	548
13R-9/200.15C			12	92	17	0.7	521
13R-9/200.15E			11	94	29	0.6	513
13R-9/201.29-201.41			13	106	32	0.9	516
13R-9/201.95-202.10			40	100	14	1.5	557
13R-9/203.30-203.43			3	102	34	0.3	603
13R-9/204.40-204.52			4	103		0.6	428
13R-9/205.42-205.52		1.35	19.5	107.5	886	1.3	1540
13R-9/206.15-206.29			12	110	60	0.9	705
13R-9/208.22-208.34			9	97	30	0.8	530
13R-9/209.79-209.93			34	98	16	4.2	553
13R-9/211.09-211.26			8	97	44	0.9	531
13R-9/211.87D			3	101	12	0.2	530
13R-9/212.10A			1	97	10	0.1	501
13R-9/212.68A				193	10		990
13R-9/212.68C			1	180	104	0.2	1418
13R-9/212.80B	55			195	128	0.2	1897
13R-9/212.84B			1	179	86		747
13R-9/212.90B			1	163	93	0.1	803
13R-9/212.90D	12			138	219	0.1	959
13R-9/212.90E	8.5		2	254	26.5		667
13R-9/212.90G	7			218	130	0.2	806
13R-9/212.90I	7			249	72		619
13R-9/212.90K	2			221	109	0.3	586
13R-9/212.90M	2			236	69	0.2	553
13R-9/213.27B	2			224	117		538
13R-9/213.27D	4			236	31	0.3	547
13R-9/213.27F				247	98	0.1	606
13R-9/213.27H	4			244	97	0.1	586
13R-9/213.50B	2			262	102		574
13R-9/213.50D	2	19.9	206	264	42	2.7	512
13R-9/213.63A	4		466	213	39	5	460
13R-9/213.63C	5		12	175	100	0.5	798
13R-9/213.63D	10	1.2	24	174	58	0.5	998
13R-9/213.63E	10		1	183	53		1027
13R-9/213.63G			2	162	73	0.2	1235
13R-9/213.97A			1	205	6		1162
13R-9/214.24A			2	105	49	0.2	714
13R-9/214.24G			2	111	60	0.2	803
13R-9/214.69-214.80			1	113	104	0.1	833
13R-9/215.20-215.30			3	102	19	0.3	699
13R-9/215.65-215.79	3.5		2	106.5	52	0.15	729

ELEMENTS	S	SO3	S	Sr	V	Y	Zn	Zr
UNITS	ppm	%	ppm	ppm	ppm	ppm	ppm	ppm
DETECTION	50	0.01 or 0.002		0.5	5	0.5	5	1
METHOD	4A/OE	FB1/RF	Calc	4A/MS	4A/OE	4A/MS	4A/OE	4A/MS
13R-9/199.46A	243	0.06	240.269	6.4	68	1.1	100	2
13R-9/199.60A	544	0.12	480.538	4.7	1204	1.8	270	3
13R-9/199.60C	462	0.13	520.583	5	2354	0.9	369	2
13R-9/199.60D	53	0.019	76.085	0.6	4248		785	
13R-9/199.60F	170	0.042	168.188	0.6	4661		797	1
13R-9/199.82B		0.008	32.036		3805		650	1
13R-9/199.82D		0.015	60.067	1.2	3520		683	2
13R-9/199.82F	60	0.019	76.085	1	3183		750	3
13R-9/199.82H	69	0.021	84.094	1.4	4025	0.8	1036	3
13R-9/199.82J		0.014	56.063	1	4850	0.5	1008	2
13R-9/200.15B	67	0.023	92.103	10.6	378	2.7	103	11
13R-9/200.15C	80	0.01	40.045	9.3	281	2.9	96	6
13R-9/200.15E	286	0.06	240.269	9.3	317	3	95	6
13R-9/201.29-201.41	94	0.02	80.090	9.5	341	3.3	118	5
13R-9/201.95-202.10	58	0.01	40.045	6.5	325	5.3	126	9
13R-9/203.30-203.43	101	0.02	80.090	2.8	221	2.5	108	3
13R-9/204.40-204.52			0.000	2	283	3.5	119	4
13R-9/205.42-205.52	1583	0.365	1461.637	11.5	222	4.7	89	6
13R-9/206.15-206.29	226	0.05	200.224	9.4	183	4.6	108	6
13R-9/208.22-208.34	117	0.03	120.135	7.9	222	3.9	100	6
13R-9/209.79-209.93	71	0.01	40.045	9.3	366	7.1	142	16
13R-9/211.09-211.26	163	0.04	160.179	9.7	242	3.2	102	7
13R-9/211.87D	91	0.02	80.090	4.8	213	1.8	71	3
13R-9/212.10A	104	0.02	80.090	2	224	2.1	78	3
13R-9/212.68A	492	0.14	560.628	1	1901		328	1
13R-9/212.68C	1373	0.32	1281.435	2.6	692	0.8	120	3
13R-9/212.80B	1905	0.37	1481.659	3.1	953		178	2
13R-9/212.84B	479	0.09	360.404	2	2279	0.5	263	1
13R-9/212.90B	507	0.11	440.493	3.1	1530	0.7	220	3
13R-9/212.90D	1062	0.25	1001.121	10.8	1154	1	187	4
13R-9/212.90E	343	0.102	408.457	1.2	2321		586.5	1.5
13R-9/212.90G	651	0.172	688.771	12	1358		432	
13R-9/212.90I	311	0.087	348.390	5.6	1795		582	2
13R-9/212.90K	353	0.109	436.489	1.4	1547		528	2
13R-9/212.90M	299	0.083	332.372	12.4	1677		562	2
13R-9/213.27B	338	0.097	388.435	8	1800		543	3
13R-9/213.27D	234	0.071	284.318	12.8	1872	0.6	731	2
13R-9/213.27F	338	0.083	332.372	1.1	2101		614	2
13R-9/213.27H	348	0.095	380.426	0.5	2495		617	3
13R-9/213.50B	313	0.079	316.354	4	2843		620	3
13R-9/213.50D	168	0.042	168.188	64	2823	2.1	692	23
13R-9/213.63A	123	0.037	148.166	65.9	2456	3.5	584	4
13R-9/213.63C	559	0.144	576.646	15.3	1608	1.9	333	3
13R-9/213.63D	508	0.129	516.579	8.3	1124	1.9	264	3
13R-9/213.63E	619	0.15	600.673	2.2	1162	0.7	207	2
13R-9/213.63G	1042	0.24	961.076	7.4	325	0.8	105	2
13R-9/213.97A	1015	0.23	921.032	5.4	192	0.6	97	
13R-9/214.24A	164	0.04	160.179	2.1	247	2.6	105	3
13R-9/214.24G	332	0.08	320.359	4	314	2.5	121	2
13R-9/214.69-214.80	231	0.06	240.269	1.7	342	2.4	119	2
13R-9/215.20-215.30	71	0.01	40.045	2.1	338	2.7	114	3
13R-9/215.65-215.79	135.5	0.03	120.135	1.4	316	2.45	101.5	2.5

ELEMENTS	Ir	Os	Pd	Pt	Rh	Ru	IPGE	PPGE	Total PGE	Pt*/Ru*
UNITS	ppb	ppb	ppb	ppb	ppb	ppb	ppb	ppb	ppb	
DETECTION	1	1	1	1	1	1	3	3	6	
METHOD	NS25/MS						NS25/MS		NS25/MS	
13R-9/199.46A	3	2	14	97	8	14	19	119	138	6.26
13R-9/199.60A							0	0	0	0.00
13R-9/199.60C	70	56	190	565	94	437	563	849	1412	1.51
13R-9/199.60D	89	78	215	621	121	553	720	957	1677	1.33
13R-9/199.60F	93	80	209	451	109	608	781	769	1550	0.98
13R-9/199.82B	128	108	396	643	178	836	1072	1217	2289	1.14
13R-9/199.82D	137	116	786	717	160	862	1115	1663	2778	1.49
13R-9/199.82F	127	107	1286	917	133	763	997	2336	3333	2.34
13R-9/199.82H	70	93	434	562	87	438	601	1083	1684	1.80
13R-9/199.82J	117	76	452	1738	217	648	841	2407	3248	2.86
13R-9/200.15B	17	11	81	257	30	62	90	368	458	4.09
13R-9/200.15C	15	9	94	283	31	72	96	408	504	4.25
13R-9/200.15E							0	0	0	0.00
13R-9/201.29-201.41							0	0	0	0.00
13R-9/201.95-202.10							0	0	0	0.00
13R-9/203.30-203.43							0	0	0	0.00
13R-9/204.40-204.52	1		27	27	5	8	9	59	68	6.56
13R-9/205.42-205.52							0	0	0	0.00
13R-9/206.15-206.29							0	0	0	0.00
13R-9/208.22-208.34							0	0	0	0.00
13R-9/209.79-209.93							0	0	0	0.00
13R-9/211.09-211.26	2		49	28	6	8	10	83	93	8.30
13R-9/211.87D							0	0	0	0.00
13R-9/212.10A							0	0	0	0.00
13R-9/212.68A							0	0	0	0.00
13R-9/212.68C							0	0	0	0.00
13R-9/212.80B	28	29	162	302	52	215	272	516	788	1.90
13R-9/212.84B							0	0	0	0.00
13R-9/212.90B							0	0	0	0.00
13R-9/212.90D	40	38	120	124	50	331	409	294	703	0.72
13R-9/212.90E	98	101	62	357	125	759	958	544	1502	0.57
13R-9/212.90G	70	64	44	262	101	481	615	407	1022	0.66
13R-9/212.90I	93	99	87	241	95	709	901	423	1324	0.47
13R-9/212.90K	95	91	55	287	114	723	909	456	1365	0.50
13R-9/212.90M	83	71	67	314	132	563	717	513	1230	0.72
13R-9/213.27B	87	74	47	142	88	560	721	277	998	0.38
13R-9/213.27D	73	82	40	210	93	589	744	343	1087	0.46
13R-9/213.27F	93	91	59	259	111	710	894	429	1323	0.48
13R-9/213.27H	87	87	106	345	135	552	726	586	1312	0.81
13R-9/213.50B	78	76	109	194	103	496	650	406	1056	0.62
13R-9/213.50D	73	52	95	113	96	452	577	304	881	0.53
13R-9/213.63A	60	58	77	132	91	420	538	300	838	0.56
13R-9/213.63C	102	71	289	2612	274	423	596	3175	3771	5.33
13R-9/213.63D	23	24	85	234	31	130	177	350	527	1.98
13R-9/213.63E	23	16	64	208	37	116	155	309	464	1.99
13R-9/213.63G							0	0	0	0.00
13R-9/213.97A							0	0	0	0.00
13R-9/214.24A							0	0	0	0.00
13R-9/214.24G							0	0	0	0.00
13R-9/214.69-214.80							0	0	0	0.00
13R-9/215.20-215.30							0	0	0	0.00
13R-9/215.65-215.79	4	2	11	26.5	8.5	15	21	46	67	2.19

Appendix C

Whole rock means and standard deviation calculations for boreholes 13R-3 and 13R-9

	SiO2	Al2O3	TiO2	Fe2O3(T)	FeO(T)	MgO	CaO	Na2O	K2O	Cr2O3	P2O5	MnO	Mg#	Cr#	Cr/Fe
13R-3															
Mean (LG-6)	1.43	14.55	0.59	28.10	25.29	10.17	0.24	0.02	0.01	44.69	0.01	0.21	41.76	67.32	1.56
Standard Deviation	0.49	0.13	0.01	0.15	0.13	0.14	0.06	0.02	0.01	0.38	0.00	0.00	0.43	0.12	0.01
13R-9															
Mean (LG-6)	2.44	14.42	0.69	23.04	20.74	10.76	0.79	0.01	0.02	47.58	0.01	0.24	48.03	68.87	2.02
Standard Deviation	0.80	0.42	0.07	0.76	0.69	0.52	0.88	0.01	0.05	1.27	0.01	0.03	1.95	0.68	0.09
Difference of means					4.55	0.59				2.90			6.27	1.55	0.47
Std Dev of the difference of the means					0.22	0.17				0.41			0.63	0.22	0.03

	Au	Ag	Ba	Co	Cu	La	Ni	S	SO3	S from SO3	S	Sr	V
13R-3	ppb	ppm	ppm	ppm	ppm	ppm	ppm	ppm	%	%	ppm	ppm	ppm
Mean (LG-6)	3.20	0.65	7.23	269	13.36	0.23	886.20	206.00	0.01	0.00	24.56	3.24	2052.73
Standard Deviation	1.17	0.11	6	8.17	13.10	0.07	48.34	0.00	0.00	0.00	11.03	3.45	244.54
13R-9	13R-9												
Mean (LG-6)	3.72	19.90	104	243.70	76.35	0.62	578.80	304.50	0.08	0.03	339.58	11.10	2127.40
Standard Deviation	2.32	0.00	102	13.84	31.73	0.94	42.50	56.32	0.02	0.01	71.65	18.16	446.31
Difference of means				25.30	62.99		307.40	98.50			315.02		74.67
Std Dev of the difference of the means				4.86	10.63		18.34	17.81			22.84		154.61

	Y	Zn	Zr	Ir	Os	Pd	Pt	Rh	Ru	IPGE	PPGE	Total PGE	Pt*/Ru*
13R-3	ppm	ppm	ppm	ppb	ppb	ppb	ppb	ppb	ppb				
Mean (LG-6)	0.73	599.23	2.33	74.07	71.20	80.47	275.07	107.60	469.33	614.60	463.13	1077.73	0.77
Standard Deviation	0.12	25.22	0.70	8.45	12.97	18.12	74.39	21.25	83.78	100.42	111.87	169.28	0.19
13R-9													
Mean (LG-6)	1.35	607.55	4.35	86.00	82.40	72.70	246.20	109.20	611.30	779.70	428.10	1207.80	0.55
Standard Deviation	0.75	60.27	6.24	8.58	13.99	23.47	78.18	16.09	100.61	120.72	96.09	183.80	0.12
Difference of means									141.97	165.10	35.03	130.07	0.21
Std Dev of the difference of the means									38.47	46.15	41.93	72.72	0.06

LG-6A

	Total PGE	Cr/Fe
13R-3		
LG-6A mean	1629.67	1.53
std dev	276.05	0.02
13R-9		
LG-6A mean	2365.57	1.64
Std dev	706.54	0.17

Appendix D

Whole rock corrections

ELEMENTS	SiO2	Al2O3	TiO2	Fe2O3	MgO	CaO	Na2O
UNITS	%	%	%	%	%	%	%
DETECTION	0.01	0.01	0.01	0.01	0.01	0.01	0.01
METHOD	FB1/XRF	FB1/XRF	FB1/XRF	FB1/XRF	FB1/XRF	FB1/XRF	FB1/XRF
AMIS0170							
AMIS0170 [certified]							
AR (%)							
AMIS0278							
AMIS0278							
AMIS0278							
AMIS0278							
AMIS0278 [certified]							
Mean							
2σ							
AR (%)							
RSD							
SARM8	4.3	10.44	0.24	20.25	14.63	0.27	0.02
SARM8 [certified]	4.3	10.5	0.24	20.201661	14.6	0.26	
AR (%)	100	99.4285714	100	100.239282	100.205479	103.846154	
AMIS0171							
AMIS0171 [certified]							
AR (%)							
SARM9	0.59	15.08	0.56	27.56	10.73	0.13	
SARM9 [certified]	0.61	15.1	0.56	21.58847	10.8	0.16	
AR (%)	96.7213115	99.8675497	100	127.660737	99.3518519	81.25	
AMIS0323	9.17	12.2	0.58	24.88	10.55	0.49	0.05
AMIS0323 [certified]	9.16	12.24	0.58	25	10.58	0.48	0.06
AR (%)	100.10917	99.6732026	100	99.52	99.7164461	102.083333	83.3333333
OREAS 45d							
OREAS 45d [certified]							
AR (%)							
AMIS0132 (XRF)	28.29	15.98	0.62	18.48	9.92	4.92	0.89
AMIS0132 (ICP)							
AMIS0132 [certified]	28.39	16.2	0.6	18.63	10.08	4.83	0.9
Mean	28.29	15.98	0.62	18.48	9.92	4.92	0.89
2σ							
AR (%)	99.6477633	98.6419753	103.333333	99.194847	98.4126984	101.863354	98.8888889
RSD							
OREAS 45e							
OREAS 45e [certified]							
AR (%)							
AMIS0010							
AMIS0010 [certified]							
AR (%)							
OREAS 13b							
OREAS 13b [certified]							
AR (%)							
OREAS 73b							
OREAS 73b [certified]							
AR (%)							
BLANKS							
Control Blank		X				X	
Control Blank		X				X	
Acid Blank		X				X	
Control Blank							

ELEMENTS	K2O	Cr2O3	P2O5	MnO	Total	LOI	Au
UNITS	%	%	%	%	%	%	ppb
DETECTION	0.01	0.005	0.002	0.01	0.01	0.01	2
METHOD	FB1/XRF	FB1/XRF	FB1/XRF	FB1/XRF	FB1/XRF	/TGA	NS25/MS
AMIS0170							
AMIS0170 [certified]							
AR (%)							
AMIS0278							260
AMIS0278							256
AMIS0278							219
AMIS0278							243
AMIS0278 [certified]							260
Mean							244.5
2σ							36.968455
AR (%)							94.0384615
RSD							0.07560011
SARM8	0.02	48.738	0.008	0.25	100.01		
SARM8 [certified]		48.9	0.00893646	0.25			
AR (%)		99.6687117	89.5209065	100			
AMIS0171							
AMIS0171 [certified]							
AR (%)							
SARM9		46.139	0.006	0.21	100.09		
SARM9 [certified]		46.1	0.00549936	0.21			
AR (%)		100.084599	109.103605	100			
AMIS0323	0.19	39.069	0.023	0.25	99.32		
AMIS0323 [certified]	0.18	39.14		0.25			
AR (%)	105.555556	99.8185999		100			
OREAS 45d							
OREAS 45d [certified]							
AR (%)							
AMIS0132 (XRF)	0.19	19.541	0.049	0.18	99.51		
AMIS0132 (ICP)							
AMIS0132 [certified]	0.19	19.64	0.048	0.18			
Mean	0.19	19.541	0.049	0.18	99.51		
2σ							
AR (%)	100	99.4959267	102.083333	100			
RSD							
OREAS 45e							
OREAS 45e [certified]							
AR (%)							
AMIS0010							25
AMIS0010 [certified]							26
AR (%)							96.1538462
OREAS 13b							
OREAS 13b [certified]							
AR (%)							
OREAS 73b							
OREAS 73b [certified]							
AR (%)							
BLANKS							
Control Blank							X
Control Blank							
Acid Blank							
Control Blank							X

ELEMENTS	Ag	Ba	Co	Cu	La	Ni	S
UNITS	ppm	ppm	ppm	ppm	ppm	ppm	ppm
DETECTION	0.5	2	1	5	0.1	5	50
METHOD	4A/MS	4A/MS	4A/MS	4A/OE	4A/MS	4A/OE	4A/OE
AMIS0170		35	53	719	4.2	1107	4408
AMIS0170 [certified]		37.2	51	709	4.3	1071	4700
AR (%)		94.0860215	103.921569	101.410437	97.6744186	103.361345	93.787234
AMIS0278							
AMIS0278							
AMIS0278							
AMIS0278							
AMIS0278 [certified]							
Mean							
2σ							
AR (%)							
RSD							
SARM8							
SARM8 [certified]							341
AR (%)							0
AMIS0171	4.4	21	784	15697	2.2	>20000	59860
AMIS0171 [certified]	4.21	17.52	820	16220	1.82	24310	
AR (%)	104.513064	119.863014	95.6097561	96.7755857	120.879121		
SARM9							
SARM9 [certified]							28
AR (%)							0
AMIS0323							
AMIS0323 [certified]							8100
AR (%)							0
OREAS 45d		178	31	375	16.7	226	475
OREAS 45d [certified]		183	29.5	371	16.9	231	490
AR (%)		97.2677596	105.084746	101.078167	98.816568	97.8354978	96.9387755
AMIS0132 (XRF)							
AMIS0132 (ICP)		87	166	50	4.6	649	107
AMIS0132 [certified]		81.7		47.2	4.9	684	
Mean		87	166	50	4.6	649	107
2σ							
AR (%)		106.487148		105.932203	93.877551	94.8830409	
RSD							
OREAS 45e	0.5	256	60	789	10.3	454	441
OREAS 45e [certified]	0.311	252	57	780	11	454	460
AR (%)	160.771704	101.587302	105.263158	101.153846	93.6363636	100	95.8695652
AMIS0010							
AMIS0010 [certified]							
AR (%)							
OREAS 13b	0.9	692	78	2406	25.5	2237	11807
OREAS 13b [certified]	0.86	694	75	2327		2247	11900
AR (%)	104.651163	99.7118156	104	103.394929		99.5549622	99.2184874
OREAS 73b	2.2	206	239	479	13.6	15149	30961
OREAS 73b [certified]	0.371	205	240	447	16.6	14800	29400
AR (%)	592.991914	100.487805	99.5833333	107.158837	81.9277108	102.358108	105.309524
BLANKS							
Control Blank	0.8	X	0.008	X	X	X	X
Control Blank	X	X	0.009	X	X	X	X
Acid Blank	X	X	X	X	X	X	X
Control Blank							

ELEMENTS	SO3	Sr	V	Y	Zn	Zr
UNITS	%	ppm	ppm	ppm	ppm	ppm
DETECTION	0.002	0.5	5	0.5	5	1
METHOD	FB1/XRF	4A/MS	4A/OE	4A/MS	4A/OE	4A/MS
AMIS0170		26.9	71	6.3	53	32
AMIS0170 [certified]		25.76	67.3	5.58	51.58	33.43
AR (%)		104.425466	105.497771	112.903226	102.753005	95.722405
AMIS0278						
AMIS0278						
AMIS0278						
AMIS0278						
AMIS0278 [certified]						
Mean						
2σ						
AR (%)						
RSD						
SARM8	0.079					
SARM8 [certified]						
AR (%)						
AMIS0171		16.3	96	4.2	283	16
AMIS0171 [certified]	5.52	18.78	95.85	3.91	299	9.51
AR (%)	0	86.7944622	100.156495	107.41688	94.6488294	168.243954
SARM9	0.006					
SARM9 [certified]						
AR (%)						
AMIS0323	2.045					
AMIS0323 [certified]						
AR (%)						
OREAS 45d		31.5	236	9.4	44	132
OREAS 45d [certified]		31.3	235	9.53	45.7	141
AR (%)		100.638978	100.425532	98.6358867	96.2800875	93.6170213
AMIS0132 (XRF)	0.034					
AMIS0132 (ICP)		137.8	1116	4.1	360	21
AMIS0132 [certified]		142	1108	4.62	373	21.6
Mean	0.034	139.9	1112	4.36	366.5	21.3
2σ						
AR (%)		98.5211268	100.361011	94.3722944	98.2573727	98.6111111
RSD						
OREAS 45e		16.9	321	9	49	104
OREAS 45e [certified]		15.9	322	8.28	46.7	110
AR (%)		106.289308	99.689441	108.695652	104.925054	94.5454545
AMIS0010						
AMIS0010 [certified]						
AR (%)						
OREAS 13b		514.3	314	19.9	134	70
OREAS 13b [certified]		537	330		133	108
AR (%)		95.7728119	95.1515152		100.75188	64.8148148
OREAS 73b		69.3	83	10.9	121	61
OREAS 73b [certified]		69	74	10.9	114	64
AR (%)		100.434783	112.162162	100	106.140351	95.3125
BLANKS						
Control Blank		X	X	X	X	X
Control Blank		X	X	X	X	X
Acid Blank		X	X	X	X	X
Control Blank						

ELEMENTS	Ir	Os	Pd	Pt	Rh	Ru
UNITS	ppb	ppb	ppb	ppb	ppb	ppb
DETECTION	1	1	1	1	1	1
METHOD	NS25/MS	NS25/MS	NS25/MS	NS25/MS	NS25/MS	NS25/MS
AMIS0170						
AMIS0170 [certified]						
AR (%)						
AMIS0278	39	22	2135	1740	151	158
AMIS0278	38	18	2156	1684	152	157
AMIS0278	30	17	1722	1321	123	127
AMIS0278	35	19	1954	1516	138	143
AMIS0278 [certified]	36		2100	1690	150	150
Mean	35.5	19	1991.75	1565.25	141	146.25
2σ	8.08290377	4.3204938	402.80475	377.222746	27.1784228	29.0918087
AR (%)	98.6111111		94.8452381	92.6183432	94	97.5
RSD	0.11384372	0.11369721	0.1011183	0.1204992	0.09637739	0.09945918
SARM8						
SARM8 [certified]						
AR (%)						
AMIS0171						
AMIS0171 [certified]						
AR (%)						
SARM9						
SARM9 [certified]						
AR (%)						
AMIS0323						
AMIS0323 [certified]						
AR (%)						
OREAS 45d						
OREAS 45d [certified]						
AR (%)						
AMIS0132 (XRF)						
AMIS0132 (ICP)						
AMIS0132 [certified]						
Mean						
2σ						
AR (%)						
RSD						
OREAS 45e						
OREAS 45e [certified]						
AR (%)						
AMIS0010	173	107	1276	2074	423	774
AMIS0010 [certified]	170		1330	2050	410	800
AR (%)	101.764706		95.9398496	101.170732	103.170732	96.75
OREAS 13b						
OREAS 13b [certified]						
AR (%)						
OREAS 73b						
OREAS 73b [certified]						
AR (%)						
BLANKS						
Control Blank	X	X	2	X	X	2
Control Blank						
Acid Blank						
Control Blank	1	X	X	4	3	6

ELEMENTS	SiO2	Al2O3	TiO2	Fe2O3	MgO	CaO	Na2O
UNITS	%	%	%	%	%	%	%
DETECTION	0.01	0.01	0.01	0.01	0.01	0.01	0.01
METHOD	FB1/XRF	FB1/XRF	FB1/XRF	FB1/XRF	FB1/XRF	FB1/XRF	FB1/XRF
AMIS0132							
AMIS0132 [certified]	28.39	16.2	0.6	18.63	10.08	4.83	0.9
AR (%)		0	0	0		0	0
AMIS0170							
AMIS0170 [certified]							
AR (%)							
AMIS0171							
AMIS0171 [certified]							
AR (%)							
AMIS0278							
AMIS0278							
AMIS0278							
AMIS0278 [certified]							
Mean							
2σ							
AR (%)							
RSD							
SARM1	75.66	12.07	0.09	1.97	0.04	0.77	3.31
SARM1 [certified]	75.7	12.08	0.090077	2	0.06	0.78	3.36
AR (%)	99.94716	99.91722	99.91407	98.5	66.66667	98.717949	98.5119
SARM2	63.25	17.16	0.04	1.41	0.45	0.68	0.41
SARM2 [certified]	63.63	17.34	0.044205	1.4	0.46	0.68	0.43
AR (%)	99.4028	98.96194	90.48822	100.7143	97.82609	100	95.34884
SY-4	49.63	20.49	0.29	6.2	0.52	7.93	7.14
SY-4 [certified]							
AR (%)							
OREAS 13b							
OREAS 13b [certified]							
AR (%)							
OREAS 45d							
OREAS 45d [certified]							
AR (%)							
OREAS 45e							
OREAS 45e [certified]							
AR (%)							
OREAS 73b							
OREAS 73b [certified]							
AR (%)							
BLANKS							
Control Blank							
Control Blank							
Acid Blank							
Control Blank							

ELEMENTS	K2O	Cr2O3	P2O5	MnO	Total	LOI	Au
UNITS	%	%	%	%	%	%	ppb
DETECTION	0.01	0.01	0.002	0.01	0.01	0.01	2
METHOD	FB1/XRF	FB1/XRF	FB1/XRF	FB1/XRF	FB1/XRF	/TGA	NS25/MS
AMIS0132							
AMIS0132 [certified]	0.19	19.64	0.048	0.18			
AR (%)	0	0	0	0			
AMIS0170							
AMIS0170 [certified]							
AR (%)							
AMIS0171							
AMIS0171 [certified]							
AR (%)							
AMIS0278							254
AMIS0278							244
AMIS0278							268
AMIS0278 [certified]							260
Mean							255.3333
2σ							24.11086
AR (%)							98.20513
RSD							0.047214
SARM1	4.98		0.009	0.02	99.61		
SARM1 [certified]	4.99			0			
AR (%)	99.7996						
SARM2	15.28		0.121	0.01	99.37		
SARM2 [certified]	15.35		0.12	0.01033			
AR (%)	99.54397		100.8333				
SY-4	1.64		0.133	0.11	99.16		
SY-4 [certified]							
AR (%)							
OREAS 13b							
OREAS 13b [certified]							
AR (%)							
OREAS 45d							
OREAS 45d [certified]							
AR (%)							
OREAS 45e							
OREAS 45e [certified]							
AR (%)							
OREAS 73b							
OREAS 73b [certified]							
AR (%)							
BLANKS							
Control Blank							X
Control Blank							
Acid Blank							
Control Blank							X

ELEMENTS	Ag	Ba	Co	Cu	La	Ni	S
UNITS	ppm	ppm	ppm	ppm	ppm	ppm	ppm
DETECTION	0.5	1	1	5	0.1	5	50
METHOD	4A/MS	4A/MS	4A/MS	4A/OE	4A/MS	4A/OE	4A/OE
AMIS0132		85	166	50	5	701	118
AMIS0132 [certified]		81.7		47.2	4.9	684	
AR (%)		104.0392		105.9322	102.0408	102.4854	
AMIS0170		36	51	730	4.3	1120	4703
AMIS0170 [certified]		37.2	51	709	4.3	1071	4700
AR (%)		96.77419	100	102.9619	100	104.5752	100.0638
AMIS0171	3.9	17	673	16204	2.4	23481	62809
AMIS0171 [certified]	4.21	17.52	820	16220	1.82	24310	
AR (%)	92.63658	97.03196	82.07317	99.90136	131.8681	96.58988	
AMIS0278							
AMIS0278							
AMIS0278							
AMIS0278 [certified]							
Mean							
2σ							
AR (%)							
RSD							
SARM1							
SARM1 [certified]							
AR (%)							
SARM2							
SARM2 [certified]							
AR (%)							
SY-4							
SY-4 [certified]							
AR (%)							
OREAS 13b	1	724	74	2389	27.7	2228	12487
OREAS 13b [certified]	0.86	694	75	2327		2247	11900
AR (%)	116.2791	104.3228	98.66667	102.6644		99.15443	104.9328
OREAS 45d		185	30	369	17.9	229	481
OREAS 45d [certified]		183	29.5	371	16.9	231	490
AR (%)		101.0929	101.6949	99.46092	105.9172	99.1342	98.16327
OREAS 45e		253	59	785	11.4	451	452
OREAS 45e [certified]	0.311	252	57	780	11	454	460
AR (%)		100.3968	103.5088	100.641	103.6364	99.33921	98.26087
OREAS 73b		210	241	450	16.1	13889	29688
OREAS 73b [certified]	0.371	205	240	447	16.6	14800	29400
AR (%)		102.439	100.4167	100.6711	96.98795	93.84459	100.9796
BLANKS							
Control Blank	X	X	X	X	X	X	X
Control Blank	X	X	X	X	X	X	X
Acid Blank	X	X	X	X	X	X	X
Control Blank							X

ELEMENTS	SO3	Sr	V	Y	Zn	Zr
UNITS	%	ppm	ppm	ppm	ppm	ppm
DETECTION	0.01	0.5	5	0.5	5	1
METHOD	FB1/XRF	4A/MS	4A/OE	4A/MS	4A/OE	4A/MS
AMIS0132		141.7	1260	4.8	314	23
AMIS0132 [certified]		142	1108	4.62	373	21.6
AR (%)		99.78873	113.7184	103.8961	84.18231	106.4815
AMIS0170		25.7	67	5.4	54	33
AMIS0170 [certified]		25.76	67.3	5.58	51.58	33.43
AR (%)		99.76708	99.55423	96.77419	104.6917	98.71373
AMIS0171		16.8	94	3.7	306	14
AMIS0171 [certified]	5.52	18.78	95.85	3.91	299	9.51
AR (%)	0	89.45687	98.0699	94.62916	102.3411	147.2135
AMIS0278						
AMIS0278						
AMIS0278						
AMIS0278 [certified]						
Mean						
2σ						
AR (%)						
RSD						
SARM1	0.02					
SARM1 [certified]						
AR (%)						
SARM2						
SARM2 [certified]						
AR (%)						
SY-4	0.04					
SY-4 [certified]						
AR (%)						
OREAS 13b		550.3	324	21.2	132	77
OREAS 13b [certified]		537	330		133	108
AR (%)		102.4767	98.18182		99.24812	71.2963
OREAS 45d		32.8	226	9.5	43	137
OREAS 45d [certified]		31.3	235	9.53	45.7	141
AR (%)		104.7923	96.17021	99.6852	94.0919	97.16312
OREAS 45e		15.9	308	8.3	44	104
OREAS 45e [certified]		15.9	322	8.28	46.7	110
AR (%)		100	95.65217	100.2415	94.21842	94.54545
OREAS 73b		66.6	70	10.1	114	63
OREAS 73b [certified]		69	74	10.9	114	64
AR (%)		96.52174	94.59459	92.66055	100	98.4375
BLANKS						
Control Blank		X	X	X	X	X
Control Blank		X	X	X	X	X
Acid Blank		X	X	X	X	X
Control Blank						

ELEMENTS	Ir	Os	Pd	Pt	Rh	Ru
UNITS	ppb	ppb	ppb	ppb	ppb	ppb
DETECTION	1	1	1	1	1	1
METHOD	NS25/MS	NS25/MS	NS25/MS	NS25/MS	NS25/MS	NS25/MS
AMIS0132						
AMIS0132 [certified]						
AR (%)						
AMIS0170						
AMIS0170 [certified]						
AR (%)						
AMIS0171						
AMIS0171 [certified]						
AR (%)						
AMIS0278	36	19	2132	1672	154	151
AMIS0278	36	17	2086	1665	155	144
AMIS0278	35	18	2052	1660	152	150
AMIS0278 [certified]	36		2100	1690	150	150
Mean	35.66667	18	2090	1665.667	153.6667	148.3333
2σ	1.154701	2	80.29944	12.05543	3.05505	7.571878
AR (%)	99.07407		99.52381	98.56016	102.4444	98.88889
RSD	0.016187	0.055556	0.01921	0.003619	0.009941	0.025523
SARM1						
SARM1 [certified]						
AR (%)						
SARM2						
SARM2 [certified]						
AR (%)						
SY-4						
SY-4 [certified]						
AR (%)						
OREAS 13b						
OREAS 13b [certified]						
AR (%)						
OREAS 45d						
OREAS 45d [certified]						
AR (%)						
OREAS 45e						
OREAS 45e [certified]						
AR (%)						
OREAS 73b						
OREAS 73b [certified]						
AR (%)						
BLANKS						
Control Blank	X	X	1	1	X	1
Control Blank						
Acid Blank						
Control Blank						X

Appendix E

EPMA data for Cr-spinel

	Sample Name/Number						
Wt% Oxides	1 / 1 . (13R9-212.90E	4 / 1 .	6 / 1 .	7 / 1 .	8 / 1 .	9 / 1 .	10 / 1 .
SiO2	0.01	0.03	0.05	0.04	0.06	0.03	0.01
TiO2	0.7	0.68	0.72	0.73	0.68	0.72	0.75
Al2O3	15.76	15.97	15.76	16.13	15.92	15.73	16.19
Cr2O3	47.78	47.22	47.34	47.42	47.16	46.69	46.95
V2O3	0.55	0.55	0.58	0.56	0.54	0.55	0.56
FeO	26.18	26.3	26.31	26.03	25.72	27.69	26.57
MnO	0	0	0	0	0	0	0
MgO	8.15	8.97	8.04	8.03	8.49	7.92	8.93
CaO							
ZnO	0.02	0.13	0.04	0.05	0.06	0.11	0.07
NiO	0.04	0.1	0.06	0.08	0.08	0.11	0.05
Total	99.19	99.95	98.9	99.07	98.71	99.55	100.08
A.P.F.U Fe Corrected							
Si	0.00	0.01	0.01	0.01	0.02	0.01	0.00
Ti	0.14	0.13	0.14	0.14	0.13	0.14	0.15
Al	4.88	4.87	4.89	4.99	4.93	4.86	4.93
Cr	9.92	9.67	9.86	9.84	9.80	9.67	9.59
V	0.12	0.11	0.12	0.12	0.11	0.12	0.12
Fe(ii)	4.94	4.63	4.98	4.98	4.79	5.01	4.68
Fe(iii)	0.81	1.07	0.82	0.74	0.86	1.06	1.06
Mn	0	0	0	0	0	0	0
Mg	3.19	3.46	3.16	3.14	3.33	3.09	3.44
Zn	0.00	0.02	0.01	0.01	0.01	0.02	0.01
Ni	0.01	0.03	0.02	0.02	0.02	0.03	0.01
Total	**24**	**24**	**24**	**24**	**24**	**24**	**24**
Fe2/(Fe2+Fe3)	0.859	0.813	0.859	0.871	0.848	0.825	0.815
Fe3/(Fe3+Fe2)	0.141	0.187	0.141	0.129	0.152	0.175	0.185
Wt % ox Corrected Fe							
SiO2	0.01	0.03	0.05	0.04	0.06	0.03	0.01
TiO2	0.7	0.68	0.72	0.73	0.68	0.72	0.75
Al2O3	15.76	15.97	15.76	16.13	15.92	15.73	16.19
Cr2O3	47.78	47.22	47.34	47.42	47.16	46.69	46.95
V2O3	0.55	0.55	0.58	0.56	0.54	0.55	0.56
FeO	22.49	21.37	22.59	22.68	21.81	22.85	21.66
Fe2O3	4.10	5.48	4.13	3.72	4.35	5.38	5.46
MnO	0.00	0.00	0.00	0.00	0.00	0.00	0.00
MgO	8.15	8.97	8.04	8.03	8.49	7.92	8.93
ZnO	0.00	0.00	0.00	0.00	0.00	0.00	0.00
NiO	0.04	0.1	0.06	0.08	0.08	0.11	0.05
Total	**99.58**	**100.37**	**99.27**	**99.39**	**99.09**	**99.98**	**100.56**
Mg #	39.25	42.80	38.81	38.69	40.97	38.19	42.36
Cr #	67.04	66.48	66.83	66.35	66.52	66.57	66.05
Ni (ppm)	314.3	785.8	471.5	628.6	628.6	864.4	392.9
Cr/Fe(tot)	1.73	1.70	1.70	1.72	1.73	1.59	1.67

	Sample Name/Number						
Wt% Oxides	11 / 1 .	12 / 1 .	13 / 1 .	14 / 1 .	15 / 1 .	17 / 1 .	23 / 1 .
SiO2	0.03	0.03	0.01	0.02	0.03	0.03	0.05
TiO2	0.69	0.65	0.77	0.71	0.75	0.7	0.69
Al2O3	16.12	15.95	16.24	15.58	16.59	15.68	16.24
Cr2O3	47.18	46.95	46.45	47.12	46.63	47.12	47.58
V2O3	0.56	0.57	0.57	0.55	0.55	0.53	0.56
FeO	26.02	26.34	26.38	25.79	26.21	26.01	25.92
MnO	0	0	0	0	0	0	0
MgO	9.35	8.01	7.98	9.17	9.41	9.37	8.2
CaO							
ZnO	0.11	0.1	0.1	0.11	0.06	0.08	0.13
NiO	0.03	0.06	0.01	0.07	0.07	0.1	0.08
Total	100.09	98.66	98.51	99.12	100.3	99.62	99.45
A.P.F.U Fe Corrected							
Si	0.01	0.01	0.00	0.01	0.01	0.01	0.01
Ti	0.13	0.13	0.15	0.14	0.14	0.14	0.14
Al	4.90	4.96	5.05	4.79	5.02	4.79	5.00
Cr	9.61	9.79	9.69	9.72	9.46	9.66	9.83
V	0.12	0.12	0.12	0.12	0.11	0.11	0.12
Fe(ii)	4.52	4.95	4.99	4.54	4.52	4.48	4.91
Fe(iii)	1.09	0.86	0.83	1.09	1.10	1.16	0.76
Mn	0	0	0	0	0	0	0
Mg	3.59	3.15	3.14	3.57	3.60	3.62	3.19
Zn	0.02	0.02	0.02	0.02	0.01	0.02	0.03
Ni	0.01	0.02	0.00	0.02	0.02	0.03	0.02
Total	**24**	**24**	**24**	**24**	**24**	**24**	**24**
Fe2/(Fe2+Fe3)	0.806	0.852	0.858	0.807	0.804	0.795	0.867
Fe3/(Fe3+Fe2)	0.194	0.148	0.142	0.193	0.196	0.205	0.133
Wt % ox Corrected Fe							
SiO2	0.03	0.03	0.01	0.02	0.03	0.03	0.05
TiO2	0.69	0.65	0.77	0.71	0.75	0.7	0.69
Al2O3	16.12	15.95	16.24	15.58	16.59	15.68	16.24
Cr2O3	47.18	46.95	46.45	47.12	46.63	47.12	47.58
V2O3	0.56	0.57	0.57	0.55	0.55	0.53	0.56
FeO	20.97	22.45	22.63	20.80	21.07	20.68	22.46
Fe2O3	5.62	4.32	4.17	5.54	5.71	5.93	3.84
MnO	0.00	0.00	0.00	0.00	0.00	0.00	0.00
MgO	9.35	8.01	7.98	9.17	9.41	9.37	8.2
ZnO	0.00	0.00	0.00	0.00	0.00	0.00	0.00
NiO	0.03	0.06	0.01	0.07	0.07	0.1	0.08
Total	**100.54**	**98.99**	**98.83**	**99.56**	**100.81**	**100.13**	**99.70**
Mg #	44.29	38.87	38.60	44.00	44.32	44.68	39.42
Cr #	66.26	66.38	65.74	66.98	65.34	66.84	66.28
Ni (ppm)	235.7	471.5	78.6	550.0	550.0	785.8	628.6
Cr/Fe(tot)	1.71	1.69	1.66	1.73	1.68	1.71	1.74

	Sample Name/Number					
Wt% Oxides	25 / 1 . (13R9-212.90E	71 / 1 . (13R3-168.24A	78 / 1 .	80 / 1 .	81 / 1 .	82 / 1 . (13R3-168.24A
SiO2	0.05	0.03	0.01	0.01	0.02	0.02
TiO2	0.75	0.75	0.68	0.61	0.68	0.73
Al2O3	16.05	12.06	12.04	11.72	12.04	12.42
Cr2O3	47.85	43.68	42.16	43.48	43.81	43.06
V2O3	0.52	0.33	0.36	0.35	0.32	0.34
FeO	26.17	35.26	36.36	36.02	35.08	35.02
MnO	0	0	0	0	0	0
MgO	8	7.33	6.54	7.03	6.54	7.06
CaO						
ZnO	0.12	0.09	0.04	0.09	0.1	0.19
NiO	0.04	0.12	0.15	0.13	0.08	0.17
Total	99.55	99.65	98.34	99.44	98.67	99.01
A.P.F.U Fe Corrected						
Si	0.01	0.01	0.00	0.00	0.01	0.01
Ti	0.15	0.15	0.14	0.12	0.14	0.15
Al	4.95	3.78	3.84	3.69	3.83	3.92
Cr	9.90	9.19	9.02	9.19	9.36	9.11
V	0.11	0.07	0.08	0.08	0.07	0.07
Fe(ii)	5.01	5.20	5.45	5.27	5.47	5.25
Fe(iii)	0.72	2.64	2.78	2.79	2.46	2.59
Mn	0	0	0	0	0	0
Mg	3.12	2.91	2.64	2.80	2.63	2.82
Zn	0.02	0.02	0.01	0.02	0.02	0.04
Ni	0.01	0.03	0.04	0.04	0.02	0.05
Total	**24**	**24**	**24**	**24**	**24**	**24**
Fe2/(Fe2+Fe3)	0.874	0.663	0.663	0.654	0.690	0.670
Fe3/(Fe3+Fe2)	0.126	0.337	0.337	0.346	0.310	0.330
Wt % ox Corrected Fe						
SiO2	0.05	0.03	0.01	0.01	0.02	0.02
TiO2	0.75	0.75	0.68	0.61	0.68	0.73
Al2O3	16.05	12.06	12.04	11.72	12.04	12.42
Cr2O3	47.85	43.68	42.16	43.48	43.81	43.06
V2O3	0.52	0.33	0.36	0.35	0.32	0.34
FeO	22.88	23.37	24.09	23.56	24.21	23.45
Fe2O3	3.66	13.21	13.64	13.85	12.08	12.85
MnO	0.00	0.00	0.00	0.00	0.00	0.00
MgO	8	7.33	6.54	7.03	6.54	7.06
ZnO	0.00	0.00	0.00	0.00	0.00	0.00
NiO	0.04	0.12	0.15	0.13	0.08	0.17
Total	**99.80**	**100.88**	**99.67**	**100.74**	**99.78**	**100.11**
Mg #	38.40	35.86	32.61	34.72	32.50	34.92
Cr #	66.67	70.84	70.14	71.34	70.94	69.93
Ni (ppm)	314.3	942.9	1178.7	1021.5	628.6	1335.8
Cr/Fe(tot)	1.73	1.17	1.10	1.14	1.18	1.16

	Sample Name/Number					
Wt% Oxides	86 / 1 . (13R9-213.63D	89 / 1 .	91 / 1 .	92 / 1 .	94 / 1 .	95 / 1 . (13R9-213.63D
SiO2	0.02	0.09	0.04	0.01	0.01	0.03
TiO2	0.76	0.76	0.66	0.77	0.73	0.78
Al2O3	20.66	19.55	20.46	20.19	19.9	19.62
Cr2O3	40.29	40.74	40.38	40.38	40.86	40.4
V2O3	0.64	0.61	0.65	0.62	0.62	0.66
FeO	29.97	29.11	29.89	29.44	28.86	30.07
MnO	0	0	0	0	0	0
MgO	6.88	6.84	7.66	7.76	7.25	6.62
CaO						
ZnO	0.17	0.13	0.1	0.17	0.17	0.12
NiO	0.11	0.07	0.06	0.06	0.1	0.06
Total	99.5	97.9	99.9	99.4	98.5	98.36
A.P.F.U Fe Corrected						
Si	0.01	0.02	0.01	0.00	0.00	0.01
Ti	0.15	0.15	0.13	0.15	0.14	0.15
Al	6.29	6.07	6.18	6.13	6.12	6.07
Cr	8.23	8.48	8.18	8.22	8.43	8.39
V	0.13	0.13	0.13	0.13	0.13	0.14
Fe(ii)	5.44	5.44	5.18	5.12	5.27	5.53
Fe(iii)	1.04	0.97	1.23	1.22	1.03	1.07
Mn	0	0	0	0	0	0
Mg	2.65	2.69	2.93	2.98	2.82	2.59
Zn	0.03	0.03	0.02	0.03	0.03	0.02
Ni	0.03	0.02	0.02	0.02	0.03	0.02
Total	**24**	**24**	**24**	**24**	**24**	**24**
Fe2/(Fe2+Fe3)	0.840	0.849	0.808	0.808	0.836	0.837
Fe3/(Fe3+Fe2)	0.160	0.151	0.192	0.192	0.164	0.163
Wt % ox Corrected Fe						
SiO2	0.02	0.09	0.04	0.01	0.01	0.03
TiO2	0.76	0.76	0.66	0.77	0.73	0.78
Al2O3	20.66	19.55	20.46	20.19	19.9	19.62
Cr2O3	40.29	40.74	40.38	40.38	40.86	40.4
V2O3	0.64	0.61	0.65	0.62	0.62	0.66
FeO	25.17	24.71	24.15	23.79	24.14	25.18
Fe2O3	5.33	4.89	6.38	6.28	5.25	5.44
MnO	0.00	0.00	0.00	0.00	0.00	0.00
MgO	6.88	6.84	7.66	7.76	7.25	6.62
ZnO	0.00	0.00	0.00	0.00	0.00	0.00
NiO	0.11	0.07	0.06	0.06	0.1	0.06
Total	**99.86**	**98.26**	**100.44**	**99.86**	**98.86**	**98.78**
Mg #	32.76	33.04	36.12	36.77	34.87	31.91
Cr #	56.68	58.30	56.97	57.30	57.94	58.01
Ni (ppm)	864.4	550.0	471.5	471.5	785.8	471.5
Cr/Fe(tot)	1.27	1.32	1.28	1.30	1.34	1.27

	Sample Name/Number				
Wt% Oxides	31 / 1 . (13R9-213.63H	32 / 1 .	35 / 1 .	39 / 1 .	40 / 1 . (13R9-213.63H)
SiO2	0	0.02	0.03	0.01	0.02
TiO2	0.52	0.59	0.91	0.97	0.75
Al2O3	22.98	21.37	19.46	18.77	19.28
Cr2O3	38.31	39.96	40.84	42.13	41.42
V2O3	0.53	0.57	0.63	0.63	0.58
FeO	29.52	29.68	30.29	29.95	29.87
MnO	0	0	0	0	0
MgO	7.38	6.18	6.17	6.32	7.03
CaO					
ZnO	0.3	0.19	0.31	0.25	0.23
NiO	0.06	0.05	0.07	0.06	0
Total	99.6	98.61	98.71	99.09	99.18
A.P.F.U Fe Corrected					
Si	0.00	0.01	0.01	0.00	0.01
Ti	0.10	0.12	0.18	0.19	0.15
Al	6.90	6.58	6.03	5.81	5.92
Cr	7.72	8.25	8.49	8.75	8.53
V	0.11	0.12	0.13	0.13	0.12
Fe(ii)	5.22	5.67	5.69	5.66	5.38
Fe(iii)	1.07	0.81	0.97	0.92	1.13
Mn	0	0	0	0	0
Mg	2.80	2.41	2.42	2.47	2.73
Zn	0.06	0.04	0.06	0.05	0.04
Ni	0.02	0.01	0.02	0.02	0.00
Total	**24**	**24**	**24**	**24**	**24**
Fe2/(Fe2+Fe3)	0.830	0.874	0.854	0.860	0.827
Fe3/(Fe3+Fe2)	0.170	0.126	0.146	0.140	0.173
Wt % ox Corrected Fe					
SiO2	0	0.02	0.03	0.01	0.02
TiO2	0.52	0.59	0.91	0.97	0.75
Al2O3	22.98	21.37	19.46	18.77	19.28
Cr2O3	38.31	39.96	40.84	42.13	41.42
V2O3	0.53	0.57	0.63	0.63	0.58
FeO	24.50	25.95	25.88	25.75	24.69
Fe2O3	5.57	4.15	4.90	4.67	5.75
MnO	0.00	0.00	0.00	0.00	0.00
MgO	7.38	6.18	6.17	6.32	7.03
ZnO	0.00	0.00	0.00	0.00	0.00
NiO	0.06	0.05	0.07	0.06	0
Total	**99.86**	**98.84**	**98.89**	**99.31**	**99.53**
Mg #	34.93	29.80	29.83	30.43	33.66
Cr #	52.79	55.64	58.47	60.09	59.04
Ni (ppm)	471.5	392.9	550.0	471.5	0.0
Cr/Fe(tot)	1.23	1.27	1.27	1.33	1.31

Appendix F

EPMA data for Orthopyroxene

	Sample Name/Number						
Wt% Oxides	27 / 1 . (13R9-212.90B)	29 / 1 .	30 / 1 .	31 / 1 .	33 / 1 .	34 / 1 .	36 / 1 .
SiO2	54.82	55.93	56.49	55.11	54.94	55.14	54.83
TiO2	0.08	0.08	0.09	0.08	0.07	0.08	0.09
Al2O3	0.94	0.89	0.8	1.01	1.03	0.87	0.98
Cr2O3	0.31	0.31	0.28	0.37	0.33	0.3	0.33
FeO	10.82	10.21	10.13	10.7	9.79	10.21	9.94
MnO	0.21	0.22	0.19	0.22	0.19	0.21	0.17
NiO							
MgO	31.98	31.78	32.44	32.03	31.44	31.28	31.67
CaO							
Na2O	0.02	0	0	0	0.02	0	0.01
ZrO2							
Total	99.8	100.35	100.76	100.08	98.48	98.65	98.56
A.P.F.U Fe Corrected							
Si	1.94	1.97	1.97	1.94	1.97	1.97	1.96
Al4	0.06	0.03	0.03	0.06	0.03	0.03	0.04
Al6	0.00	0.01	0.00	0.00	0.01	0.01	0.00
Fe3	0.07	0.00	0.01	0.06	0.01	0.00	0.03
Ti	0.00	0.00	0.00	0.00	0.00	0.00	0.00
Cr	0.01	0.01	0.01	0.01	0.01	0.01	0.01
Zr	0.00	0.00	0.00	0.00	0.00	0.00	0.00
Ni	0.00	0.00	0.00	0.00	0.00	0.00	0.00
Mg	1.68	1.67	1.69	1.68	1.68	1.67	1.69
Fe2	0.25	0.30	0.28	0.26	0.28	0.30	0.27
Mn	0.01	0.01	0.01	0.01	0.01	0.01	0.01
Ca	0.00	0.00	0.00	0.00	0.00	0.00	0.00
Na	0.00	0.00	0.00	0.00	0.00	0.00	0.00
Wt % ox Corrected Fe							
SiO2	54.82	55.93	56.49	55.11	54.94	55.14	54.83
TiO2	0.08	0.08	0.09	0.08	0.07	0.08	0.09
Al2O3	0.94	0.89	0.8	1.01	1.03	0.87	0.98
Cr2O3	0.31	0.31	0.28	0.37	0.33	0.3	0.33
Fe2O3	2.78	0.14	0.57	2.27	0.39	0.19	1.07
FeO	8.32	10.09	9.62	8.66	9.44	10.04	8.98
MnO	0.21	0.22	0.19	0.22	0.19	0.21	0.17
NiO	0.00	0.00	0.00	0.00	0.00	0.00	0.00
MgO	31.98	31.78	32.44	32.03	31.44	31.28	31.67
CaO	0.00	0.00	0.00	0.00	0.00	0.00	0.00
Na2O	0.02	0.00	0.00	0.00	0.02	0.00	0.01
ZrO2	0.00	0.00	0.00	0.00	0.00	0.00	0.00
Total	99.46	99.43	100.48	99.75	97.85	98.11	98.13
Mg# (Fe2)	87.26	84.88	85.74	86.83	85.59	84.74	86.27

	Sample Name/Number					
Wt% Oxides	39 / 1 . (13R9-212.90B)	52 / 1 . (13R3-168.24A)	53 / 1 .	57 / 1 .	59 / 1 .	60 / 1 .
SiO2	56.42	55.32	55.59	55.47	54.82	55.01
TiO2	0.08	0.08	0.09	0.07	0.07	0.08
Al2O3	0.83	1.16	1.19	1.15	1.1	1.13
Cr2O3	0.3	0.41	0.43	0.44	0.39	0.43
FeO	10.53	11.75	10.35	10.85	10.19	10.77
MnO	0.2	0.25	0.24	0.23	0.23	0.24
NiO						
MgO	32.08	31.05	31.62	31.36	31.71	30.72
CaO						
Na2O	0	0.01	0.01	0.01	0	0
ZrO2						
Total	100.95	100.94	100.36	100.15	99.01	99.15
A.P.F.U Fe Corrected						
Si	1.97	1.95	1.96	1.96	1.95	1.97
Al4	0.03	0.05	0.04	0.04	0.05	0.03
Al6	0.01	0.00	0.01	0.01	0.00	0.02
Fe3	0.01	0.03	0.01	0.02	0.04	0.00
Ti	0.00	0.00	0.00	0.00	0.00	0.00
Cr	0.01	0.01	0.01	0.01	0.01	0.01
Zr	0.00	0.00	0.00	0.00	0.00	0.00
Ni	0.00	0.00	0.00	0.00	0.00	0.00
Mg	1.67	1.63	1.66	1.65	1.68	1.64
Fe2	0.30	0.31	0.29	0.30	0.26	0.32
Mn	0.01	0.01	0.01	0.01	0.01	0.01
Ca	0.00	0.00	0.00	0.00	0.00	0.00
Na	0.00	0.00	0.00	0.00	0.00	0.00
Wt % ox Corrected Fe						
SiO2	56.42	55.32	55.59	55.47	54.82	55.01
TiO2	0.08	0.08	0.09	0.07	0.07	0.08
Al2O3	0.83	1.16	1.19	1.15	1.1	1.13
Cr2O3	0.3	0.41	0.43	0.44	0.39	0.43
Fe2O3	0.41	1.30	0.49	0.70	1.47	0.00
FeO	10.16	10.58	9.91	10.22	8.86	10.77
MnO	0.20	0.25	0.24	0.23	0.23	0.24
NiO	0.00	0.00	0.00	0.00	0.00	0.00
MgO	32.08	31.05	31.62	31.36	31.71	30.72
CaO	0.00	0.00	0.00	0.00	0.00	0.00
Na2O	0.00	0.01	0.01	0.01	0.00	0.00
ZrO2	0.00	0.00	0.00	0.00	0.00	0.00
Total	100.48	100.16	99.57	99.65	98.66	98.38
Mg# (Fe2)	84.91	83.95	85.05	84.54	86.44	83.56

	Sample Name/Number							
Wt% Oxides	61 / 1 .	62 / 1 .	63 / 1 .	64 / 1 .	65 / 1 .	66 / 1 .	67 / 1 .	68 / 1 .
SiO2	55.27	54.88	54.81	55.22	54.58	54.51	55.06	54.61
TiO2	0.1	0.07	0.07	0.06	0.08	0.09	0.09	0.07
Al2O3	1.19	1.2	1.19	1.17	1.08	1.07	1.16	1.16
Cr2O3	0.4	0.39	0.48	0.36	0.39	0.33	0.43	0.49
FeO	11.3	11.45	11.88	11.47	11.27	11.2	11.44	11.32
MnO	0.25	0.26	0.24	0.21	0.26	0.21	0.24	0.25
NiO								
MgO	31.16	31.04	30.88	30.67	31.15	30.73	30.94	31.04
CaO								
Na2O	0	0.01	0	0	0	0.01	0.02	0
ZrO2								
Total	100.46	100.14	100.16	99.78	99.5	98.91	100.09	99.8
A.P.F.U Fe Corrected								
Si	1.95	1.95	1.94	1.96	1.94	1.96	1.95	1.94
Al4	0.05	0.05	0.06	0.04	0.06	0.04	0.05	0.06
Al6	0.00	0.00	0.00	0.01	0.00	0.00	0.00	0.00
Fe3	0.03	0.04	0.05	0.01	0.05	0.03	0.03	0.05
Ti	0.00	0.00	0.00	0.00	0.00	0.00	0.00	0.00
Cr	0.01	0.01	0.01	0.01	0.01	0.01	0.01	0.01
Zr	0.00	0.00	0.00	0.00	0.00	0.00	0.00	0.00
Ni	0.00	0.00	0.00	0.00	0.00	0.00	0.00	0.00
Mg	1.64	1.64	1.63	1.63	1.65	1.64	1.64	1.65
Fe2	0.31	0.30	0.31	0.33	0.28	0.31	0.31	0.29
Mn	0.01	0.01	0.01	0.01	0.01	0.01	0.01	0.01
Ca	0.00	0.00	0.00	0.00	0.00	0.00	0.00	0.00
Na	0.00	0.00	0.00	0.00	0.00	0.00	0.00	0.00
Wt % ox Corrected Fe								
SiO2	55.27	54.88	54.81	55.22	54.58	54.51	55.06	54.61
TiO2	0.1	0.07	0.07	0.06	0.08	0.09	0.09	0.07
Al2O3	1.19	1.2	1.19	1.17	1.08	1.07	1.16	1.16
Cr2O3	0.4	0.39	0.48	0.36	0.39	0.33	0.43	0.49
Fe2O3	1.01	1.55	1.73	0.29	1.91	1.08	1.11	1.70
FeO	10.39	10.05	10.32	11.21	9.55	10.23	10.44	9.79
MnO	0.25	0.26	0.24	0.21	0.26	0.21	0.24	0.25
NiO	0.00	0.00	0.00	0.00	0.00	0.00	0.00	0.00
MgO	31.16	31.04	30.88	30.67	31.15	30.73	30.94	31.04
CaO	0.00	0.00	0.00	0.00	0.00	0.00	0.00	0.00
Na2O	0.00	0.01	0.00	0.00	0.00	0.01	0.02	0.00
ZrO2	0.00	0.00	0.00	0.00	0.00	0.00	0.00	0.00
Total	99.77	99.46	99.72	99.19	99.00	98.26	99.49	99.11
Mg# (Fe2)	84.24	84.62	84.21	82.98	85.32	84.26	84.08	84.97

	Sample Name/Number					
Wt% Oxides	69 / 1 . (13R3-168.24A)	102 / 1 . (13R9-213.63D)	103 / 1 .	104 / 1 .	105 / 1 .	106 / 1 .
SiO2	55	54.72	55.44	54.48	54.67	55.2
TiO2	0.07	0.1	0.12	0.08	0.09	0.08
Al2O3	1.19	1.08	1.29	1.24	1.19	1.44
Cr2O3	0.46	0.3	0.33	0.32	0.3	0.47
FeO	11.9	11.32	12.03	11.3	11.39	12.43
MnO	0.25	0.22	0.2	0.21	0.25	0.21
NiO						
MgO	30.92	29.78	30.4	29.93	30.06	30.21
CaO						
Na2O	0	0	0.01	0	0	0
ZrO2						
Total	100.43	98.05	100.62	98.39	98.48	100.71
A.P.F.U Fe Corrected						
Si	1.95	1.98	1.96	1.97	1.97	1.96
Al4	0.05	0.02	0.04	0.03	0.03	0.04
Al6	0.00	0.03	0.02	0.03	0.02	0.02
Fe3	0.04	0.00	0.00	0.00	0.00	0.01
Ti	0.00	0.00	0.00	0.00	0.00	0.00
Cr	0.01	0.01	0.01	0.01	0.01	0.01
Zr	0.00	0.00	0.00	0.00	0.00	0.00
Ni	0.00	0.00	0.00	0.00	0.00	0.00
Mg	1.63	1.61	1.61	1.61	1.62	1.59
Fe2	0.31	0.34	0.35	0.34	0.34	0.36
Mn	0.01	0.01	0.01	0.01	0.01	0.01
Ca	0.00	0.00	0.00	0.00	0.00	0.00
Na	0.00	0.00	0.00	0.00	0.00	0.00
Wt % ox Corrected Fe						
SiO2	55	54.72	55.44	54.48	54.67	55.2
TiO2	0.07	0.1	0.12	0.08	0.09	0.08
Al2O3	1.19	1.08	1.29	1.24	1.19	1.44
Cr2O3	0.46	0.3	0.33	0.32	0.3	0.47
Fe2O3	1.59	0.00	0.07	0.00	0.00	0.45
FeO	10.47	11.32	11.97	11.30	11.39	12.02
MnO	0.25	0.22	0.20	0.21	0.25	0.21
NiO	0.00	0.00	0.00	0.00	0.00	0.00
MgO	30.92	29.78	30.40	29.93	30.06	30.21
CaO	0.00	0.00	0.00	0.00	0.00	0.00
Na2O	0.00	0.00	0.01	0.00	0.00	0.00
ZrO2	0.00	0.00	0.00	0.00	0.00	0.00
Total	99.95	97.52	99.83	97.56	97.95	100.09
Mg# (Fe2)	84.04	82.42	81.91	82.52	82.47	81.75

	Sample Name/Number								
Wt% Oxides	107 / 1 .	108 / 1 .	109 / 1 .	110 / 1 .	111 / 1 .	113 / 1 .	114 / 1 .	115 / 1 .	20 / 1 . (13R9-213.63H)
SiO2	54.91	54.81	53.89	55.04	54.9	54.76	55.04	55.67	55.47
TiO2	0.06	0.09	0.09	0.11	0.1	0.08	0.1	0.08	0.1
Al2O3	0.69	1.3	1.26	1.2	1.16	1.27	1.22	1.16	1.19
Cr2O3	0.22	0.39	0.36	0.32	0.26	0.42	0.4	0.34	0.33
FeO	11.11	12.28	11.77	12.7	12.58	12.39	11.77	11.86	12.64
MnO	0.23	0.26	0.25	0.26	0.22	0.23	0.24	0.2	0.25
NiO									
MgO	31.28	30.14	30.67	30.39	30.31	30.2	30.34	30.49	29.99
CaO									
Na2O	0	0	0.01	0	0.01	0.01	0.01	0	0
ZrO2									
Total	98.74	100	98.9	100.67	100.31	100	99.92	100.47	100.77
A.P.F.U Fe Corrected									
Si	1.96	1.96	1.93	1.95	1.95	1.95	1.96	1.97	1.97
Al4	0.04	0.04	0.07	0.05	0.05	0.05	0.04	0.03	0.03
Al6	0.00	0.01	0.00	0.00	0.00	0.00	0.01	0.02	0.02
Fe3	0.04	0.02	0.07	0.04	0.03	0.03	0.01	0.00	0.00
Ti	0.00	0.00	0.00	0.00	0.00	0.00	0.00	0.00	0.00
Cr	0.01	0.01	0.01	0.01	0.01	0.01	0.01	0.01	0.01
Zr	0.00	0.00	0.00	0.00	0.00	0.00	0.00	0.00	0.00
Ni	0.00	0.00	0.00	0.00	0.00	0.00	0.00	0.00	0.00
Mg	1.66	1.60	1.64	1.60	1.61	1.60	1.61	1.61	1.59
Fe2	0.29	0.35	0.29	0.34	0.34	0.34	0.34	0.35	0.38
Mn	0.01	0.01	0.01	0.01	0.01	0.01	0.01	0.01	0.01
Ca	0.00	0.00	0.00	0.00	0.00	0.00	0.00	0.00	0.00
Na	0.00	0.00	0.00	0.00	0.00	0.00	0.00	0.00	0.00
Wt % ox Corrected Fe									
SiO2	54.91	54.81	53.89	55.04	54.9	54.76	55.04	55.67	55.47
TiO2	0.06	0.09	0.09	0.11	0.1	0.08	0.1	0.08	0.1
Al2O3	0.69	1.3	1.26	1.2	1.16	1.27	1.22	1.16	1.19
Cr2O3	0.22	0.39	0.36	0.32	0.26	0.42	0.4	0.34	0.33
Fe2O3	1.53	0.71	2.46	1.35	1.26	1.05	0.26	0.00	0.00
FeO	9.73	11.64	9.56	11.49	11.45	11.45	11.54	11.86	12.64
MnO	0.23	0.26	0.25	0.26	0.22	0.23	0.24	0.20	0.25
NiO	0.00	0.00	0.00	0.00	0.00	0.00	0.00	0.00	0.00
MgO	31.28	30.14	30.67	30.39	30.31	30.20	30.34	30.49	29.99
CaO	0.00	0.00	0.00	0.00	0.00	0.00	0.00	0.00	0.00
Na2O	0.00	0.00	0.01	0.00	0.01	0.01	0.01	0.00	0.00
ZrO2	0.00	0.00	0.00	0.00	0.00	0.00	0.00	0.00	0.00
Total	98.65	99.34	98.55	100.16	99.67	99.46	99.15	99.80	99.97
Mg# (Fe2)	85.14	82.19	85.12	82.50	82.52	82.46	82.41	82.09	80.87

	Sample Name/Number							
Wt% Oxides	21 / 1 .	22 / 1 .	24 / 1 .	26 / 1 .	27 / 1 .	28 / 1 .	29 / 1 .	30 / 1 . (13R9-213.63H)
SiO2	54.99	55.08	55.42	54.77	55.49	55.53	55.08	55.24
TiO2	0.12	0.1	0.11	0.1	0.11	0.06	0.09	0.05
Al2O3	1.37	1.31	1.22	1.18	1.33	0.85	1.02	1.04
Cr2O3	0.34	0.35	0.33	0.32	0.38	0.13	0.18	0.18
FeO	12.71	12.36	12.52	11.86	12.86	12.53	12.51	12.39
MnO	0.27	0.19	0.26	0.25	0.25	0.23	0.26	0.23
NiO								
MgO	29.95	29.46	30.13	29.9	30.18	30.67	30.51	30.58
CaO								
Na2O	0.01	0	0	0	0.01	0	0	0
ZrO2								
Total	100.55	99.49	100.64	98.94	101.3	100.49	100.18	100.3
A.P.F.U Fe Corrected								
Si	1.96	1.98	1.97	1.97	1.96	1.96	1.96	1.96
Al4	0.04	0.02	0.03	0.03	0.04	0.04	0.04	0.04
Al6	0.01	0.03	0.02	0.02	0.01	0.00	0.00	0.00
Fe3	0.02	0.00	0.00	0.00	0.01	0.03	0.04	0.03
Ti	0.00	0.00	0.00	0.00	0.00	0.00	0.00	0.00
Cr	0.01	0.01	0.01	0.01	0.01	0.00	0.01	0.01
Zr	0.00	0.00	0.00	0.00	0.00	0.00	0.00	0.00
Ni	0.00	0.00	0.00	0.00	0.00	0.00	0.00	0.00
Mg	1.59	1.58	1.59	1.60	1.59	1.62	1.61	1.62
Fe2	0.36	0.37	0.37	0.36	0.36	0.34	0.34	0.34
Mn	0.01	0.01	0.01	0.01	0.01	0.01	0.01	0.01
Ca	0.00	0.00	0.00	0.00	0.00	0.00	0.00	0.00
Na	0.00	0.00	0.00	0.00	0.00	0.00	0.00	0.00
Wt % ox Corrected Fe								
SiO2	54.99	55.08	55.42	54.77	55.49	55.53	55.08	55.24
TiO2	0.12	0.1	0.11	0.1	0.11	0.06	0.09	0.05
Al2O3	1.37	1.31	1.22	1.18	1.33	0.85	1.02	1.04
Cr2O3	0.34	0.35	0.33	0.32	0.38	0.13	0.18	0.18
Fe2O3	0.61	0.00	0.13	0.00	0.55	1.08	1.34	1.14
FeO	12.16	12.36	12.40	11.86	12.36	11.56	11.30	11.36
MnO	0.27	0.19	0.26	0.25	0.25	0.23	0.26	0.23
NiO	0.00	0.00	0.00	0.00	0.00	0.00	0.00	0.00
MgO	29.95	29.46	30.13	29.90	30.18	30.67	30.51	30.58
CaO	0.00	0.00	0.00	0.00	0.00	0.00	0.00	0.00
Na2O	0.01	0.00	0.00	0.00	0.01	0.00	0.00	0.00
ZrO2	0.00	0.00	0.00	0.00	0.00	0.00	0.00	0.00
Total	99.82	98.85	100.00	98.38	100.67	100.11	99.78	99.82
Mg# (Fe2)	81.44	80.95	81.24	81.80	81.31	82.55	82.79	82.75

Appendix G

EPMA data for Olivine

	Sample Name/Number							
Wt % Oxides	42 / 1 . (13R9-212.90B)	43 / 1 .	44 / 1 .	45 / 1 .	46 / 1 .	47 / 1 .	48 / 1 .	49 / 1 .
SiO2	39.79	39.68	38.87	38.97	37.81	39.7	39.03	39.07
FeO	13.9	14.05	13.46	14.48	14.68	14.63	13.8	13.74
MnO	0.17	0.17	0.16	0.2	0.15	0.18	0.16	0.17
MgO	46.06	46.25	45.53	46.02	45.82	45.9	45.31	46.45
NiO	0.24	0.22	0.22	0.22	0.22	0.26	0.26	0.3
ZnO	0.01	0.06	0.02	0	0	0.03	0	0
Al2O3	0	0.01	0	0	0	0	0	0
Cr2O3	0	0.01	0.01	0	0	0.02	0.01	0.01
CaO	0.02	0.01	0.02	0.03	0.01	0.01	0.03	0.02
Na2O	0	0	0.01	0	0.01	0	0	0
K2O	0	0	0.01	0	0.01	0.01	0	0.01
TiO2	0.01	0	0	0	0	0.01	0	0
Total	100.2	100.46	98.31	99.92	98.71	100.75	98.6	99.77
A.P.F.U Fe Corrected								
Si	0.99	0.99	0.98	0.97	0.96	0.99	0.99	0.97
Fe(ii)	0.29	0.29	0.29	0.30	0.31	0.30	0.29	0.29
Mn	0.00	0.00	0.00	0.00	0.00	0.00	0.00	0.00
Mg	1.71	1.71	1.72	1.71	1.73	1.70	1.71	1.73
Ni	0.00	0.00	0.00	0.00	0.00	0.01	0.01	0.01
Zn	0.00	0.00	0.00	0.00	0.00	0.00	0.00	0.00
Al	0.00	0.00	0.00	0.00	0.00	0.00	0.00	0.00
Cr	0.00	0.00	0.00	0.00	0.00	0.00	0.00	0.00
Ca	0.00	0.00	0.00	0.00	0.00	0.00	0.00	0.00
Na	0.00	0.00	0.00	0.00	0.00	0.00	0.00	0.00
K	0.00	0.00	0.00	0.00	0.00	0.00	0.00	0.00
Ti	0.00	0.00	0.00	0.00	0.00	0.00	0.00	0.00
Total	3	3	3	3	3	3	3	3
Wt% ox Corrected Fe								
SiO2	39.79	39.68	38.87	38.97	37.81	39.70	39.03	39.07
FeO	13.90	14.05	13.46	14.48	14.68	14.63	13.80	13.74
MnO	0.17	0.17	0.16	0.20	0.15	0.18	0.16	0.17
MgO	46.06	46.25	45.53	46.02	45.82	45.90	45.31	46.45
NiO	0.24	0.22	0.22	0.22	0.22	0.26	0.26	0.30
ZnO	0.01	0.06	0.02	0.00	0.00	0.03	0.00	0.00
Al2O3	0.00	0.01	0.00	0.00	0.00	0.00	0.00	0.00
Cr2O3	0.00	0.01	0.01	0.00	0.00	0.02	0.01	0.01
CaO	0.02	0.01	0.02	0.03	0.01	0.01	0.03	0.02
Na2O	0.00	0.00	0.01	0.00	0.01	0.00	0.00	0.00
K2O	0.00	0.00	0.01	0.00	0.01	0.01	0.00	0.01
TiO2	0.01	0.00	0.00	0.00	0.00	0.01	0.00	0.00
Total	**100.20**	**100.46**	**98.31**	**99.92**	**98.71**	**100.75**	**98.60**	**99.77**
Mg #	85.52	85.44	85.77	85.00	84.76	84.83	85.41	85.77
Ni (ppm)	1885.87	1728.72	1728.72	1728.72	1728.72	2043.03	2043.03	2357.34

	Sample Name/Number					
Wt % Oxides	50 / 1 . (212.90B)	116 / 1 . (13R9-213.63D)	117 / 1 .	118 / 1 .	119 / 1 .	120 / 1 .
SiO2	38.47	39.34	38.14	38.46	38.85	39.02
FeO	14.29	17.42	17.62	17.49	17.01	17.95
MnO	0.16	0.21	0.24	0.19	0.23	0.21
MgO	46.04	43.12	42.65	42.54	42.16	42.92
NiO	0.28	0.3	0.26	0.25	0.27	0.3
ZnO	0	0.02	0	0.05	0.03	0.04
Al2O3	0.02	0	0	0	0	0
Cr2O3	0	0.02	0	0	0	0
CaO	0	0.02	0.01	0.01	0.01	0.01
Na2O	0	0	0	0	0	0
K2O	0	0.02	0	0	0.01	0
TiO2	0	0	0	0	0	0
Total	99.26	100.47	98.92	98.99	98.57	100.45
A.P.F.U Fe Corrected						
Si	0.97	0.99	0.98	0.99	1.00	0.99
Fe(ii)	0.30	0.37	0.38	0.38	0.37	0.38
Mn	0.00	0.00	0.01	0.00	0.01	0.00
Mg	1.72	1.62	1.63	1.63	1.62	1.62
Ni	0.01	0.01	0.01	0.01	0.01	0.01
Zn	0.00	0.00	0.00	0.00	0.00	0.00
Al	0.00	0.00	0.00	0.00	0.00	0.00
Cr	0.00	0.00	0.00	0.00	0.00	0.00
Ca	0.00	0.00	0.00	0.00	0.00	0.00
Na	0.00	0.00	0.00	0.00	0.00	0.00
K	0.00	0.00	0.00	0.00	0.00	0.00
Ti	0.00	0.00	0.00	0.00	0.00	0.00
Total	3	3	3	3	3	3
Wt% ox Corrected Fe						
SiO2	38.47	39.34	38.14	38.46	38.85	39.02
FeO	14.29	17.42	17.62	17.49	17.01	17.95
MnO	0.16	0.21	0.24	0.19	0.23	0.21
MgO	46.04	43.12	42.65	42.54	42.16	42.92
NiO	0.28	0.30	0.26	0.25	0.27	0.30
ZnO	0.00	0.02	0.00	0.05	0.03	0.04
Al2O3	0.02	0.00	0.00	0.00	0.00	0.00
Cr2O3	0.00	0.02	0.00	0.00	0.00	0.00
CaO	0.00	0.02	0.01	0.01	0.01	0.01
Na2O	0.00	0.00	0.00	0.00	0.00	0.00
K2O	0.00	0.02	0.00	0.00	0.01	0.00
TiO2	0.00	0.00	0.00	0.00	0.00	0.00
Total	**99.26**	**100.47**	**98.92**	**98.99**	**98.57**	**100.45**
Mg #	85.17	81.52	81.18	81.26	81.54	81.00
Ni (ppm)	2200.19	2357.34	2043.03	1964.45	2121.61	2357.34

	Sample Name/Number							
Wt % Oxides	121 / 1 .	123 / 1 .	124 / 1 .	125 / 1 .	126 / 1 .	127 / 1 .	128 / 1 .	130 / 1 . (13R9-213.63D)
SiO2	39.03	38.23	39.33	39.08	38	38.91	37.83	39.73
FeO	16.92	17.7	18.22	18.18	18.2	18.03	18.17	18.08
MnO	0.24	0.18	0.23	0.25	0.22	0.21	0.24	0.16
MgO	42.16	41.84	42.63	42.73	42.93	42.66	43.26	41.21
NiO	0.31	0.27	0.33	0.3	0.31	0.3	0.27	0.34
ZnO	0.11	0.01	0	0	0	0	0	0
Al2O3	0	0	0.02	0	0	0.01	0	0
Cr2O3	0.01	0.01	0.01	0	0	0	0.01	0
CaO	0.01	0.01	0.01	0.01	0.01	0.02	0.02	0.01
Na2O	0	0	0	0	0.01	0	0	0.01
K2O	0.01	0	0.01	0	0	0	0.01	0
TiO2	0	0	0	0	0.01	0	0	0
Total	98.8	98.25	100.79	100.55	99.69	100.14	99.81	99.54
A.P.F.U Fe Corrected								
Si	1.00	0.99	0.99	0.99	0.97	0.99	0.96	1.02
Fe(ii)	0.36	0.38	0.39	0.39	0.39	0.38	0.39	0.39
Mn	0.01	0.00	0.00	0.01	0.00	0.00	0.01	0.00
Mg	1.62	1.62	1.61	1.61	1.63	1.62	1.64	1.58
Ni	0.01	0.01	0.01	0.01	0.01	0.01	0.01	0.01
Zn	0.00	0.00	0.00	0.00	0.00	0.00	0.00	0.00
Al	0.00	0.00	0.00	0.00	0.00	0.00	0.00	0.00
Cr	0.00	0.00	0.00	0.00	0.00	0.00	0.00	0.00
Ca	0.00	0.00	0.00	0.00	0.00	0.00	0.00	0.00
Na	0.00	0.00	0.00	0.00	0.00	0.00	0.00	0.00
K	0.00	0.00	0.00	0.00	0.00	0.00	0.00	0.00
Ti	0.00	0.00	0.00	0.00	0.00	0.00	0.00	0.00
Total	3	3	3	3	3	3	3	3
Wt% ox Corrected Fe								
SiO2	39.03	38.23	39.33	39.08	38.00	38.91	37.83	39.73
FeO	16.92	17.70	18.22	18.18	18.20	18.03	18.17	18.08
MnO	0.24	0.18	0.23	0.25	0.22	0.21	0.24	0.16
MgO	42.16	41.84	42.63	42.73	42.93	42.66	43.26	41.21
NiO	0.31	0.27	0.33	0.30	0.31	0.30	0.27	0.34
ZnO	0.11	0.01	0.00	0.00	0.00	0.00	0.00	0.00
Al2O3	0.00	0.00	0.02	0.00	0.00	0.01	0.00	0.00
Cr2O3	0.01	0.01	0.01	0.00	0.00	0.00	0.01	0.00
CaO	0.01	0.01	0.01	0.01	0.01	0.02	0.02	0.01
Na2O	0.00	0.00	0.00	0.00	0.01	0.00	0.00	0.01
K2O	0.01	0.00	0.01	0.00	0.00	0.00	0.01	0.00
TiO2	0.00	0.00	0.00	0.00	0.01	0.00	0.00	0.00
Total	**98.80**	**98.25**	**100.79**	**100.55**	**99.69**	**100.14**	**99.81**	**99.54**
Mg #	81.62	80.82	80.66	80.73	80.79	80.83	80.93	80.25
Ni (ppm)	2435.92	2121.61	2593.08	2357.34	2435.92	2357.34	2121.61	2671.66

	Sample Name/Number						
Wt % Oxides	1 / 1 . (13R9-213.63H)	2 / 1 .	3 / 1 .	4 / 1 .	5 / 1 .	6 / 1 .	7 / 1 .
SiO2	37.86	38.79	38.71	38.23	38.46	38.74	39
FeO	17.85	18.76	18.71	18.84	18.14	17.87	18.5
MnO	0.21	0.22	0.2	0.21	0.23	0.22	0.23
MgO	41.87	41.43	41.17	42.22	42.14	41.5	41.31
NiO	0.19	0.25	0.2	0.18	0.18	0.22	0.2
ZnO	0	0	0	0.05	0.06	0	0
Al2O3	0.01	0.01	0	0	0	0	0
Cr2O3	0.01	0	0	0.02	0	0	0.01
CaO	0.01	0.04	0.03	0.02	0.04	0.02	0.02
Na2O	0.02	0.02	0	0	0	0.01	0
K2O	0	0	0	0.01	0	0.01	0
TiO2	0	0.01	0	0	0	0	0
Total	98.03	99.53	99.02	99.78	99.25	98.59	99.27
A.P.F.U Fe Corrected							
Si	0.98	1.00	1.00	0.98	0.99	1.00	1.00
Fe(ii)	0.39	0.40	0.40	0.40	0.39	0.39	0.40
Mn	0.00	0.00	0.00	0.00	0.01	0.00	0.01
Mg	1.62	1.59	1.59	1.61	1.61	1.60	1.59
Ni	0.00	0.01	0.00	0.00	0.00	0.00	0.00
Zn	0.00	0.00	0.00	0.00	0.00	0.00	0.00
Al	0.00	0.00	0.00	0.00	0.00	0.00	0.00
Cr	0.00	0.00	0.00	0.00	0.00	0.00	0.00
Ca	0.00	0.00	0.00	0.00	0.00	0.00	0.00
Na	0.00	0.00	0.00	0.00	0.00	0.00	0.00
K	0.00	0.00	0.00	0.00	0.00	0.00	0.00
Ti	0.00	0.00	0.00	0.00	0.00	0.00	0.00
Total	3	3	3	3	3	3	3
Wt% ox Corrected Fe							
SiO2	37.86	38.79	38.71	38.23	38.46	38.74	39.00
FeO	17.85	18.76	18.71	18.84	18.14	17.87	18.50
MnO	0.21	0.22	0.20	0.21	0.23	0.22	0.23
MgO	41.87	41.43	41.17	42.22	42.14	41.50	41.31
NiO	0.19	0.25	0.20	0.18	0.18	0.22	0.20
ZnO	0.00	0.00	0.00	0.05	0.06	0.00	0.00
Al2O3	0.01	0.01	0.00	0.00	0.00	0.00	0.00
Cr2O3	0.01	0.00	0.00	0.02	0.00	0.00	0.01
CaO	0.01	0.04	0.03	0.02	0.04	0.02	0.02
Na2O	0.02	0.02	0.00	0.00	0.00	0.01	0.00
K2O	0.00	0.00	0.00	0.01	0.00	0.01	0.00
TiO2	0.00	0.01	0.00	0.00	0.00	0.00	0.00
Total	**98.03**	**99.53**	**99.02**	**99.78**	**99.25**	**98.59**	**99.27**
Mg #	80.70	79.74	79.68	79.98	80.55	80.54	79.92
Ni (ppm)	1492.98	1964.45	1571.56	1414.41	1414.41	1728.72	1571.56

	Sample Name/Number						
Wt % Oxides	8 / 1 .	9 / 1 .	10 / 1 .	11 / 1 .	12 / 1 .	13 / 1 .	14 / 1 . (13R9-213.63H)
SiO2	38.98	38.89	38.71	38.53	38.48	38.38	37.54
FeO	19.13	19.19	19.09	18.95	18.84	18.91	18.88
MnO	0.23	0.24	0.22	0.23	0.25	0.23	0.22
MgO	41.16	41.51	41.34	41.52	42.13	41.48	41.91
NiO	0.22	0.24	0.27	0.23	0.25	0.19	0.22
ZnO	0	0	0.01	0	0.01	0	0
Al2O3	0.02	0	0	0.01	0	0	0.01
Cr2O3	0	0	0	0.01	0	0	0
CaO	0.01	0.04	0.02	0.01	0.02	0.01	0
Na2O	0	0	0	0.01	0	0	0
K2O	0	0	0	0	0	0	0
TiO2	0	0	0	0.01	0	0.01	0
Total	99.75	100.11	99.66	99.51	99.98	99.21	98.78
A.P.F.U Fe Corrected							
Si	1.00	0.99	0.99	0.99	0.98	0.99	0.97
Fe(ii)	0.41	0.41	0.41	0.41	0.40	0.41	0.41
Mn	0.01	0.01	0.00	0.01	0.01	0.01	0.00
Mg	1.58	1.58	1.58	1.59	1.60	1.59	1.61
Ni	0.00	0.00	0.01	0.00	0.01	0.00	0.00
Zn	0.00	0.00	0.00	0.00	0.00	0.00	0.00
Al	0.00	0.00	0.00	0.00	0.00	0.00	0.00
Cr	0.00	0.00	0.00	0.00	0.00	0.00	0.00
Ca	0.00	0.00	0.00	0.00	0.00	0.00	0.00
Na	0.00	0.00	0.00	0.00	0.00	0.00	0.00
K	0.00	0.00	0.00	0.00	0.00	0.00	0.00
Ti	0.00	0.00	0.00	0.00	0.00	0.00	0.00
Total	3	3	3	3	3	3	3
Wt% ox Corrected Fe							
SiO2	38.98	38.89	38.71	38.53	38.48	38.38	37.54
FeO	19.13	19.19	19.09	18.95	18.84	18.91	18.88
MnO	0.23	0.24	0.22	0.23	0.25	0.23	0.22
MgO	41.16	41.51	41.34	41.52	42.13	41.48	41.91
NiO	0.22	0.24	0.27	0.23	0.25	0.19	0.22
ZnO	0.00	0.00	0.01	0.00	0.01	0.00	0.00
Al2O3	0.02	0.00	0.00	0.01	0.00	0.00	0.01
Cr2O3	0.00	0.00	0.00	0.01	0.00	0.00	0.00
CaO	0.01	0.04	0.02	0.01	0.02	0.01	0.00
Na2O	0.00	0.00	0.00	0.01	0.00	0.00	0.00
K2O	0.00	0.00	0.00	0.00	0.00	0.00	0.00
TiO2	0.00	0.00	0.00	0.01	0.00	0.01	0.00
Total	**99.75**	**100.11**	**99.66**	**99.51**	**99.98**	**99.21**	**98.78**
Mg #	79.32	79.41	79.42	79.61	79.94	79.63	79.83
Ni (ppm)	1728.72	1885.87	2121.61	1807.30	1964.45	1492.98	1728.72

Appendix H

Mean and standard deviation calculations for mineral chemistry analyses

Cr-Spinel mineral chemistry

9HW	Mg#	Cr#	Ni (ppm)	Cr/Fe	Al2O3	Cr2O3
Mean	40.91	66.42	513.38	1.70	15.99	47.16
Standard Deviation	2.45	0.44	212.53	0.04	0.26	0.39
3FW	Mg#	Cr#	Ni (ppm)	Cr/Fe	Al2O3	Cr2O3
Mean	34.12	70.64	1021.52	1.15	12.06	43.24
Standard Deviation	1.33	0.52	238.34	0.03	0.22	0.60
9FWa	Mg#	Cr#	Ni (ppm)	Cr/Fe	Al2O3	Cr2O3
Mean	34.24	57.53	602.43	1.30	20.06	40.51
Standard Deviation	1.80	0.59	161.46	0.03	0.41	0.21
9FWb	Mg#	Cr#	Ni (ppm)	Cr/Fe	Al2O3	Cr2O3
Mean	31.73	57.21	377.17	1.28	20.37	40.53
Standard Deviation	2.15	2.65	195.03	0.04	1.57	1.32
9FW (Avg)	Mg#	Cr#	Ni (ppm)	Cr/Fe	Al2O3	Cr2O3
Mean	33.10	57.38	500.04	1.29	20.20	40.52
Standard Deviation	2.33	1.85	209.97	0.03	1.11	0.90

Orthopyroxene mineral chemistry

9HW	Mg#	FeO	MgO				
Mean	85.78	9.41	31.84				
Standard Deviation	0.88	0.65	0.35				
3FW	Mg#	FeO	MgO				
Mean	84.45	10.20	31.07				
Standard Deviation	0.80	0.54	0.30				
9FWa	Mg#	FeO	MgO				
Mean	82.73	11.29	30.32				
Standard Deviation	1.05	0.74	0.36	9FW (Avg)	Mg#	FeO	MgO
				Mean	82.33	11.58	30.25
9FWb	Mg#	FeO	MgO	Standard Deviation	1.05	0.73	0.37
Mean	81.74	12.00	30.15				
Standard Deviation	0.72	0.47	0.36				

Olivine mineral chemistry

9HW	Mg#	Ni (ppm)	FeO	MgO		
Mean	85.30	1938.26	14.11	45.93		
Standard Deviation	0.36	222.25	0.40	0.33		
9FWa	Mg#	Ni (ppm)	FeO	MgO		
Mean	81.01	2302.94	17.77	42.52		
Standard Deviation	0.38	205.33	0.43	0.54	9FW (Avg)	Ni (ppm)
					Mean	1993.56
9FWb	Mg#	Ni (ppm)	FeO	MgO	Standard Deviation	364.92
Mean	79.88	1706.27	18.69	41.62		
Standard Deviation	0.42	215.05	0.42	0.35		

Appendix I

Borehole co-ordinates with the Cr/Fe ratio for the LG-6 chromitite

BHID	Micromine E	Micromine N	RL	LG-6 Contact	Cr/Fe
13R0001	-7019.621	-2785959.785	1112.116	1029.406	1.55
13R0003	-6747.806	-2786084.05	1107.433	940.16	1.50
13R0005	-6464.104	-2786190.71	1100.033	862.24	2.02
13R0007	-7000.117	-2786300.271	1114.014	991.16	1.55
13R0008	-6861.492	-2786354.928	1110.596	961.976	2.00
13R0009	-6669.976	-2786437.91	1104.206	891.25	2.04
13R0010	-6704.846	-2786752.289	1109.87	915.37	1.85
13R0011	-6988.445	-2786631.794	1114.375	971.81	1.72
13R0031	-6939.308	-2786158.399	1112.44	1000.81	
13R0032	-6783.009	-2786548.256	1109.016	913.53	2.10
13R0002	-6884.042	-2786022.93	1110.996	976.33	1.56
13R0004	-6681.117	-2787085.978	1109.64	897.42	1.55
13R0013	-7097.384	-2786910.505	1117.715	986.41	1.53
13R0014	-7365.495	-2787177.565	1124.014	1017.50	1.56
13R0015	-6794.068	-2787328.131	1111.673	891.99	1.55
13R0016	-7330.352	-2787457.014	1123.928	995.07	1.56
13R0017A	-6958.618	-2787366.83	1114.76	944.24	1.57
13R0033	-6939.308	-2786158.399	1112.44	759.06	
ZS1	-6203.303	-2785784.196	1094.8	819.76	1.57
ZD132	-7008.0232	-2785873.249	1110.961	1032.49	1.58
ZD137	-6698.8919	-2785875.008	1106.138	932.51	1.58
ZD76	-6980.261	-2785712.794	1108.883	1036.10	

Appendix J

Breakdown of each sample, with the respective analyses done to each sample

BHID	Sample №	Reef	Rock type (by Eye)	Thin sections	Intertek XRF+ICP-MS	PGE	Probe
13R0003	13R-3/150.88-151		Pyx	-	-		
13R0003	13R-3/152.09-152.19		Pyx	-	-		
13R0003	13R-3/152.44-152.54		Pyx, dissem	-			
13R0003	13R-3/152.68A		Pyx	-	-		
13R0003	13R-3/152.68B		Pyx	-			
13R0003	13R-3/152.68C		Pyx	-	-		
13R0003	13R-3/152.68D	LG-6A	Chr	-	-	-	
13R0003	13R-3/152.80A	LG-6A	Chr	-	-	-	
13R0003	13R-3/152.80B	LG-6A	Chr	-	-	-	
13R0003	13R-3/152.80C	LG-6A	Chr	-	-	-	
13R0003	13R-3/152.80D	LG-6A	Chr	-	-	-	
13R0003	13R-3/152.80E	LG-6A	Chr	-	-	-	
13R0003	13R-3/152.95A		Pyx	-	-		
13R0003	13R-3/152.95B		Pyx	-			
13R0003	13R-3/152.95C		Chr	-			
13R0003	13R-3/152.95D		Chr/Pyx, 50,	-			
13R0003	13R-3/152.95E		Pyx	-	-		
13R0003	13R-3/152.95F		Pyx	-			
13R0003	13R-3/152.95G		Pyx	-			
13R0003	13R-3/153.38-153.48		Pyx	-	-		
13R0003	13R-3/154-154.10		Pyx	-	-		
13R0003	13R-3/155.92-156		Pyx	-	-		
13R0003	13R-3/157-157.10		Pyx	-	-		
13R0003	13R-3/160.70-160.78		Pyx	-	-		
13R0003	13R-3/163.58-163.67		Pyx	-	-		
13R0003	13R-3/164.83-165		Pyx	-	-	-	
13R0003	13R-3/166.10-166.27		Pyx	-	-		
13R0003	13R-3/166.78-166.85		Pyx, dissem	-	-		
13R0003	13R-3/167.10F		Chr-Pyx	-	-	-	
13R0003	13R-3/167.10G		Chr-Pyx	-			
13R0003	13R-3/167.10H		Chr-Pyx	-	-	-	
13R0003	13R-3/167.34A		Chr-Pyx	-			
13R0003	13R-3/167.34B		Chr-Pyx	-	-	-	
13R0003	13R-3/167.34C		Chr-Pyx	-			
13R0003	13R-3/167.34D		Chr-Pyx	-	-	-	
13R0003	13R-3/167.46A	LG-6	Chr	-	-	-	
13R0003	13R-3/167.46B	LG-6	Chr	-	-	-	
13R0003	13R-3/167.46C						
13R0003	13R-3/167.46D1	LG-6	Chr	-	-	-	
13R0003	13R-3/167.46D2						
13R0003	13R-3/167.46E	LG-6	Chr	-	-	-	
13R0003	13R-3/167.60A	LG-6	Chr	-			
13R0003	13R-3/167.60B	LG-6	Chr	-	-	-	
13R0003	13R-3/167.60C	LG-6	Chr	-			

BHID	Sample №	Reef	Rock type (by Eye)	Thin sections	Intertek XRF+ICP-MS	PGE	Probe
13R0009	13R-9/200.15B	LG-6A	Chr-Pyx	-	-	-	
13R0009	13R-9/200.15C		Pyx	-	-	-	
13R0009	13R-9/200.15D		Pyx	-			
13R0009	13R-9/200.15E		Pyx	-	-		
13R0009	13R-9/201.29-201.41		Pyx	-	-		
13R0009	13R-9/201.95-202.10		Pyx	-	-		
13R0009	13R-9/203.30-203.43		Pyx	-	-		
13R0009	13R-9/204.40-204.52				-	-	
13R0009	13R-9/205.42-205.52		Pyx	-	-		
13R0009	13R-9/206.15-206.29		Pyx	-	-		
13R0009	13R-9/208.22-208.34		Pyx	-	-		
13R0009	13R-9/209.79-209.93		Pyx	-	-		
13R0009	13R-9/211.09-211.26		Pyx	-	-	-	
13R0009	13R-9/211.87D		Pyx	-	-		
13R0009	13R-9/212.10A		Ol-Pyx	-	-		
13R0009	13R-9/212.68A		Ol	-	-		
13R0009	13R-9/212.68B		Ol	-			
13R0009	13R-9/212.68C		Ol	-	-		
13R0009	13R-9/212.80A		Ol	-			
13R0009	13R-9/212.80B		Ol	-	-	-	
13R0009	13R-9/212.84A		Chr	-			
13R0009	13R-9/212.84B		Ol-Pyx	-	-		
13R0009	13R-9/212.90A		Ol-Pyx	-			
13R0009	13R-9/212.90B		Ol-Pyx	-	-		- (9HW)
13R0009	13R-9/212.90C		Ol-Pyx	-			
13R0009	13R-9/212.90D		Ol-Pyx	-	-	-	
13R0009	13R-9/212.90E	LG-6	Chr	-	-	-	
13R0009	13R-9/212.90F	LG-6	Chr	-			
13R0009	13R-9/212.90G	LG-6	Chr	-	-	-	
13R0009	13R-9/212.90H	LG-6	Chr	-			
13R0009	13R-9/212.90I	LG-6	Chr	-	-	-	
13R0009	13R-9/212.90J	LG-6	Chr	-			
13R0009	13R-9/212.90K	LG-6	Chr	-	-	-	
13R0009	13R-9/212.90L	LG-6	Chr	-			
13R0009	13R-9/212.90M	LG-6	Chr	-	-	-	
13R0009	13R-9/213.27A	LG-6	Chr	-			
13R0009	13R-9/213.27B	LG-6	Chr	-	-	-	
13R0009	13R-9/213.27C	LG-6	Chr	-			
13R0009	13R-9/213.27D	LG-6	Chr	-	-	-	
13R0009	13R-9/213.27E	LG-6	Chr	-			
13R0009	13R-9/213.27F	LG-6	Chr	-	-	-	
13R0009	13R-9/213.27G	LG-6	Chr	-			
13R0009	13R-9/213.27H	LG-6	Chr	- (2)	-	-	
13R0009	13R-9/213.50A	LG-6	Chr	-			

BHID	Sample №	Reef	Rock type (by Eye)	Thin sections	Intertek XRF+ICP-MS	PGE	Probe
13R0003	13R-3/167.70A	LG-6	Chr	-	-	-	
13R0003	13R-3/167.70B	LG-6	Chr	-			
13R0003	13R-3/167.70C	LG-6	Chr	-	-	-	
13R0003	13R-3/167.80A	LG-6	Chr	-			
13R0003	13R-3/167.80B	LG-6	Chr	-	-	-	
13R0003	13R-3/167.80C	LG-6	Chr	-			
13R0003	13R-3/167.80D	LG-6	Chr	-	-	-	
13R0003	13R-3/167.80E	LG-6	Chr	-			
13R0003	13R-3/167.80F	LG-6	Chr	-	-	-	
13R0003	13R-3/167.80G	LG-6	Chr	-			
13R0003	13R-3/167.80H	LG-6	Chr	-	-	-	
13R0003	13R-3/168.02A	LG-6	Chr	-			
13R0003	13R-3/168.02B	LG-6	Chr	-	-	-	
13R0003	13R-3/168.02C	LG-6	Chr	-			
13R0003	13R-3/168.02D	LG-6	Chr	-	-	-	
13R0003	13R-3/168.02E						
13R0003	13R-3/168.02F	LG-6	Chr	-	-	-	
13R0003	13R-3/168.02G	LG-6	Chr	-	-	-	
13R0003	13R-3/168.24A		Chr-Pyx	-	-	-	- (3FW)
13R0003	13R-3/168.24B		Chr-Pyx	-			
13R0003	13R-3/168.24C		Chr-Pyx	-			
13R0003	13R-3/168.24D		Chr-Pyx	-	-	-	
13R0003	13R-3/168.56-168-68		Pyx	-	-		
13R0003	13R-3/168.93-169		Pyx	-	-		
13R0003	13R-3/171.90-172		Pyx	-	-		
13R0009	13R-9/199.22A		Ol-Pyx	-			
13R0009	13R-9/199.46A		Ol-Pyx	-	-	-	
13R0009	13R-9/199.60A		Pyx	-	-		
13R0009	13R-9/199.60B		Pyx	-			
13R0009	13R-9/199.60C		Pyx	-	-	-	
13R0009	13R-9/199.60D	LG-6A	Chr	-	-	-	
13R0009	13R-9/199.60E	LG-6A	Chr	-			
13R0009	13R-9/199.60F	LG-6A	Chr	-	-	-	
13R0009	13R-9/199.82A	LG-6A	Chr	-			
13R0009	13R-9/199.82B	LG-6A	Chr	-	-	-	
13R0009	13R-9/199.82C	LG-6A	Chr	-			
13R0009	13R-9/199.82D	LG-6A	Chr	-	-	-	
13R0009	13R-9/199.82E						
13R0009	13R-9/199.82F	LG-6A	Chr	-	-	-	
13R0009	13R-9/199.82G	LG-6A	Chr	-			
13R0009	13R-9/199.82H	LG-6A	Chr	-	-	-	
13R0009	13R-9/199.82I						
13R0009	13R-9/199.82J	LG-6A	Chr	-	-	-	
13R0009	13R-9/200.15A	LG-6A	Chr-Pyx	-			

BHID	Sample №	Reef	Rock type (by Eye)	Thin sections	Intertek XRF+ICP-MS	PGE	Probe
13R0009	13R-9/213.50B	LG-6	Chr	-	-	-	
13R0009	13R-9/213.50C	LG-6	Chr	-			
13R0009	13R-9/213.50D	LG-6	Chr	-	-	-	
13R0009	13R-9/213.63A		Chr-Ol	-	-	-	
13R0009	13R-9/213.63B		Chr-Ol	-			
13R0009	13R-9/213.63C		Chr-Ol	-	-	-	
13R0009	13R-9/213.63D		Chr-Ol	-	-	-	- (9FWa)
13R0009	13R-9/213.63E		Ol	-	-	-	
13R0009	13R-9/213.63F		Ol	-			
13R0009	13R-9/213.63G		Ol	-	-		
13R0009	13R-9/213.63H		Ol	-			- (9FWb)
13R0009	13R-9/213.97A		Ol	-	-		
13R0009	13R-9/214.24A		Pyx	-	-		
13R0009	13R-9/214.24G		Pyx	-	-		
13R0009	13R-9/214.69-214.80		Pyx	-	-		
13R0009	13R-9/215.20-215.30		Pyx	-	-		
13R0009	13R-9/215.65-215.79		Pyx	-	-	-	

Appendix K

Sample list from second sampling trip from March 2016

Second sampling trip (March 2016) samples of several different reefs from several boreholes

Borehole	Sample №	Reef	Rock type (by Eye)	Thin sections	Intertek XRF+ICP-MS	PGE	Probe	Notes
13R0032	32R6A	LG-6A	Chr		-	-		
13R0033	33R4C	MG-4C	Chr		-	-		
13R0033	33R4B	MG-4B	Chr		-	-		
13R0033	33R4A	MG-4A	Chr		-	-		
13R0033	33R7	LG-7			-	-		
13R0033	33R6A	LG-6A	Chr		-	-		
13R0015	15R6A	LG-6A	Chr		-	-		
13R0015	15R7	LG-7			-	-		
13R0010	10R6A	LG-6A	Chr		-	-		
13R0010	10R7	LG-7			-	-		
13R0008	8R6	LG-6	Chr		-	-		
13R0008	8R6A	LG-6A	Chr		-	-		
13R0001	1R6#1	LG-6	Chr		-	-		Sample split into 2 due to different textures and chemistry
13R0001	1R6#2	LG-6	Chr		-	-		Sample split into 2 due to different textures and chemistry
13R0001	1R6A#1	LG-6A	Chr		-	-		Triplicate as a test
13R0001	1R6A#2	LG-6A	Chr		-	-		Triplicate as a test
13R0001	1R6A#3	LG-6A	Chr		-	-		Triplicate as a test
13R0003	3R7	LG-7			-	-		
13R0005	5R4C	MG-4C (B?)	Chr		-	-		
13R0005	5R4A#1	MG-4A	Chr		-	-		Increasing plag with depth.
13R0005	5R4A#2	MG-4A	Chr		-	-		Dyke from 52.15m - 53.09m
13R0005	5R2B	MG-2B	Chr		-	-		
13R0005	5R2A	MG-2A	Chr		-	-		
13R0005	5R1	MG-1	Chr		-	-		
13R0005	5R7	LG-7			-	-		
13R0004	4R2B	MG-2B	Chr		-	-		
13R0004	4R2A	MG-2A	Chr		-	-		
13R0004	4R1	MG-1	Chr		-	-		
13R0008	8R7#1	LG-7			-	-		Triplicate as a test
13R0008	8R7#2	LG-7			-	-		Triplicate as a test
13R0008	8R7#3	LG-7			-	-		Triplicate as a test
13R0013	13R6A	LG-6A	Chr		-	-		
13R0031	31R6T	LG-6	Chr		-	-		sperated by dolerite dyke
13R0031	31R6B	LG-6	Chr		-	-		sperated by dolerite dyke